

N86 - 30232 (^{D5-76}
1489.

11658

APPENDIX 6.4

A COMPARISON OF CURRENT MODELS FOR NONLINEAR RATE-DEPENDENT
MATERIAL BEHAVIOR OF CRYSTALLINE SOLIDS

A Thesis

by

JOACHIM MICHAEL BEEK

Submitted to the Graduate College of

Texas A&M University

in partial fulfillment of the requirements for the degree of

MASTER OF SCIENCE

May 1986

Major Subject: Aerospace Engineering

ABSTRACT

A Comparison of Current Models for Nonlinear Rate-Dependent
Material Behavior of Crystalline Solids. (May 1986)

Joachim Michael Beek, B.S., Texas A&M University

Chair of Advisory Committee: Dr. D. H. Allen

This thesis reviews three theories for prediction of inelastic deformation which are based on considerations of the microstructural behavior of materials. These theories are those of Krieg, et al., Bodner, et al., and Miller, et al. The thesis opens with a review of the mechanics of continua with internal state variables and a review of the historical development of constitutive modelling. A detailed discussion, including chronological development, review of theory, and method of determination of material parameters, of each model follows. An experimental data base is established from which the material parameters of the constitutive equations are calculated. Finally, computer simulations of various load histories are performed and compared to experiment, and conclusions of the ability of each theory to model inelastic deformation are drawn.

ACKNOWLEDGMENTS

I wish to thank Dr. David H. Allen for his guidance, patience, and support throughout this research effort.

I would also like to thank Dr. R. A. Schapery and Dr. W. L. Bradley for kindly consenting to join my committee and for their support. Gratitude is due to my wife for her patience and to all others, too numerous to mention here, who aided in this work.

This research was supported by NASA Lewis Research Center under Grant no. NAG3-491.

TABLE OF CONTENTS

	Page
INTRODUCTION.....	1
THE EQUATION OF STATE APPROACH.....	6
LITERATURE REVIEW AND GENERAL DISCUSSION OF MODELS.....	16
Classical Plasticity Models.....	16
Nonlinear Viscoelasticity Models.....	21
Microstructural Models.....	25
KRIEG, SWEARENGEN, AND ROHDE'S MODEL.....	33
Chronological Development.....	33
General Theory.....	35
Evaluation of Material Constants.....	41
BODNER AND PARTOM'S MODEL.....	54
Chronological Development.....	54
General Theory.....	57
Evaluation of Material Constants.....	62
MILLER'S MODEL.....	72
Chronological Development.....	72
General Theory.....	75
Evaluation of Material Constants.....	81
DETERMINATION OF MATERIAL CONSTANTS.....	85
Material Constants for Krieg, <u>et al</u>	90
Material Constants for Bodner, <u>et al</u>	95
Material Constants for Miller, <u>et al</u>	102
COMPARISON OF THEORY TO EXPERIMENT.....	107
Qualitative Review of Predictive Capabilities.....	107
Review of Integration Technique.....	109
Comparison of Numerical Predictions to Experiment.....	110
SUMMARY AND CONCLUSIONS.....	141
REFERENCES.....	144

LIST OF TABLES

	Page
Table 1. Composition and Material Properties of Al 5086.....	87
Table 2. Review of Material Test Requirements.....	88
Table 3. Pertinent Results of Experimental Tests.....	92
Table 4. Calculated Values of Z used in the Determination of Z_0	99
Table 5. Calculated Values of Z used in the Determination of A and r.....	100
Table 6. Calculations for Various Values of A.....	103
Table 7. Summary of Material Constants for all Models.....	106

LIST OF FIGURES

	Page
Fig. 1 Phenomena associated with inelastic deformation (uniaxial loading).....	4
Fig. 2 Phenomena associated with inelastic deformation (cyclic loading).....	5
Fig. 3 The relationship between local inhomogeneities and the continuum assumption.....	13
Fig. 4 The three parameter standard solid.....	22
Fig. 5 A comparison of the hyperbolic sine, power law, and exponential forms of the inelastic strain rate equation.....	29
Fig. 6 Strain response for rapid stress reductions during steady-state creep.....	43
Fig. 7 A stress-drop test.....	44
Fig. 8 Four hypotheses for creep response following a stress-drop.....	46
Fig. 9 A qualitative graph of $\ln(\dot{\epsilon}^I)$ v. $\ln \sigma - \alpha $ for determining c_1 and c_2	49
Fig. 10 A qualitative graph of the primary-to-secondary creep ratio used in determining c_3 and c_4	52
Fig. 11 A qualitative comparison of a saturated stress curve and a non-saturated stress curve.....	63
Fig. 12 A qualitative graph of constant strain rate tensile data for determining n and Z_1	65
Fig. 13 A qualitative graph of γ v. σ for determining the saturated stress level.....	67
Fig. 14 A qualitative graph of $\ln(Z_1 - Z)$ v. W^P for determining m and Z_0	69
Fig. 15 The effect of A on $\log_{10}(\dot{\epsilon}_{ss}^I / \theta')$ v. $\log_{10}[\sinh(A\sigma_{ss}/E)]$ data.....	83

Fig. 16	Experimental constant strain rate tensile test response.....	89
Fig. 17	Experimental creep test response.....	91
Fig. 18	Graph of $\ln(\dot{\epsilon}^I)$ v. $\ln \sigma - \alpha $ for Krieg's model.....	93
Fig. 19	Graph of γ v. σ for Bodner's model.....	97
Fig. 20	Graph of $\ln[-\ln(\frac{\sqrt{3}}{2}\dot{\epsilon}^I/D_0)]$ v. $\ln(\sigma_s)$ for Bodner's model.....	98
Fig. 21	Graph of $\ln[m(Z_1 - Z)\dot{W}^P]$ v. $\ln[(Z - Z_2)/Z_1]$ for Bodner's model.....	101
Fig. 22	Graph of $\log_{10}(\dot{\epsilon}_{ss}^I/\theta')$ v. $\log_{10}[\sinh(A\sigma_{ss}/E)]$ for Miller's model.....	104
Fig. 23	Experimental constant strain rate tensile test: $\dot{\epsilon} = 4(10)^{-5}$ sec $^{-1}$	111
Fig. 24	Constant strain rate tensile test. Comparison of theory of Krieg, <u>et al.</u> , to experiment.....	113
Fig. 25	Constant strain rate tensile test. Comparison of theory of Bodner, <u>et al.</u> , to experiment.....	115
Fig. 26	Constant strain rate tensile test. Comparison of theory of Miller, <u>et al.</u> , to experiment.....	116
Fig. 27	Constant strain rate tensile test. Comparison of all theories to experiment.....	117
Fig. 28	Experimental cyclic loading test: cycles 1-10.....	119
Fig. 29	Cyclic loading test cycle 1. Comparison of theory of Krieg, <u>et al.</u> , to experiment.....	120
Fig. 30	Cyclic loading test: cycles 1 and 10. Prediction of theory of Krieg, <u>et al.</u>	121
Fig. 31	Cyclic loading test: cycle 10. Comparison of theory of Krieg, <u>et al.</u> , to experiment.....	123
Fig. 32	Cyclic loading test: cycle 1. Comparison of theory of Bodner, <u>et al.</u> , to experiment.....	124

Fig. 33	Cyclic loading test: cycles 1 and 10. Prediction of theory of Bodner, <u>et al.</u>	125
Fig. 34	Cyclic loading test: cycle 10. Comparison of theory of Bodner, <u>et al.</u> , to experiment....	126
Fig. 35	Cyclic loading test: cycle 1. Comparison of theory of Miller, <u>et al.</u> , to experiment....	128
Fig. 36	Cyclic loading test: cycles 1 and 10. Prediction of theory of Miller, <u>et al.</u>	129
Fig. 37	Cyclic loading test: cycle 10. Comparison of theory of Miller, <u>et al.</u> , to experiment....	130
Fig. 38	Cyclic loading test: cycle 1. Comparison of all theories to experiment.....	131
Fig. 39	Cyclic loading test: cycle 10. Comparison of all theories to experiment.....	132
Fig. 40	Experimental complex loading history.....	134
Fig. 41	Experimental complex loading response.....	135
Fig. 42	Complex loading test. Comparison of theory of Krieg, <u>et al.</u> , to experiment.....	136
Fig. 43	Complex loading test. Comparison of theory of Bodner, <u>et al.</u> , to experiment.....	137
Fig. 44	Complex loading test. Comparison of theory of Miller, <u>et al.</u> , to experiment.....	139
Fig. 45	Complex loading test. Comparison of all theories to experiment.....	140

INTRODUCTION

The prediction of inelastic material behavior in metals is a problem of great importance which has accordingly been given a great deal of attention by the research community in recent years. Recent technological advances require materials to function in severe chemical, mechanical, and thermal environments such as nuclear reactors and gas turbines. Superalloys have been developed that are able to sustain loads at extreme temperatures; however, due to this environment, these materials exhibit substantial complexity in their material constitution in that they are highly nonlinear, rate-dependent, temperature-dependent, and history-dependent.

Numerous theories have been proposed to predict the thermomechanical behavior of inelastic solids at elevated temperatures. These theories are usually based on one of the following concepts: 1) rate-dependent extensions of classical plasticity theory retaining the concept of a yield surface, 2) thermodynamics and/or nonlinear viscoelasticity theory, and 3) considerations of the

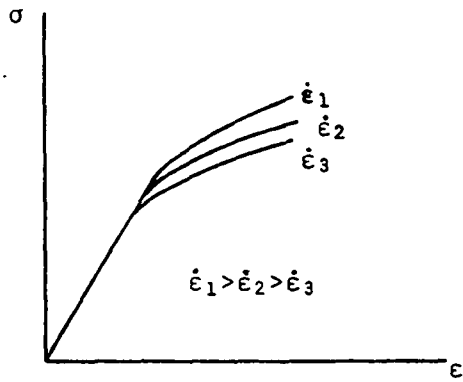
The style and format of this thesis follow the Journal of Engineering Materials and Technology.

microstructural behavior of the material. It is important that each of these theories be able to model diverse phenomena associated with inelastic deformation including anelasticity (completely recoverable time-dependent strain at zero load), the Bauschinger effect, cyclic strain hardening/softening, rate sensitivity, creep, relaxation, and tensile and compressive loading and unloading. These are illustrated in Figures 1 and 2.

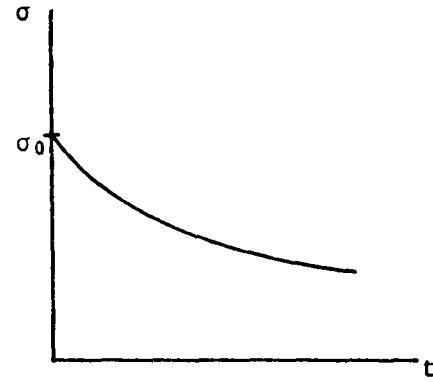
The purpose of this research is to review three theories based on considerations of microstructural behavior. Since each theory is proposed for a material and temperature of its authors' choosing, a set of experiments is performed by this author with a single candidate material in order to create a common experimental data base with which the mathematical representation of each model can be characterized. The theories are subsequently analyzed qualitatively and quantitatively over a range of material behavior to determine their suitability in predicting inelastic deformation.

This thesis opens with a short review of the mechanics of continua with internal state variables. This is followed by a literature review and, utilizing the framework of internal state variables, a detailed study of the models chosen for discussion. The experimental program associated with the research for this thesis is presented

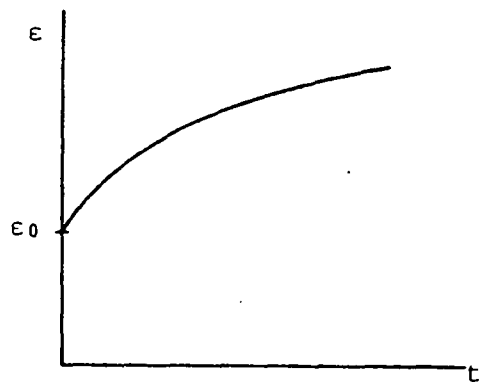
as an assessment of the experimental data base requirements for each model, accompanied by the results of the experiments. A uniaxial comparison of the predictive capabilities of the models follows and, finally, conclusions from the complete survey are presented.



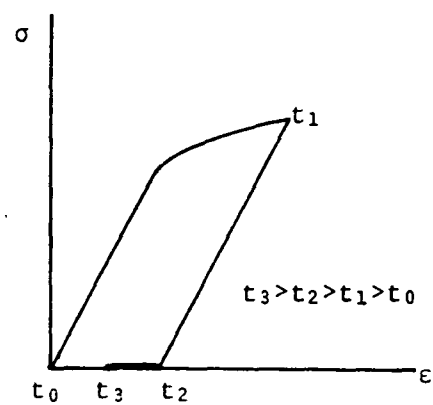
Rate sensitivity



Relaxation

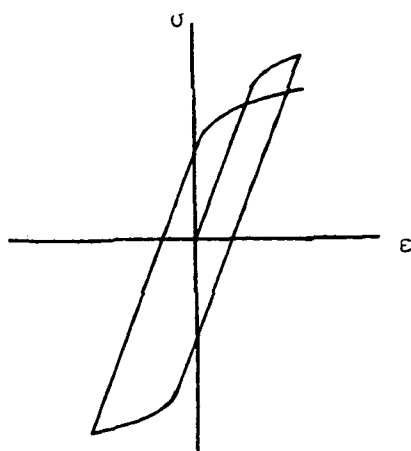


Creep

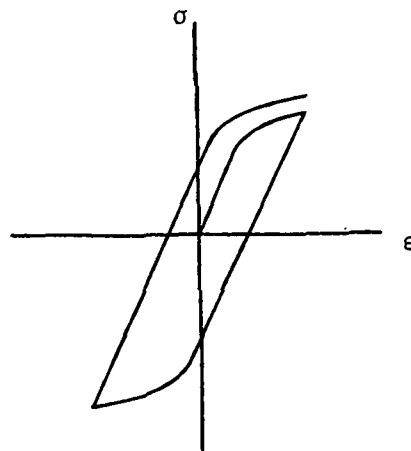


Anelasticity

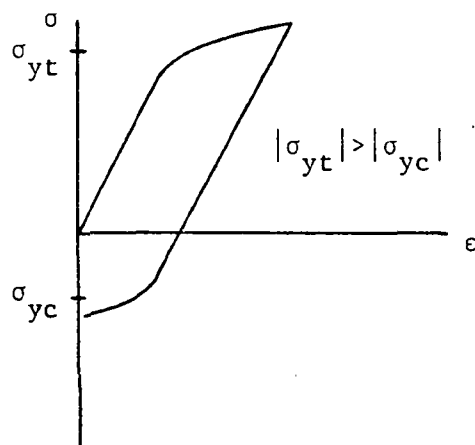
Fig. 1 Phenomena associated with inelastic deformation
(uniaxial loading)



Cyclic strain softening



Cyclic strain hardening



Bauschinger effect

Fig. 2 Phenomena associated with inelastic deformation
(cyclic loading)

THE EQUATION OF STATE APPROACH

The concept of internal state variables, sometimes called hidden variables, is gaining widespread usage in current research on the modelling of inelastic solids. Therefore, it is useful to construct a well-defined framework for internal state variable models which is based on continuum mechanics.

The concept of internal state variables was apparently first utilized in Onsager's work in thermodynamics [1,2] and has found numerous applications since the Second World War [3-12].

In the theory of internal state variables applied to solids, Coleman and Gurtin [3] defined the elastic field problem to be one in which the following state variables are required in order to characterize fully the state of a body at all points x_j and at all times t : *

- 1) the displacement field $u_i = u_i(x_j, t); \quad (1)$

* For convenience, only infinitesimal deformations will be considered here, although the general theory applies to finite deformations as well.

2) the stress tensor $\sigma_{ij} = \sigma_{ij}(x_k, t); \quad (2)$

3) the body force per unit mass $f_i = f_i(x_j, t); \quad (3)$

4) the internal energy per unit mass

$$u = u(x_j, t); \quad (4)$$

5) the heat supply per unit mass $r = r(x_j, t); \quad (5)$

6) the entropy per unit mass $s = s(x_j, t); \quad (6)$

7) the absolute temperature $T = T(x_j, t); \quad (7)$

and

8) the heat flux vector $q_i = q_i(x_j, t). \quad (8)$

Thermodynamic constraints will lead to the conclusion that, for elastic bodies, entropy is generated only through heat conduction [3]. For inelastic bodies, however, this conclusion cannot be drawn because additional entropy is generated. The state cannot be characterized solely from the observable state variables; rather, a set of internal state variables α_{ij}^k is also necessary, and these are determined by observation of the entire past history of

states of the body:

$$\alpha_{ij}^k = \alpha_{ij}^k(x_m, t), \quad (9)$$

where the superscript k ranges from one to the number of internal state variables necessary to characterize fully the state of the body. Although listed here as second order tensors, they may be tensors of other rank as well [13].

The method of Coleman and Noll [14] may be used to obtain the spatial and time distribution of the body force f_i and the heat supply r from the conservation of linear momentum and the conservation of energy, respectively, assuming the displacements u_i and the temperature T are specified independent variables. It is hypothesized subsequently that constitutive equations may be constructed for the remaining state variables in terms of u_i and T and their spatial derivatives:

$$\begin{aligned} \sigma_{ij}(x_k, t) = \\ \sigma_{ij}(\epsilon_{mn}(x_k, t), T(x_k, t), g_m(x_k, t), \alpha_{mn}^p(x_k, t)); \quad (10) \end{aligned}$$

$$u(x_k, t) =$$

$$u(\epsilon_{mn}(x_k, t), T(x_k, t), g_m(x_k, t), \alpha_{mn}^p(x_k, t)); \quad (11)$$

$$s(x_k, t) =$$

$$s(\epsilon_{mn}(x_k, t), T(x_k, t), g_m(x_k, t), \alpha_{mn}^p(x_k, t)); \quad (12)$$

$$q_i(x_k, t) =$$

$$q_i(\epsilon_{mn}(x_k, t), T(x_k, t), g_m(x_k, t), \alpha_{mn}^p(x_k, t)); \quad (13)$$

where g_m is the spatial temperature gradient $T_{,m}$ and

$$\epsilon_{ij} = \frac{1}{2}(u_{i,j} + u_{j,i}) \quad (14)$$

is the infinitesimal strain tensor. The form of equations (10) through (13) implies that all constitutive equations are evaluated in the specified state x_k and t . For this reason, σ_{ij} , u , s , and q_i are termed observable state variables since they can be determined from equations of state, even though there is an implied history dependence through the internal state variables α_{mn}^p . These are defined to be of the form:

$$\dot{\alpha}_{ij}^k = \Omega_{ij}^k(\epsilon_{mn}, T, g_m, \alpha_{mn}^p), \quad (15)$$

where time and spatial dependence have been dropped for notational convenience and the superscripts k and p range from one to the number of internal state variables necessary to characterize fully the state of the body. If equations (15) are integrable in t at all times, then they can be rewritten as

$$\alpha_{ij}^k(x_m, t) = \int_{-\infty}^t \Omega_{ij}^k(x_m, t') dt', \quad (16)$$

where t is the time of interest and t' is a dummy variable of integration.

The above framework has been shown to be applicable to crystalline solids [15,16] and further discussion of this subject is provided in reference [17].

On the basis of the Coleman-Mizel procedure [18] it can be shown that satisfaction of the first and second laws of thermodynamics will lead to the following conclusions:

$$h = u - Ts = h(\epsilon_{mn}, T, \alpha_{mn}^p), \quad (17)$$

where h is the Helmholtz free energy;

$$\sigma_{kl} = \rho \partial h / \partial \epsilon_{kl}; \quad (18)$$

$$s = -\partial h / \partial T; \quad (19)$$

and

$$q_i = -k_{ij}g_j + O(g_j), \quad (20)$$

where k_{ij} is the thermal conductivity tensor. Although further results are obtainable [3,15-17], they are not pertinent to the current research. The importance of the results above is that, in order to construct a complete description of constitutive equations (10) through (13) and (15), it is necessary only to prescribe the Helmholtz free energy. In order to describe the class of materials discussed herein, the free energy is expanded in terms of the elastic strain tensor ϵ_{ij}^E and the temperature T in a second order Taylor series as follows:

$$h = h_R + \epsilon_{ij}^E D_{ijkl} \epsilon_{kl}^E / 2\rho - c_V (T - T_R) / 2T, \quad (21)$$

where the subscript R refers to quantities in the reference state, D_{ijkl} is the linear elastic modulus tensor, $c_V = -T(\partial^2 h / \partial T^2)$ is the specific heat at constant elastic volume, and

$$\epsilon_{ij}^E = \epsilon_{ij} - \epsilon_{ij}^I - \epsilon_{ij}^T, \quad (22)$$

where ϵ_{ij}^T is the thermal strain tensor and ϵ_{ij}^I is the inelastic strain tensor, which can be considered to be an internal state variable [15,16,18-21]. Substitution of equation (21) into (18) will result in

$$\sigma_{kl} = D_{klmn} (\epsilon_{mn} - \epsilon_{mn}^I - \epsilon_{mn}^T). \quad (23)$$

The above equations, together with internal state variable growth laws (15), will be shown to be a suitable framework for comparison of all the models discussed herein.

Theoretically, constitutive equations (10) through (13) and (15) are applicable to fixed infinitesimal material points. In practical terms however, it is not possible to construct experiments on material points since the continuum assumption becomes invalid at the microscopic level. Rather, it is considered acceptable to construct constitutive equations by subjecting local specimens to surface deformations (or tractions) which lead to spatially homogeneous stresses and strains. In this manner, a local average of the pointwise observable state variables can be determined directly from the effects on the boundaries of the specimen.

As shown in Figure 3, the scale of the smallest dimension of a local specimen is generally assumed to be at least one order of magnitude larger than the scale of the

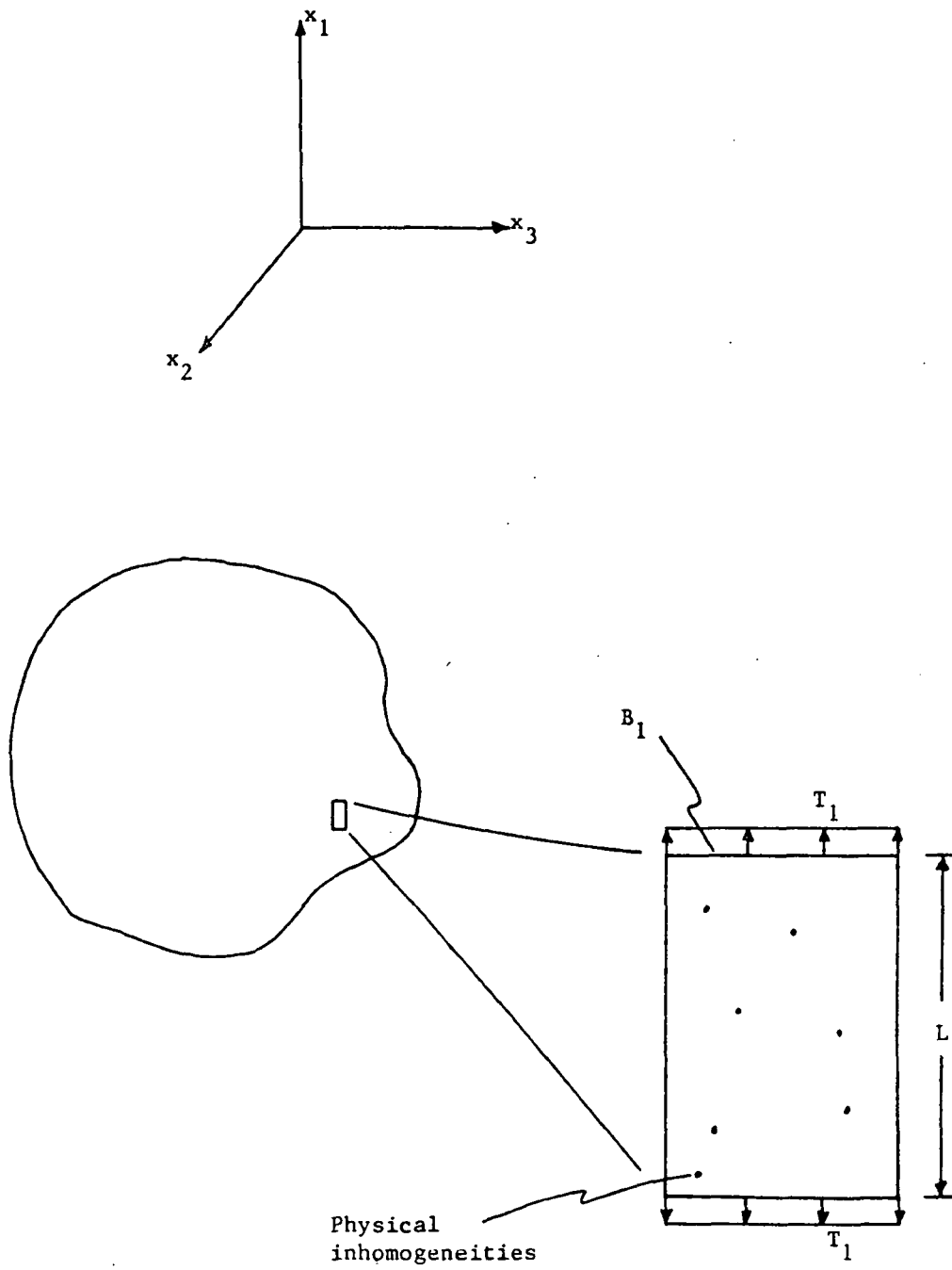


Fig. 3 The relationship between local inhomogeneities and the continuum assumption

largest material inhomogeneity, while the scale of the largest dimension of the local specimen is much smaller than the scale of the domain of interest. The former preserves the continuum assumption, while the latter conserves the notion that constitutive equations are indeed pointwise in nature. The local constitutive equations that result from experimentation are assumed to be of the same form as pointwise equations (10) through (13) and (15); for example,

$$\bar{\sigma}_{11} = \bar{\sigma}_{11}(\bar{\epsilon}_{11}, \bar{T}, \bar{\alpha}_{mn}^p), \quad (24)$$

where

$$\bar{\sigma}_{11} = \frac{1}{A} \int_{B_1} \sigma_{11} dx_2 dx_3, \quad (25)$$

$$\bar{\epsilon}_{11} = \frac{1}{L} \int_L \epsilon_{11} dx_1, \quad (26)$$

and

$$\bar{T} = T(a_1, a_2, a_3), \quad (27)$$

where L is the length of the local specimen, A is the cross-sectional area in the x_2 - x_3 plane, (a_1, a_2, a_3) is an arbitrary point on the surface of the specimen, and

$$\bar{\alpha}_{mn}^p = \frac{1}{V} \int_V \alpha_{mn}^p dx_1 dx_2 dx_3. \quad (28)$$

It is then assumed that equation (24) is a suitable replacement for equation (10). There are obvious shortcomings in this assumption in that equation (24) represents a solution to a boundary value problem. This implies volume averaging of local balance laws, which violates the local nature of constitutive equations. In addition, there may be a question of uniqueness resulting from the fact that more than one global state of a given internal state variable will map into the globally averaged state variable described by equations (28). However, assuming that the scale of inhomogeneities is small and that the distribution of α_{mn}^p is random, the specimen will be statistically homogeneous and the relation between α_{mn}^p and $\bar{\alpha}_{mn}^p$ reasonably one-to-one. The above procedure remains the only reasonable method for constructing constitutive equations from experimental data bases.

LITERATURE REVIEW AND GENERAL DISCUSSION OF MODELS

Man's curiosity about his environment and his constant striving to harness the power and resources of nature with increasing efficiency have been the driving force behind the study of the laws of nature and the attempts to use these laws to predict the solutions of many problems.

The theory of elasticity dates to the 17th century with Robert Hooke's discovery that the tension in a spring is directly proportional to its extension. This heralded the beginning of the characterization of mechanical behavior of materials using mathematical constitutive models. Contributions to the theory of elasticity were also made by Galileo, the Bernoullis, Navier, Cauchy, Euler, and Saint-Venant, to name a few [22].

Classical Plasticity Models

Often only a small part of material deformation is elastic and, in general, a material will not behave elastically at large strains. Consequently, in 1864 Tresca [23] proposed a criterion to predict the onset of inelastic deformation in metals based on the maximum shear stress reaching a critical value. This was followed in 1913 by von Mises [24] with a yield criterion based on an equivalent

stress state reaching a critical value; this has been interpreted as the elastic shear strain energy reaching a critical value [25].

Independently of each other, Levy [26] and von Mises [24] formed the basis of classical plasticity by proposing a three-dimensional relationship between the strain increment and the stress tensor which became known as the Levy-Mises equations:

$$d\epsilon_{ij} = d\lambda \sigma'_{ij}, \quad (29)$$

where $d\epsilon_{ij}$ is the total strain increment, $d\lambda$ is a scalar, and σ'_{ij} is the deviatoric stress tensor, given by

$$\sigma'_{ij} = \sigma_{ij} - \frac{1}{3}\sigma_{kk}\delta_{ij} \quad (30)$$

where δ_{ij} is the Kronecker delta. In equations (29), the elastic strain component is assumed to be negligible; these equations consequently describe a fictitious, rigid, perfectly plastic material. Equations (29) were extended to take into account the elastic strain component by Prandtl [27] in 1924, who solved the plane stress case, and by Reuss [28] in 1930, who generalized the equations to three dimensions:

$$d\epsilon_{ij}^P = d\lambda \sigma'_{ij}, \quad (31)$$

where $d\epsilon_{ij}^P$ is the plastic strain component and $d\lambda$ is a scalar history-dependent material property. The total strain increment $d\epsilon_{ij}$ is then assumed to be the sum of the plastic strain component $d\epsilon_{ij}^P$ and the elastic strain component $d\epsilon_{ij}^E$.

These developments enabled the classical plasticity theory to model elastic and rate-independent inelastic deformation fairly accurately for most metals with only a few restrictions. These were that the material be subjected to monotonically increasing loads and low non-transient homologous temperatures; that is, temperatures less than three tenths of the absolute melting temperature. At higher temperatures, however, rate dependence of material behavior becomes significant, limiting the use of the existing plasticity theory.

Rate dependence was initially treated as an extension of classical plasticity theory by Bingham [29] in 1922 by using the concept of a yield function dependent on the excess of the stress intensity over the yield stress for the case of simple shear. This was generalized by Hohenemser and Prager [30] in 1932 for the three-dimensional case. Further progress in plasticity theories was slow and advanced vastly and diversely only

after completion of World War II. Prager [31] and Ziegler [32] proposed work-hardening rules for rate-independent plasticity to allow the yield surface to translate to model kinematic hardening. Drucker's stability postulate [33] serves as a basis for the incremental theories of plasticity, in which the plastic strain increment is determined by the stress and the stress increment. Rate-dependent plasticity models proposed in the postwar period included those by Freudenthal [34], Malvern [35,36], who constructed a one-dimensional equation relating the stress increment to the strain rate, Lubliner [37], who modified Malvern's equation to include a limiting stress-strain curve, and Perzyna [38-41], who generalized Malvern's equations to three dimensions and finite strains.

Many classical plasticity models have been extended to include rate dependence by adding an uncoupled rate-dependent strain component to the rate-independent strain component. No observable difference exists between the physical mechanisms causing these phenomena, however, and it has been argued that the two terms should be combined [42]. Naghdi and Murch [43] attempted to include rate dependence by introducing interdependent, although not unified, plastic and viscoelastic strain components.

Classical plasticity theories are usually described by

$$\sigma_{ij} = D_{ijmn} (\epsilon_{mn} - \epsilon_{mn}^I - \epsilon_{mn}^T), \quad (32)$$

where D_{ijmn} is the linear elastic modulus tensor, ϵ_{mn}^T is the thermal strain, and ϵ_{mn}^I , the inelastic strain, is given by

$$\dot{\epsilon}_{mn}^I = \dot{\lambda} \sigma F / \sigma \sigma_{mn}, \quad (33)$$

where $\dot{\lambda}$ is a scalar valued function of state and F is a scalar valued function for inelastic behavior often taken to be the yield function. If F is described by the von Mises yield criterion [24], given by

$$F(\sigma_{ij} - \alpha_{ij}) = \frac{1}{2}(\sigma_{ij} - \alpha_{ij})(\sigma_{ij} - \alpha_{ij}) = k^2, \quad (34)$$

where α_{ij} is a tensor describing the yield surface center in stress space and k is a constant representing the yield surface size, then equations (33) can be written as

$$\dot{\epsilon}_{ij}^I = \dot{\lambda} (\sigma_{ij} - \alpha_{ij}), \quad (35)$$

resulting in a kinematic hardening model with constant yield surface size. Furthermore, if the yield surface translation is derived from the Ziegler modification [32] of the Prager work-hardening rule [31], it may be described

by

$$\dot{\alpha}_{ij} = \dot{\mu} (\sigma_{ij} - \alpha_{ij}), \quad (36)$$

where $\dot{\mu}$ is a scalar valued function of state.

By use of equations (32), equations (35) and (36) can be shown to be consistent with growth laws (15). It can then be seen that classical plasticity theories are consistent with the thermodynamic framework developed in the equation of state approach.

Recently proposed theories include those by Snyder and Bathe [44], Yamada and Sakurai [45], Allen and Haisler [46,47], which attempts to model transient temperature effects, Zienkiewicz and Corneau [48], and Robinson [49]. Bodner and his associates proposed a model [50] which uses a flow law similar to equations (31), although the internal state variable growth laws are based on microstructural considerations. Robinson's model and Bodner's model are still under active development.

Nonlinear Viscoelasticity Models

Nonlinear viscoelasticity models are usually based on thermodynamics and/or mechanical analogs composed of springs and dashpot combinations such as the three parameter standard solid, shown in Figure 4. In 1954, Biot

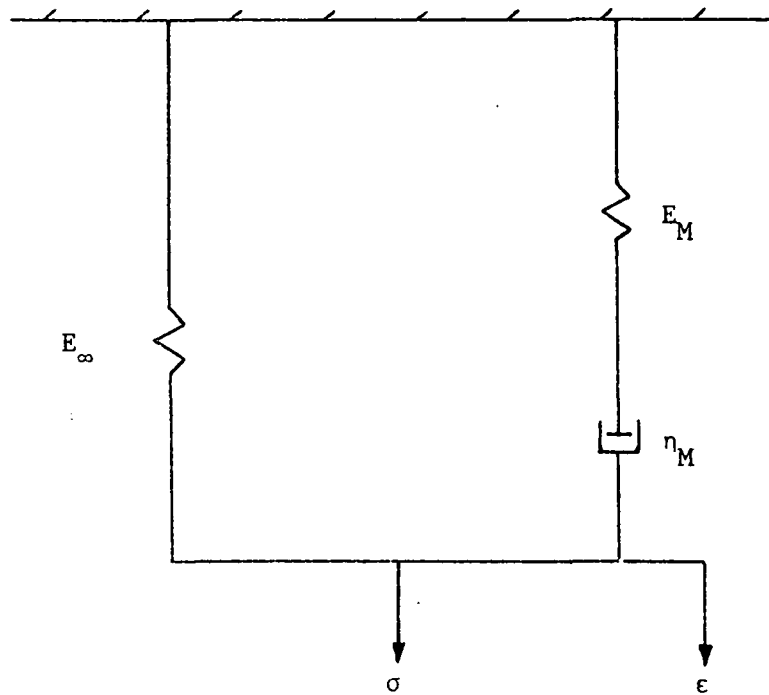


Fig. 4 The three parameter standard solid

[6,7] proposed a theory of linear thermoviscoelasticity based on the principles of irreversible thermodynamics. Schapery [12] later modified this to include nonlinear behavior and introduced a reduced time scale to solve the resulting highly nonlinear equations. Valanis [51-53] proposed a viscoplasticity theory, termed the endochronic theory, which includes a history-dependent reduced time parameter. This was later shown to be a special case of Schapery's model [54]. Some other models based on thermodynamics are those of Coleman and Noll [55,14], Green and Rivlin [56], and Green and Naghdi [57]. These tend to be quite complex in nature and difficult to solve.

Many of the recent models are based on variations of the three parameter standard solid. The standard solid shown in Figure 4 has been demonstrated to be an appropriate representation for thermoviscoplastic metals if the springs and dashpot are nonlinearized [58,59]. The governing differential equation for this solid is

$$\sigma + (\eta_M/E_M)\dot{\sigma} = E_\infty \epsilon + (\eta_M/E_M) (E_M + E_\infty)\dot{\epsilon}. \quad (37)$$

This may be rewritten in the equivalent form

$$\dot{\epsilon} = \dot{\sigma}/(E_M + E_\infty) + E_M/[\eta_M(E_M + E_\infty)] (\sigma - E_\infty \epsilon). \quad (38)$$

In accordance with the instantaneous linear behavior of metals, it is assumed that

$$E_M + E_\infty = E = \text{Elastic modulus} = \text{constant}, \quad (39)$$

and equation (38) becomes

$$\epsilon = \frac{\sigma}{E} + \epsilon^I, \quad (40)$$

where ϵ^I is the inelastic strain, given by

$$\dot{\epsilon} = (E_M / \eta_M E) (\sigma - E_\infty \epsilon). \quad (41)$$

The nonlinearity of the springs and dashpot can be introduced by considering a multi-axial extension of equation (37):

$$\sigma_{pq} + K_{pqmn} \dot{\epsilon}_{mn} = G_{pqmn} \epsilon_{mn} + M_{pqmn} \dot{\epsilon}_{mn}. \quad (42)$$

In order to model metals, K_{pqmn} , G_{pqmn} , and M_{pqmn} are nonlinear material functions determined from experimental data. In addition, constraint (39) requires that

$$K_{ijmn}^{-1} M_{mnkl} = D_{ijkl}, \quad (43)$$

where D_{ijkl} is the linear elastic modulus tensor.

Equations (42) and (43) lead to

$$\sigma_{ij} = D_{ijmn} (\epsilon_{mn} - \epsilon_{mn}^I - \epsilon_{mn}^T), \quad (44)$$

where the inelastic strain ϵ_{ij}^I is given by

$$\dot{\epsilon}_{ij}^I = M_{ijkl}^{-1} (\dot{\sigma}_{kl} - G_{klmn} \dot{\epsilon}_{mn}). \quad (45)$$

Substitution of equations (44) into (45) will result in equations consistent with growth laws (15). It can then be seen that nonlinear viscoelasticity models are consistent with the thermodynamic framework developed earlier in the equation of state approach.

Some recent models which are based on nonlinear modifications of the three parameter standard solid are those of Krempl, et al. [59-66], and Walker [58,67,68].

Microstructural Models

Microstructural models have generated increased interest in recent years because their formulation is based on microphysical considerations rather than a statistically averaged macroscopic view. The primary micromechanisms which cause inelastic deformation are dislocation glide and climb, deformation twinning, diffusion, grain boundary

sliding, and microvoid growth and coalescence. These mechanisms are difficult to model individually and are usually reduced to three more general mechanisms: dislocation arrangement, dislocation density, and damage. In the concept of microphenomenology it is assumed that the three mechanisms can be characterized by internal state variables. One internal state variable represents the back stress for modelling the dislocation arrangement. Another internal state variable, termed the drag stress, models dislocation density. In addition, it can be argued that the inelastic strain represents the third internal state variable [15,16,19]. Current research is in progress to account for damage in materials using a fourth internal state variable [69-71], although it is difficult to distinguish between damage and the drag stress since both are primarily stiffness-reducing parameters.

Early research in this field was performed by Coble [72], Nabarro [73], and Herring [74] in their work on diffusion-controlled creep. Other important contributions were made by Sherby, et al. [75-77], Garofalo [78], Argon [42], Weertman [79], Alden [80], Kocks [81], and Hart [82].

Mukherjee, et al. [83], studied the effectiveness of using a power law of the following form to model dislocation climb:

$$\dot{\epsilon}^I = D A (\sigma/E)^n, \quad (46)$$

where D is the self-diffusivity, E is Young's modulus, and A and n are temperature-dependent material parameters. The authors concluded, however, that a model in terms of a single dislocation mechanism may not completely characterize high-temperature creep.

Gibbs [84] proposed a two-internal-state-variable theory in which the inelastic strain rate is characterized by an exponential function of temperature and an effective stress:

$$\dot{\epsilon}^I = A^* \exp\{-[Q_c - (\sigma - \sigma_a)lb^2]/kT\}, \quad (47)$$

where A^* is a structure factor, Q_c is the dislocation core diffusion energy, k is the activation energy, T is the absolute temperature, b is the Burger's vector, and σ_a and l are internal state variables representing, respectively, back stress and drag stress.

It is generally recognized [85] that at intermediate to high stresses and at temperatures above $0.5T_m$, where T_m is the absolute melting temperature, stress is related to the inelastic strain rate by a power law of the form

$$\dot{\epsilon}^I = A \sigma^n, \quad (48)$$

where A and n are constants. At very high stress levels, the relationship is

$$\dot{\epsilon}^I = B \exp(m\sigma), \quad (49)$$

where B and m are constants. Power law and exponential relationships represent limiting cases for the more general empirical relationship

$$\dot{\epsilon}^I = C [\sinh(k\sigma)]^p, \quad (50)$$

where C, p, and k are constants. Equation (50) approximates a power law when $k\sigma < 0.8$, but it approximates an exponential curve when $k\sigma > 1.2$. See Figure 5 for a comparison of the forms of equations (48), (49), and (50).

Microstructural models are usually similar in nature, differing only in the proposed relationship between stress and inelastic strain (that is, equations (48), (49), or (50)) and in the proposed internal state variable growth laws. The growth laws for the internal state variables representing the back stress and the drag stress usually follow the framework established by Bailey [86] and Orowan [87] in which a hardening term, proceeding with accumulated deformation, competes simultaneously with a softening or recovery term, proceeding with time. For example, the

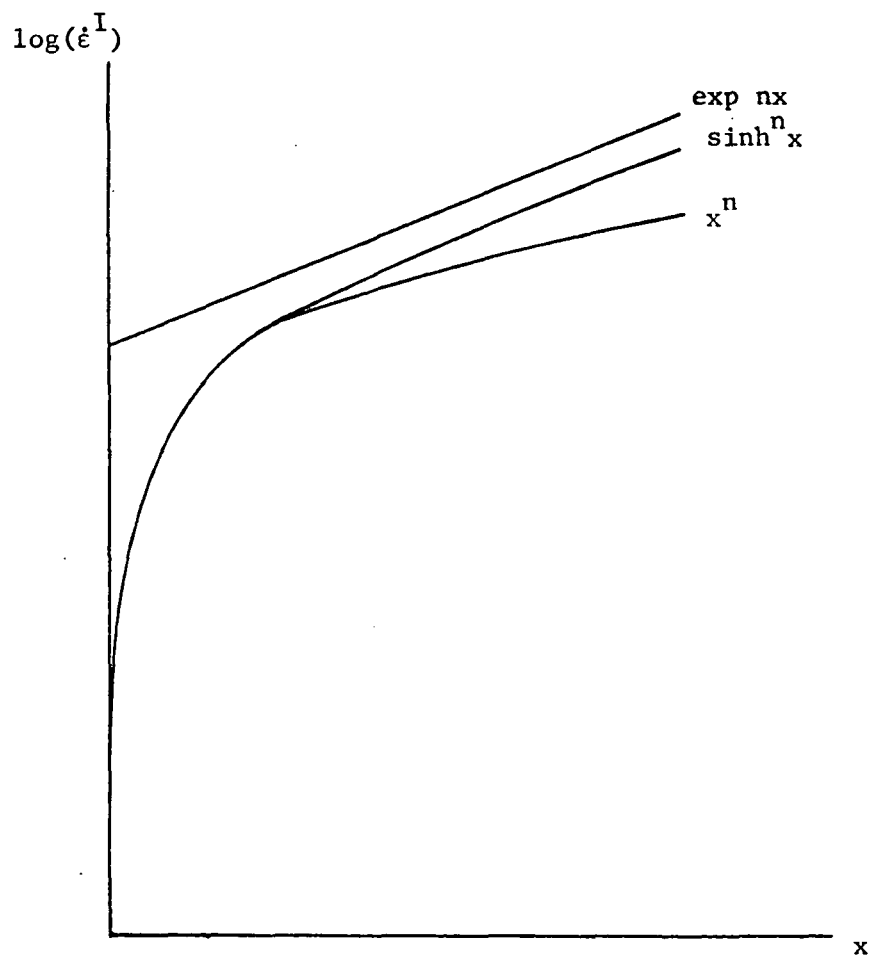


Fig. 5 A comparison of the hyperbolic sine, power law, and exponential forms of the inelastic strain rate equation

isothermal model proposed by Krieg, et al. [88], is given in its uniaxial form by

$$\sigma = E (\epsilon - \epsilon^I), \quad (51)$$

where the inelastic strain is given by

$$\dot{\epsilon}^I = c_1 [|\sigma - \alpha_1|/\alpha_2] \operatorname{sgn}(\sigma - \alpha_1), \quad (52)$$

where the growth laws for the back stress α_1 and the drag stress α_2 are given as the differences of hardening and softening rates:

$$\dot{\alpha}_1 = c_3 \dot{\epsilon}^I - c_4 \alpha_1^2 [\exp(c_5 \alpha_1^2) - 1] \operatorname{sgn}(\alpha_1) \quad (53)$$

and

$$\dot{\alpha}_2 = c_6 |\dot{\epsilon}^I| - c_7 (\alpha_2 - \alpha_{2_0})^n, \quad (54)$$

where c_1 , c_2 , c_3 , c_4 , c_5 , c_6 , c_7 , n , and α_{2_0} are temperature-dependent material constants, and $\operatorname{sgn}()$ is the signum function.

Substituting equation (51) into (52) will result in equations consistent with growth laws (15). In addition, since equations (53) and (54) are consistent with growth

laws (15), it can be seen that microstructural models agree with the thermodynamic framework developed earlier in the equation of state approach. Cescotto and Leckie [89] proposed a model which has the interesting feature that no particular forms are assumed for the inelastic strain rate function and the hardening and recovery functions; only weak hypotheses are required and the functions are defined experimentally.

Other recently proposed models include those of Miller, et al. [90], in which a hyperbolic sine function is used for the stress-inelastic strain rate equation, Walker [58], in which a power law is used for the inelastic strain rate equation, and Bodner [50], in which an exponential function is used. An interesting aspect of these last two models is that, although the respective growth laws for the back stress and the drag stress are formulated from microstructural considerations, Walker's inelastic strain rate equation is based on a nonlinear modification of a three parameter viscoelastic solid, while Bodner's inelastic strain rate equation is based on a flow law similar to the Prandtl-Reuss equation of classical plasticity (see the literature reviews on nonlinear viscoelasticity models and classical plasticity models, respectively).

Since theories based on microstructural considerations

have been given a great deal of study in recent years, the theories chosen for comparison are taken from this field and are those of Krieg, et al. [88], Miller, et al. [90], and Bodner, et al. [50]. The motivation for the choice of these three models is that they are still under development; they have been cast in a common thermodynamic framework; the authors have included in their theories detailed accounts of methods of determination of the material constants; these models have received considerable attention [20,68,91-93]; and research is in progress to extend these isothermal models to include transient temperature response [68,91,94].

KRIEG, SWEARENGEN, AND ROHDE'S MODEL

Chronological Development

In 1977, Krieg [95] cast several current unified constitutive models into the common framework of a skeletal model in which general similarities, such as the use of competing hardening and recovery rates for internal state variable growth laws, are noted. These models include those of Bodner, et al., Robinson, et al., Hart, Lagneborg, Miller, Pasley and Wells, Ponter and Leckie, and an early development of Krieg's model, which is described as a composite of the aforementioned models. All hardening and softening functions are taken to be constants in the skeletal model in order to make observations about difficulties encountered in numerically integrating mathematically stiff constitutive equations. Finally, integration techniques are proposed to alleviate these difficulties.

In a development of this model, Krieg, Swearengen, and Rohde [88] proposed a power-law kinetic relation in multiaxial form to model pure aluminum at room temperature. This model has three internal state variables: the inelastic strain, the back stress and the drag stress. The growth laws of the back stress and the drag stress are formulated in the usual hardening rate/recovery rate

format. The hardening functions have not been defined and are assumed to be constant; recovery is considered to be a thermally-activated process and dynamic recovery is not included. Furthermore, the response of pure aluminum at room temperature is very nearly kinematic and, as a consequence, the drag stress (the isotropic hardening variable) is taken to be constant. Krieg, et al., present a test method in which all material constants, except Young's modulus, are calculated by determining values of the back stress from a set of stress-drop tests. In this test, a portion of the load on a specimen during secondary creep is removed and the resulting strain transient is recorded. The authors have obtained reasonable results for pure aluminum at room temperature for various load histories, although the predicted hysteresis loops are "over-square" and the model's use is limited in high strain rate ranges.

In 1982, Jones, et al. [96], noted that, while most unified creep-plasticity models require an extensive number of tests for characterization of material parameters, the model proposed by Krieg, et al., requires only a set of stress-drop tests. It is pointed out that, although simple in concept, the stress-drop test is difficult to perform in practice. The critical measurement in this test, a zero strain rate after unloading or merely the absence of a

resolvable strain rate, results in a strong dependence of the parameters on experimental resolution. The authors present the design of a test apparatus to minimize these effects. In addition, there appear to be differing opinions in the literature on the response of the creep rate immediately after unloading. Jones, et al., conclude that stress-drop testing should be performed with great care.

In subsequent research in 1983, Jones and Rohde [97] refer to a new technique to reduce stress-drop data which alleviates the difficulties mentioned above. Rather than attempting to measure a zero strain rate, this method [98] uses a comparison of the instantaneous strain change and the maximum strain change after unloading. This method appears to simplify the calculations considerably and merits further study.

General Theory

In their unified creep-plasticity model, Krieg, Swearingen, and Rohde [88] state that inelastic deformation can be caused by: 1) thermally-activated, stress-assisted penetration of short-range obstacles to dislocation motion, 2) generation and immobilization of dislocations, leading to increases in dislocation density, stored elastic energy, and the flow stress, and 3) stress-assisted thermal

rearrangement of dislocations to reduce long-range internal stresses. Krieg, et al., note that strain hardening at low to intermediate homologous temperatures (below $0.5T_m$, where T_m is the absolute melting temperature) is both isotropic and kinematic. Isotropic hardening, manifested by an increase in the height of the reversed strain hysteresis loop, has its microstructural origins in dislocation obstacle interaction, while kinematic hardening, manifested by the Bauschinger effect, has its origins in dislocation pile-ups. Mathematical descriptions of this behavior require two internal state variables.

Deformation kinetics resulting from thermally-activated processes are usually described by Arrhenius or hyperbolic sine functions; however, over a wide range of stresses, the analytically simpler power law provides a good approximation. This motivated Krieg, et al., to propose the following flow rule in multiaxial form in deviatoric stress-strain space:

$$\dot{\underline{\epsilon}}^I = \dot{\epsilon}_0 \left(|\underline{\zeta}|/R \right)^m \left(\underline{\zeta}/|\underline{\zeta}| \right), \quad (55)$$

where $\dot{\underline{\epsilon}}^I$ is the inelastic strain rate vector, $||$ is the Euclidean vector norm, $\dot{\epsilon}_0$ and m are temperature-dependent material constants, and R is the drag stress, an internal state variable which accounts for isotropic hardening. The

effective stress ζ is given by

$$\zeta = \underline{s} - \underline{\alpha}, \quad (56)$$

where $\underline{\alpha}$ is the back stress, an internal state variable which accounts for kinematic hardening; and \underline{s} is the applied stress. The increase in flow stress associated with an increase in hardening is taken to be proportional to inelastic strain. Recovery is associated with dislocation escape from glide planes by climb or cross-slip. In the absence of external loads, this escape reduces the internal stresses through annealing; in the presence of external loads, this escape permits additional inelastic deformation through creep or dynamic recovery. The evolution of $\underline{\alpha}$ and R is given by the difference between hardening and recovery rates as

$$\dot{\underline{\alpha}} = A_{\alpha} \dot{\underline{\epsilon}}^I - r_{\alpha} (\underline{\alpha}/|\underline{\alpha}|) \quad (57)$$

and

$$\dot{R} = A_R |\dot{\underline{\epsilon}}^I| - r_R, \quad (58)$$

where A_{α} and A_R are the hardening functions, and r_{α} and r_R are the recovery functions.

Krieg, et al., assume the hardening functions A_{α} and A_R

to be constant. The recovery rates are assumed to be proportional to dislocation velocity of escape and inversely proportional to the escape distance [99], where the velocity and distance depend on the magnitude of the back and drag stresses. Since annealing rate depends on hardening mechanisms, one would expect the kinetics of recovery for α and for R to be different. A unique feature of this model is that it incorporates different physically-based recovery kinetics for each internal variable.

Dislocation processes associated with the drag stress are formations of dislocation tangles, or networks. Temperature-dependent changes in the networks can be described by the climb recovery model of Friedel [99]:

$$r_R = -K_1 (R^n/kT) \exp(-U/kT), \quad (59)$$

where K_1 and n are material constants, k is the gas constant, T is the absolute temperature, and U is the activation energy associated with the particular micromechanism of softening.

Dislocation processes associated with the back stress are pile-ups or cell-wall bowing. Although both cross-slip and climb are recovery mechanisms, only screw dislocations can cross-slip and, consequently, the model's authors feel

that recovery by climb is a more complete description. The kinetics of this process are again given by Friedel [99]:

$$\dot{r}_\alpha = -K_2 \alpha^2 [\exp(K_3 \alpha^2 / kT) - 1], \quad (60)$$

where K_2 and K_3 are material constants.

By use of equations (60), in multiaxial form, and (59), equations (57) and (58) become

$$\dot{\underline{\alpha}} = A_\alpha \dot{\underline{\epsilon}}^I - |\underline{\alpha}| K_2 [\exp(K_3 |\underline{\alpha}|^2 / kT) - 1] \quad (61)$$

and

$$\dot{R} = A_R |\dot{\underline{\epsilon}}^I| - K_1 [(R - R_0)^n / T] \exp(-U/kT), \quad (62)$$

where R_0 represents an isotropic annealed state.

For conditions of uniaxial stress and constant temperature, equations (55), (61), and (62) reduce to

$$\dot{\epsilon}^I = \bar{c}_1 |\zeta/R|^{c_2} \operatorname{sgn}(\zeta), \quad (63)$$

$$\dot{\alpha} = c_3 \dot{\epsilon}^I - c_4 \alpha^2 [\exp(c_5 \alpha^2) - 1] \operatorname{sgn}(\alpha), \quad (64)$$

and

$$\dot{R} = c_6 |\dot{\epsilon}^I| - c_7 (R - R_0)^n, \quad (65)$$

where $c_1, c_2, c_3, c_4, c_5, c_6, c_7, n$, and R_0 are temperature-dependent material constants, $\text{sgn}()$ is the signum function, and the effective stress ζ is

$$\zeta = \sigma - \alpha. \quad (66)$$

Krieg, et al., simplify the model further by assuming a kinematic work-hardening material so that the isotropic hardening variable R will remain constant. Equation (65) can then be omitted and the uniaxial isothermal form of the model becomes

$$\sigma = E (\epsilon - \epsilon^I), \quad (67)$$

where ϵ^I is given by

$$\dot{\epsilon}^I = c_1 |\zeta|^{c_2} \text{sgn}(\zeta), \quad (68)$$

and

$$\dot{\alpha} = c_3 \dot{\epsilon}^I - c_4 \alpha^2 [\exp(c_5 \alpha^2) - 1] \text{sgn}(\alpha), \quad (69)$$

where c_1, c_2, c_3, c_4 , and c_5 are-temperature dependent

material constants, and the effective stress ζ is given by equation (66).

Evaluation Of Material Constants

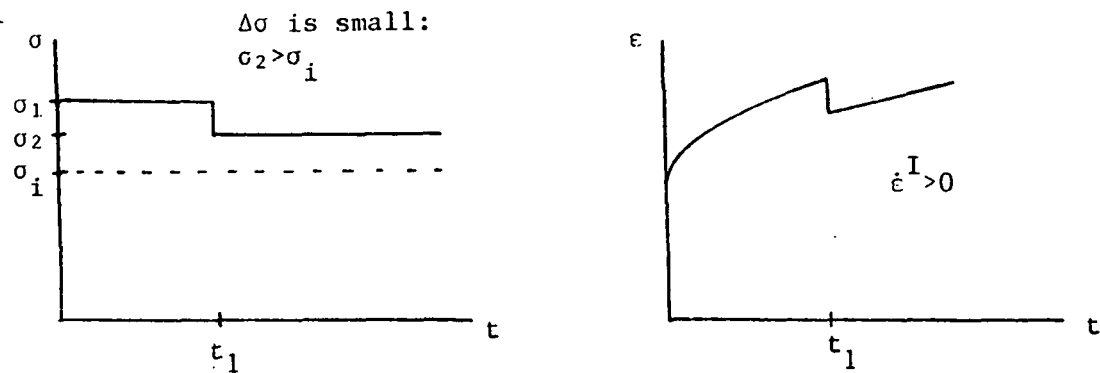
Krieg, et al., present an experimental test and data reduction procedure which allows all constants, except the elastic modulus E , to be determined from a set of stress-drop tests, sometimes called strain transient dip tests.

Before describing the procedure to evaluate the material constants, it would be instructive to review the somewhat controversial stress-drop test. High-temperature creep can be characterized in terms of an internal stress and an effective stress [100], where the internal (or back) stress is the driving force for recovery, and the effective stress (the difference between the applied and back stress) is the driving force for dislocation glide. Consequently, it is of interest to be able to determine the back stress.

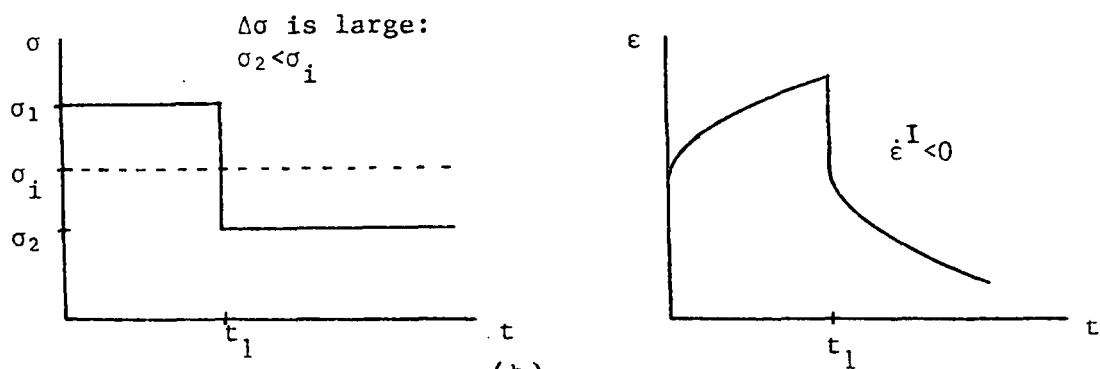
Since the back stress is a result of the dynamic balance between strain hardening and recovery, the back stress begins to change when the applied stress is changed. Therefore, the transient response examined should be of short enough duration to ensure a structure which is still reasonably representative of the steady-state structure; i.e., a structure in which the value of the back stress has

not changed appreciably from its steady-state value. A technique described by Ahlquist and Nix [100,101] involves the dynamic measurement of back stresses by rapidly reducing the applied stress from the steady-state value σ_1 and measuring the strain rate immediately after the reduction. For a small reduction in stress $\Delta\sigma$, the strain rate immediately after the reduction is positive as shown in Figure 6a. For a large reduction in stress $\Delta\sigma$, the strain rate is negative as shown in Figure 6b. For an intermediate reduction in stress $\Delta\sigma$, the strain rate is zero and the new stress level σ_2 describes the mean internal (or back) stress σ_1 . After a short time, recovery events reduce the back stress, yielding a positive strain rate. As can be seen from Figure 7, it may be necessary to load and unload a sample several times during a test before finding the stress reduction that will give the back stress.

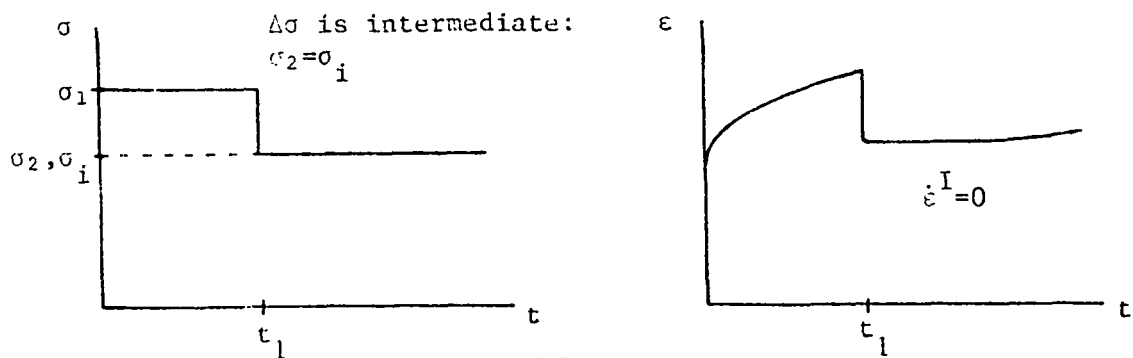
This procedure for determining the back stress applies to thermally-activated creep. However, there are different hypotheses for creep deformation where the concept of a back stress may become questionable. Consequently, these hypotheses give differing predictions of the transient response after a stress drop. Poirier [102] summarizes these into four categories, as shown in Figure 8, where the responses due to stress drops of different magnitudes have



(a)



(b)



(c)

Fig. 6 Strain response for rapid stress reductions during steady-state creep

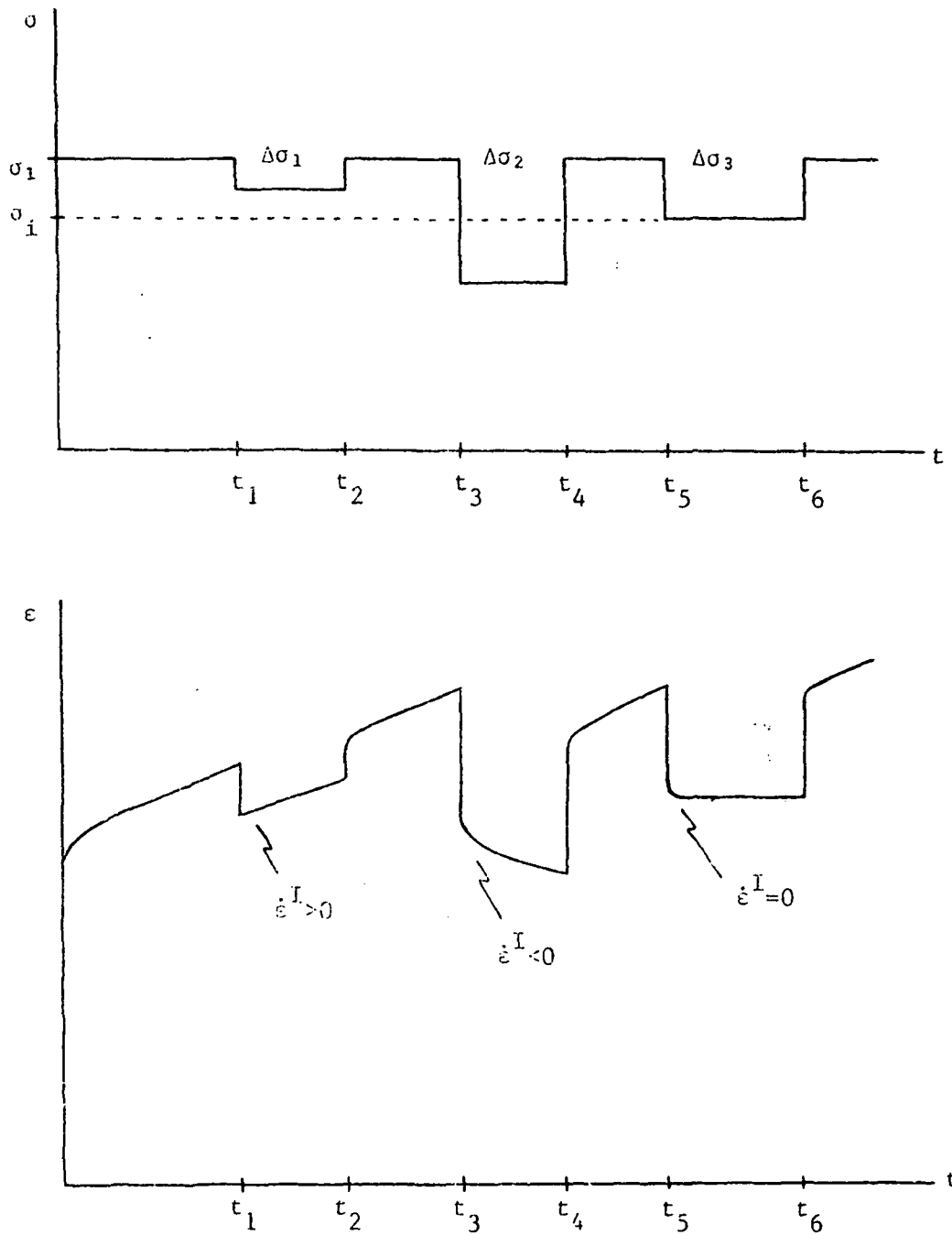


Fig. 7 A stress-drop test

been superposed.

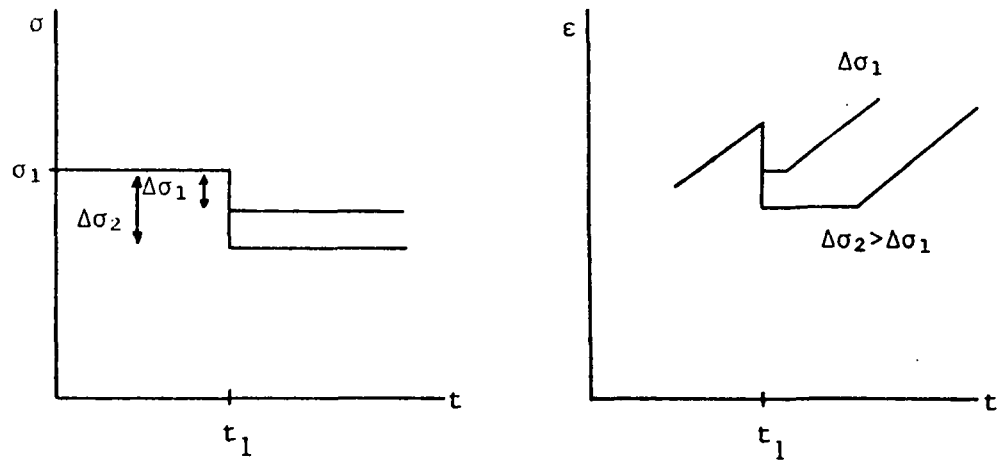
The athermal recovery-controlled creep case is characterized by: 1) the absence of an effective stress, 2) creep proceeding only if the back stress is reduced to the applied stress level by diffusion-controlled recovery, and 3) stress reductions, regardless of magnitude, always followed by a period of zero creep rate (see Figure 8a).

The thermally-activated creep, jerky glide, case is characterized by localized obstacles to dislocation movement and, consequently, no negative creep rate after the stress reduction. However, there may be a period of zero creep or positive creep, depending on the magnitude of the stress reduction (see Figure 8b).

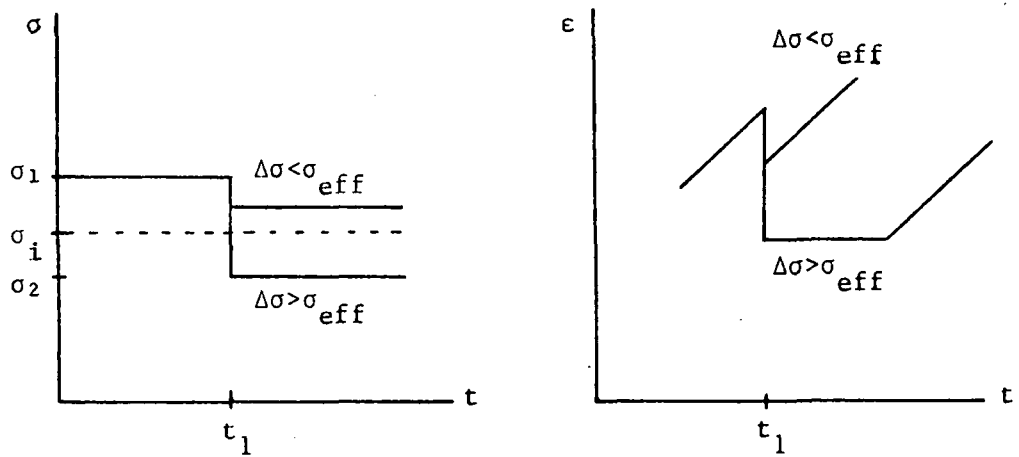
The thermally-activated creep, viscous glide, case is characterized by "smeared" rather than localized obstacles. Consequently, there may be positive, zero, or negative creep after the stress reduction (see Figure 8c).

Finally, the thermally-activated creep case with a combination of jerky and viscous glide is characterized by a combination of localized and smeared obstacles. The response of this case is similar to that of the previous two and depends on the magnitude of the stress reduction as well as the applied stress level (see Figure 8d).

Poirier concludes that, while the concept of a back stress cannot be rejected on experimental grounds,

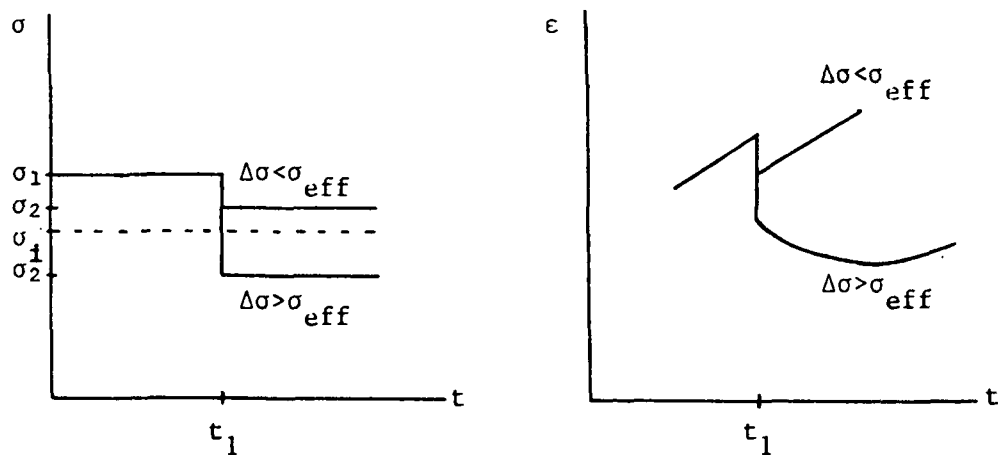


(a)

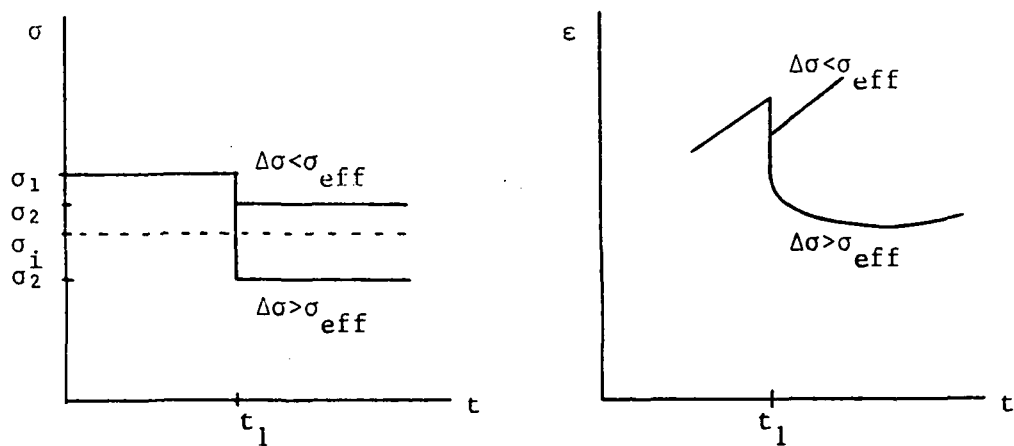


(b)

Fig. 8 Four hypotheses for creep response following a stress-drop



(c)



(d)

Fig. 8 (continued)

measurements of the back stress resulting from stress-drop tests should be performed with great care and are valid only for thermally-activated flow.

Similarly, Jones, et al. [96], conclude that due to ambiguity involved in attempting to determine a zero creep rate or merely the absence of a resolvable creep rate after unloading, the stress-drop test should be interpreted with great care on the basis of a specific deformation hypothesis. With this in mind, one can now proceed to evaluate the material constants c_1 , c_2 , c_3 , c_4 , and c_5 .

c_1 and c_2

Equation (68), which governs inelastic strain, can be rewritten as

$$\ln(\dot{\epsilon}^I) = \ln(c_1) + c_2 \ln|\zeta|, \quad (70)$$

where $|\zeta|$ is the difference between the applied stress σ and the experimentally determined back stress α , and $\dot{\epsilon}^I$ is the creep rate immediately preceding the particular stress reduction associated with that value of α . The left hand term of (70) must be linear in $\ln|\zeta|$ if it is an adequate representation of experimental data. A plot of data in the form of (70) is shown in Figure 9. Graphical means or a least-squares analysis of the data will give the values of

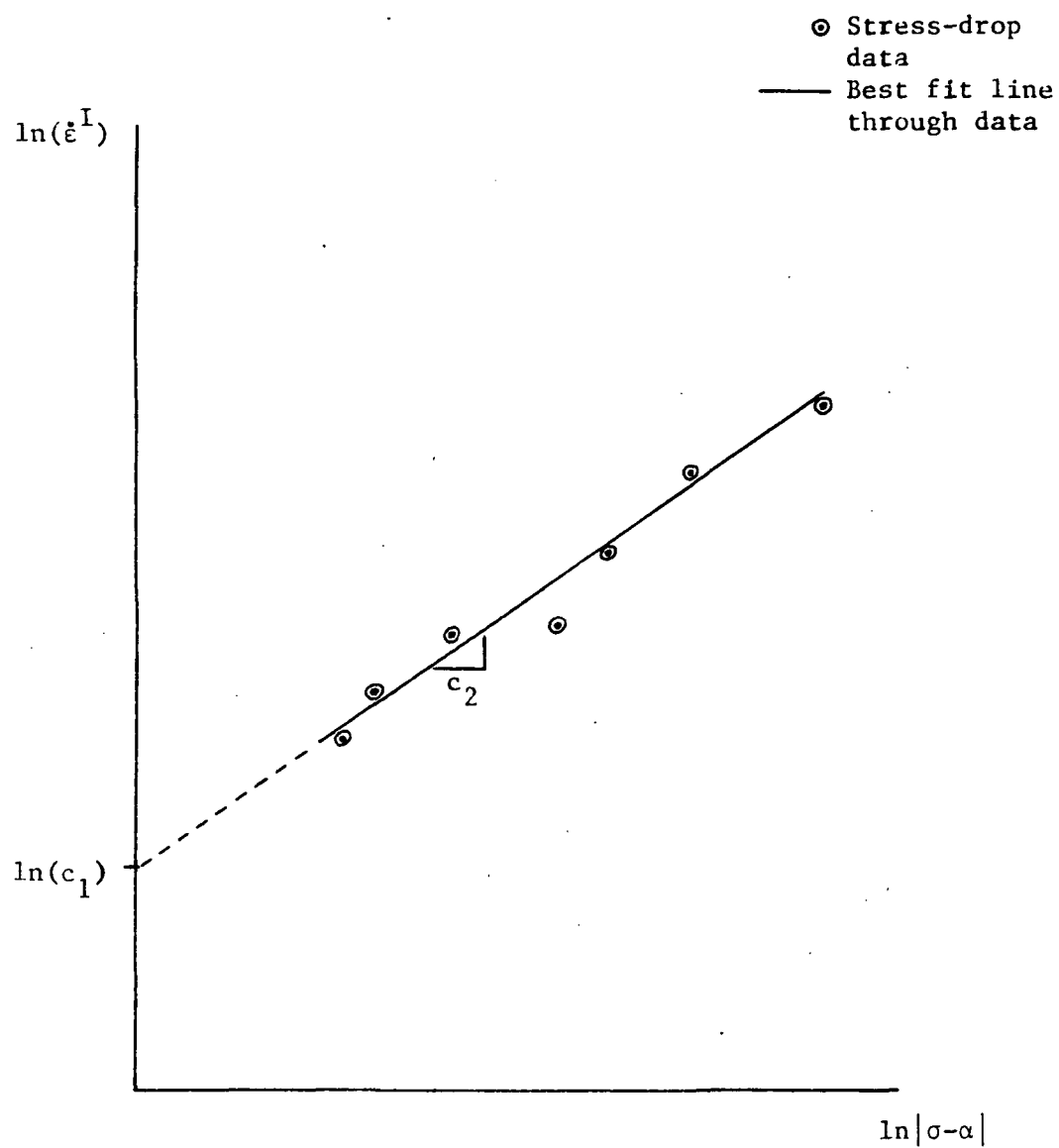


Fig. 9 A qualitative graph of $\ln(\dot{\epsilon}^I)$ v. $\ln|\sigma - \alpha|$ for determining c_1 and c_2

c_1 and c_2 .

c_5 and (c_3/c_4)

During steady-state creep, the creep rate $\dot{\epsilon}^I$ is constant and, as a consequence of equation (68), ζ must also be constant. Since the applied stress σ is constant in a creep test, this implies that the back stress α is also constant. With $\dot{\alpha} = 0$, equation (69) reduces to:

$$(c_3/c_4) = [\alpha^2/(c_1|\zeta|^{c_2})] [\exp(c_5\alpha^2) - 1], \quad (71)$$

where the fitted form $c_1|\zeta|^{c_2}$ has been used for the term $\dot{\epsilon}^I$ to reduce experimental scatter. The experimental pairs (ζ_1, α_1) and (ζ_2, α_2) , where the subscripts 1 and 2 refer to the highest and lowest values of α , may be used in equation (71) to give two nonlinear equations in two unknowns. These are then solved by iterative means to give the values of c_5 and the ratio (c_3/c_4) .

c_3 and c_4

It now remains to determine either c_3 or c_4 , since only their ratio is known at this point. In order to accomplish this, information from a point on the primary creep curve (where $\dot{\alpha}$ is not zero) must be used since the available steady-state information has been exhausted. Substituting

equation (68) into (69), separating variables, and integrating leads to

$$c_3 t = \int_0^{\alpha_1} \{c_1 | \sigma_1 - \alpha |^{c_2} - (c_4/c_3) \alpha^2 [\exp(c_5 \alpha^2) - 1]\}^{-1} d\alpha, \quad (72)$$

where σ_1 is the creep stress, α is the variable of integration, α_1 and t are the back stress and time, respectively, at which the primary creep rate $\dot{\epsilon}_1^I$ is still twice the eventual steady-state value. The value for α_1 at this data point can be determined by inverting equation (68):

$$\alpha_1 = \sigma_1 - (\dot{\epsilon}_1^I / c_1)^{1/c_2}. \quad (73)$$

Since all the quantities inside the integral now have known values, equation (72) can be integrated numerically to give a value for $c_3 t$. Since t is known, c_3 and, consequently, c_4 can be calculated easily. Although not explained by Krieg, et al., a primary-to-steady-state creep rate ratio of two appears to represent a transition point between the region of rapidly decreasing primary creep rate and the region in which the creep rate slowly approaches its steady-state value, as shown in Figure 10.

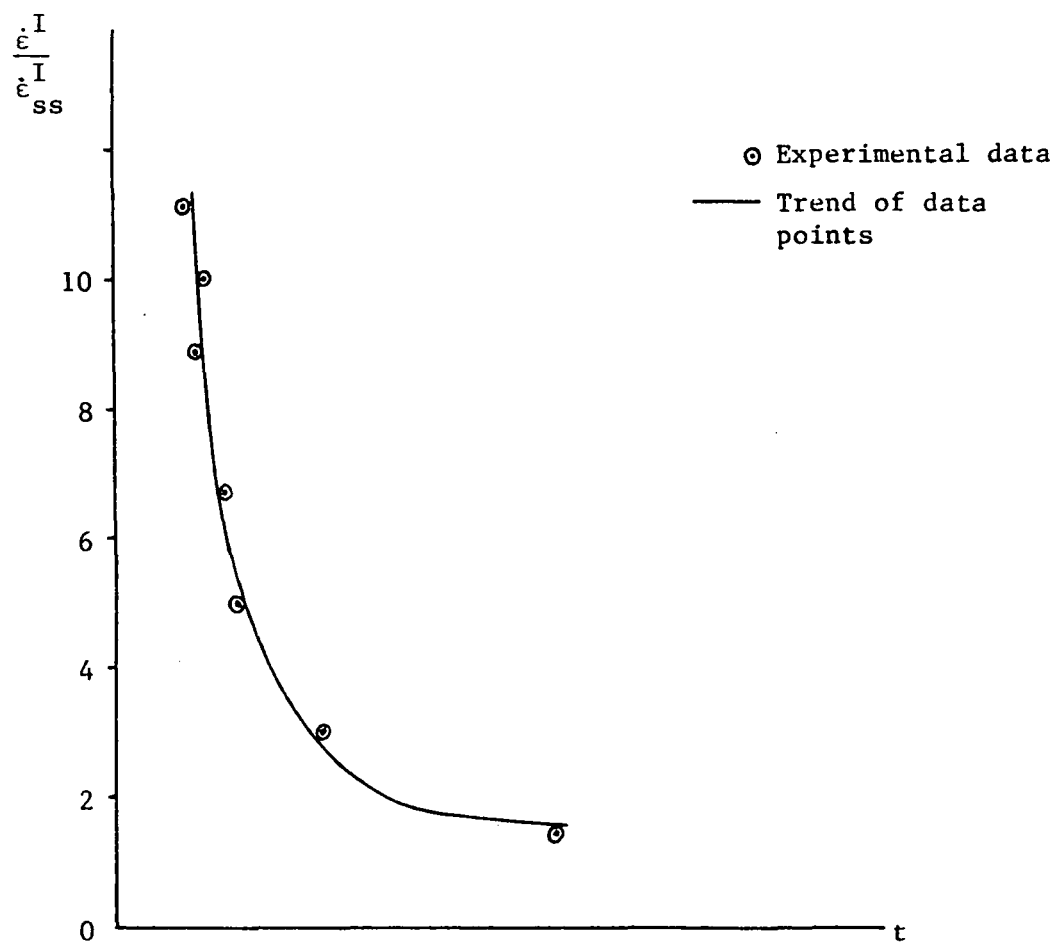


Fig. 10 A qualitative graph of the primary-to-secondary creep ratio used in determining c_3 and c_4

In summary, the Krieg, Swearengen, and Rohde theory requires a constant strain rate test (for the elastic modulus E), several stress-drop tests in the steady-state creep region (constants c_1 , c_2 , c_5 , and the ratio c_3/c_4) and a creep curve complete with primary and secondary regions (constants c_3 and c_4). This concludes the determination of the material constants for the Krieg, Swearengen, and Rohde model.

BODNER AND PARTOM'S MODEL

Chronological Development

In 1975, Bodner and Partom [50] expanded an earlier model, capable of modelling elastic-perfectly plastic behavior only [103], to include strain-hardening by introducing plastic work as the measure of the hardened state. The formulation of the inelastic strain rate equation is based on a generalization of the flow rule of classical plasticity and is motivated partly by dislocation dynamics. The inelastic strain rate is proposed as an exponential function of stress and an internal state variable representing hardness, where the hardness parameter is an exponential function of plastic work. The proposed formulation corresponds to isotropic hardening and therefore would not characterize the Bauschinger effect. Bodner and Partom found good agreement of their theory with experimental results for commercially pure aluminum.

In noting that most constitutive theories consider isotropic and directional hardening effects as completely separable and thereby controlled by different internal state variables, Bodner and his colleagues [104] extended their isotropic theory in 1979 to model uniaxial cyclic loading by proposing an alternative approach. This

approach uses separate values of the hardening parameter in order to account for the directional character of hardening during cyclic loading; one value corresponds to tensile loading, the other corresponds to compressive loading.

Bodner, et al., found good agreement with uniaxial experimental data for OFHC copper and commercially pure titanium and aluminum at room temperature in modelling phenomena such as cyclic strain hardening and softening.

The Bodner-Partom theory subsequently was generalized to a framework for the multidimensional stress case by using a general anisotropic form of the flow law [105].

In another development of the theory [106], an additional term was introduced to the constitutive equations in order to account for the thermal recovery of hardening, a term essential for modelling secondary creep. This development was used to model the superalloy Rene 95 at high temperatures.

A parameter to account for damage was introduced in 1980 [71]. Bodner examined the isotropic case first and then generalized the damage parameter to the anisotropic case in a manner similar to his earlier treatment of anisotropic hardening [105].

A preliminary method to determine the material constants of the uniaxial constitutive equations directly from experimental data rather than from trial-and-error

curve-fitting was presented in 1981 in a study of Rene 95 at high temperatures [69]. This was further developed into a detailed systematic method and applied to IN100 at elevated temperatures [107] for the case of isotropic hardening with thermal recovery and no damage.

In an earlier paper [105], anisotropy was introduced in a manner not automatically leading to plastic incompressibility. Bodner and Stouffer revised the theory in 1983 [108] to enforce plastic incompressibility in order to make the theory consistent with stability and thermodynamic principles. Results from the revised theory are essentially unchanged from the original work except that plastic volume changes become zero.

An incrementally isotropic form of the flow law has been proposed [109] in order to alleviate some of the computational difficulties encountered in using the full anisotropic form. In this formulation, the scalar hardening variable is taken to be the sum of the isotropic component and a scalar effective value of the directional component. Evolutionary equations are given for both components, including thermal recovery terms, as well as for isotropic damage. It is suggested that anisotropic damage can be treated in a manner similar to anisotropic hardening.

Recent work on the Bodner-Partom theory includes

research into modelling transient temperatures [91,94], a complete detailed review of the present constitutive theory [110], and development of a systematic method for the determination of material constants for the model in its complete anisotropic form with damage [111].

General Theory

The unified creep-plasticity model of Bodner and his colleagues [107] is motivated in part by work done in dislocation dynamics in which the total deformation can be separated into elastic and plastic components which are generally non-zero at all stages of loading. A yield criterion or loading and unloading conditions are therefore not required.

The total strain rate is given by

$$\dot{\epsilon}_{ij} = \dot{\epsilon}_{ij}^E + \dot{\epsilon}_{ij}^I, \quad (74)$$

where the elastic strain rate $\dot{\epsilon}_{ij}^E$ is given by the time derivative of Hooke's Law and the inelastic strain rate $\dot{\epsilon}_{ij}^I$ is given by the flow rule of classical plasticity:

$$\dot{\epsilon}_{ij}^I = \dot{\epsilon}_{ij}^I = \lambda \sigma'_{ij}, \quad (75)$$

where $\dot{\epsilon}_{ij}^I$ and σ'_{ij} are the deviatoric components of the

inelastic strain rate and applied stress tensors, respectively, and λ is a scalar material function.

Squaring both sides of (75) gives

$$\lambda^2 = D_2^P / J_2, \quad (76)$$

where D_2^P is the second invariant of the inelastic strain rate deviator

$$D_2^P = \frac{1}{2} \dot{e}_{ij}^I \dot{e}_{ij}^I \quad (77)$$

and J_2 is the second invariant of the stress deviator

$$J_2 = \frac{1}{2} \sigma'_{ij} \sigma'_{ij} \quad (78)$$

A fundamental assumption of the Bodner-Partom theory is that all inelastic deformations are governed by the kinetic equation

$$D_2^P = f(J_2, T, Z_k), \quad (79)$$

where T is the absolute temperature and Z_k are a set of internal state variables. Extensive work in the field of dislocation dynamics [112-114] has shown that dislocation velocity and, therefore, inelastic strain rate can be

represented as a power function or an exponential function of stress.

Bodner and Partom note that in order to represent material behavior D_2^P should vary inversely with the measure of strain hardening, have a limiting value for large J_2 , and be almost zero for low stresses. Whereas several mathematical functions may fulfill these requirements, the function chosen by Bodner and Partom is

$$D_2^P = D_0^2 \exp[-(Z^2/3J_2)^n], \quad (80)$$

where D_0 is the limiting strain rate in shear, n is a temperature dependent material constant, and Z is interpreted as an internal state variable representing hardness. It should be noted that, in subsequent developments of the theory, an internal state variable representing damage was introduced in the following manner [71,109,110]:

$$D_2^P = D_0^2 \exp\{-[Z^2(1 - \omega)^2/3J_2]^n\}, \quad (81)$$

where ω represents damage in the material.

Equations (75), (76), and (80) can then be combined to give an expression for the inelastic strain rate:

$$\dot{\epsilon}_{ij}^I = \{D_0^2 \exp[-(Z^2/3J_2)^n]/J_2\}^{1/2} \sigma'_{ij}. \quad (82)$$

The work-hardened state, that is, the resistance to plastic flow, is assumed to be represented by a single variable Z which depends on the plastic work W^P , where dW^P is $\sigma d\epsilon^I$. The plastic work rate was chosen by Bodner and Partom as the measure of hardening over the more common choice of the inelastic strain rate because Z is directly related to the stored energy of cold work and this choice leads to relative simplicity of the resulting equations [110].

It is postulated that the evolution of Z is governed by the current values of stress, hardness, and the absolute temperature:

$$\dot{Z} = F(J_2, Z, T), \quad (83)$$

where the particular form chosen by Bodner and his colleagues is

$$\dot{Z} = m (Z_1 - Z) \dot{W}^P - A Z_1 [(Z - Z_2)/Z_1]^r, \quad (84)$$

where m , Z_1 , Z_2 , A , and r are temperature-dependent material constants and the constant Z_0 is designated as the initial value of Z . The constants Z_1 and Z_2 correspond to

the maximum value of Z and the minimum recoverable value of Z , respectively.

The first term in equation (84) is the hardening term, where the negative part can be interpreted as dynamic recovery, and the second term is the thermal recovery term, designed to be negligible during rapid loading histories.

This representation, equation (84), corresponds to isotropic hardening and, as a result does not predict the Bauschinger effect. The Bodner-Partom theory was later modified [109] to include directional hardening by taking the scalar hardening variable Z in the inelastic strain rate equation (82) as the sum of the scalar isotropic hardening variable Z^I and a scalar effective directional hardening variable Z^A :

$$Z = Z^I + Z^A, \quad (85)$$

where Z^I is now given by (84) and the evolution equation for Z^A has the general form of (84) but is tensorial in character.

For the purposes of this research, the isotropic hardening model with no damage [107], equations (82) and (84), is considered.

For uniaxial stress and constant temperature, equation (82) reduces to

$$\dot{\epsilon}^I = \frac{2}{\sqrt{3}} D_0 \exp\left[-\frac{1}{2}(\sigma/Z)^{-2n}\right] \operatorname{sgn}(\sigma) \quad (86)$$

and equation (84) remains unchanged due to its scalar nature:

$$\dot{Z} = m (Z_1 - Z) \dot{W}^P - A Z_1 [(Z - Z_2)/Z_1]^r. \quad (84)$$

The material constants to be determined are D_0 , n , m , Z_1 , A , Z_2 , r , and Z_0 , the initial value of Z .

Evaluation of Material Parameters

D_0

The quantity D_0 is the maximum value of strain rate in shear and has its physical basis in the upper bound of the dislocation velocity. The value of D_0 can be set as 10^8 sec^{-1} for $\dot{\epsilon}^I > 10^3$, 10^6 sec^{-1} for $10^1 < \dot{\epsilon}^I < 10^3$, and 10^4 sec^{-1} for $\dot{\epsilon}^I < 10^1$.

Z_1 and n

The first step in the evaluation of material constants is to determine the strain rate sensitivity parameter n and the maximum value of the hardness, Z_1 , from tensile data. For material behavior as shown by curve (a) in Figure 11 where the stress saturates to a maximum value, in the region where both the stress and strain rate are constant Z

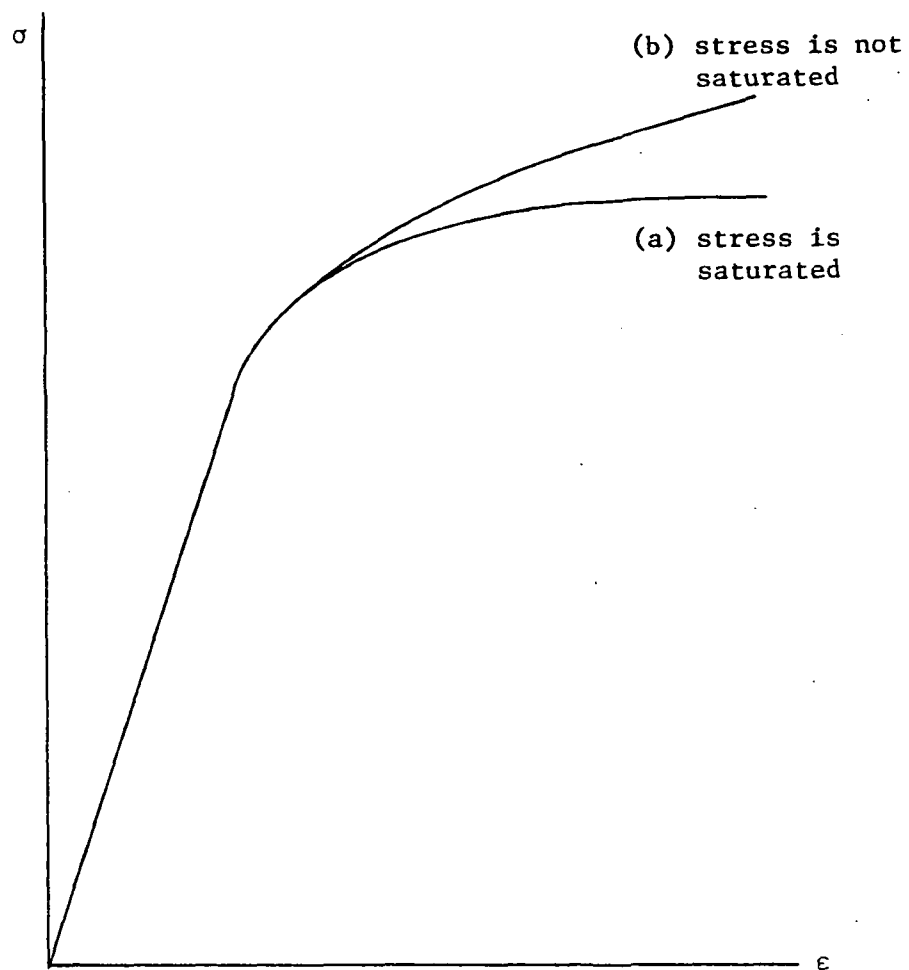


Fig. 11 A qualitative comparison of a saturated stress curve and a non-saturated stress curve

must also be constant in order to satisfy equation (86). For short duration tests with no recovery, the material must be in a fully work-hardened state to obtain the maximum value of stress; that is, Z must have its maximum value Z_1 . Rewriting equation (86) for this steady flow condition gives

$$\ln\left[-\ln\left(\frac{\sqrt{3} \cdot I}{2\dot{\epsilon}}/D_0\right)\right] = -2n\ln(\sigma) + [2n\ln(Z_1) + \ln(\frac{1}{2})]. \quad (87)$$

The left hand term of (87) must be linear in $\ln(\sigma)$ if it is an adequate representation of experimental data. A plot of data in the form of equation (87) is shown in Figure 12. Graphical means or a least-squares analysis of the data will give the values for n and Z_1 .

However, if the tensile curves are not quite saturated, as shown by curve (b) in Figure 11, simply using the largest value of stress attained may give incorrect values for Z_1 and n . In this case, equation (86) is solved for σ to give

$$\sigma = K_1 Z, \quad (88)$$

where

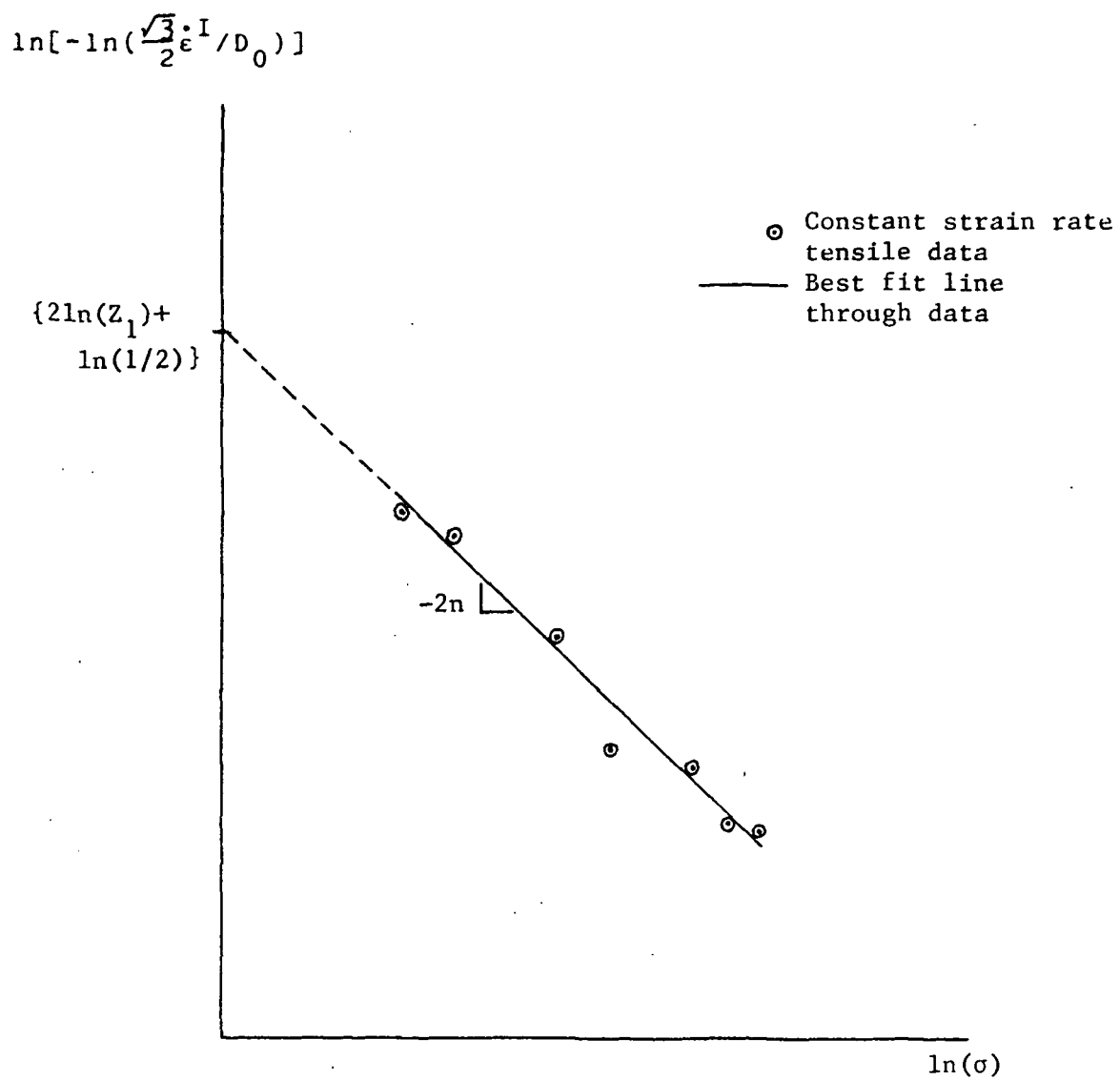


Fig. 12 A qualitative graph of constant strain rate tensile data for determining n and Z_1

$$K_1 = [21n(\frac{2}{7}D_0/\dot{\epsilon}^I)]^{-1/2n}. \quad (89)$$

In the absence of hardening recovery, the hardening evolution equation (84) becomes the first order linear differential equation

$$dZ = m (Z_1 - Z) dW^P, \quad (90)$$

which can be combined with the differential of equation (88) to give

$$d\sigma = K_1 m (Z_1 - Z) dW^P. \quad (91)$$

By defining a new parameter γ as

$$\gamma = d\sigma/dW^P \quad (92)$$

and substituting equation (88) for Z , equation (91) can be rewritten as

$$\gamma = K_1 m Z_1 - m \sigma. \quad (93)$$

In order to be an adequate representation of experimental data, γ must be linear in σ , as shown in Figure 13. The saturation stress is given by the stress level where $\gamma=0$.

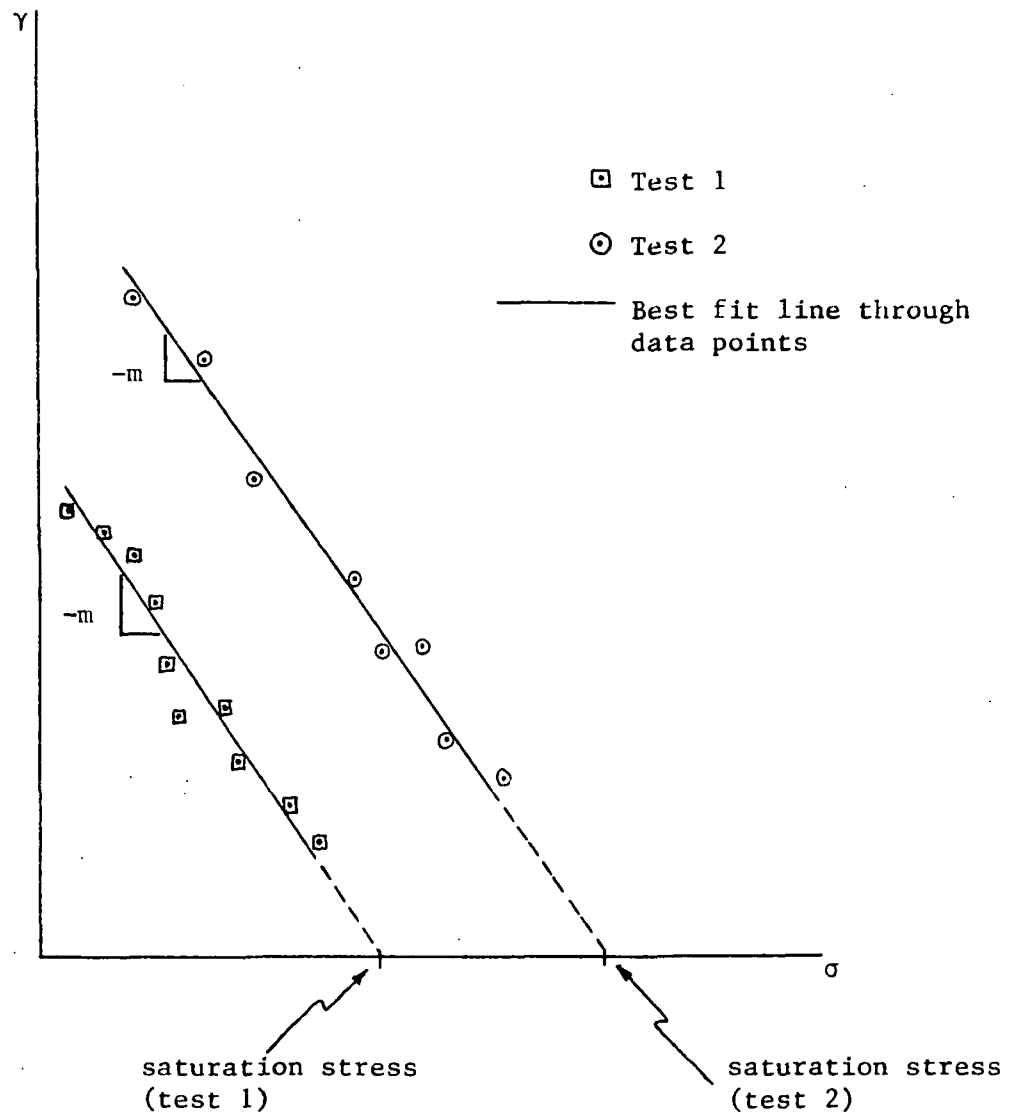


Fig. 13 A qualitative graph of γ v. σ for determining the saturated stress level

With this value of the saturation stress, one can now return to the method outlined above to determine n and Z_1 .

Z_0 and m

The value of the hardening variable Z can be calculated for corresponding values of stress and inelastic strain rate by inverting equation (86):

$$Z = \sigma [2 \ln(\frac{2}{\sqrt{3}} D_0 / \dot{\epsilon}^I)]^{1/2n}. \quad (94)$$

Equation (90), the hardening evolution equation with no recovery, can be integrated to give

$$\ln(Z_1 - Z) = \ln(Z_1 - Z_0) - mW^P, \quad (95)$$

where Z_0 is the initial value of Z . Several values of Z can be calculated for each test by using equation (94) at different stress levels and their corresponding values of $\dot{\epsilon}^I$ taken from the region in the σ - ϵ graph where recovery is minimal. In this manner a plot of $\ln(Z_1 - Z)$ against W^P can be made for several constant strain rate tensile tests. Since this plot must be linear in order to represent material behavior adequately, as shown in Figure 14, the constants m and Z_0 can be calculated easily either by graphical means or by a least-squares analysis.

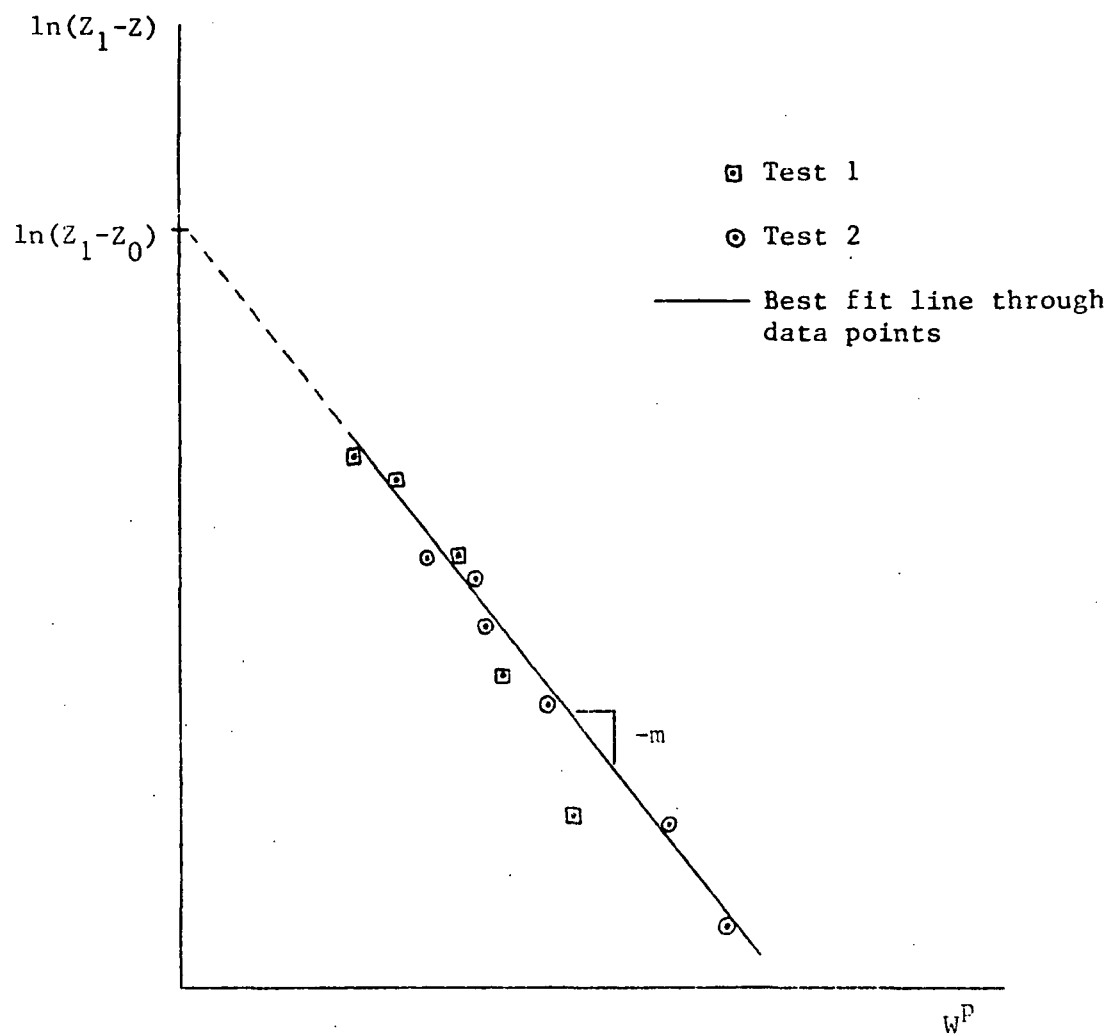


Fig. 14 A qualitative graph of $\ln(Z_1 - Z)$ v. W^P for determining m and Z_0

Alternatively, if a γ - σ graph was used in the earlier determination of n and Z_1 , then the average of the slopes of the linear curve-fits of the γ - σ data will be $-m$. Z_0 is then given by calculating values of Z in the immediate post-yield (i.e., post-elastic limit) region of a stress-strain curve.

Z_2

During secondary creep, since stress and inelastic strain rate are constant, the value of Z must also be constant in order to satisfy equation (86). These stationary values of Z can be determined from equation (94) for several creep tests. The lowest calculated stationary value of Z can be used for the value of Z_2 , the minimum value of Z , although Bodner states that $Z_2 = Z_0$ for many applications since the initial condition (Z_0) is the fully recovered state (Z_2) [110].

A and r

Since $\dot{Z} = 0$ during secondary creep, the hardening evolution equation becomes

$$m(Z_1 - Z) \dot{W}^P = A Z_1 [(Z - Z_2)/Z_1]^r. \quad (96)$$

The values of σ , $\dot{\epsilon}^I$, and Z used in the determination of Z_2

above may be used in a plot of $\ln[m (Z_1 - Z) \dot{w}^P]$ against $\ln[(Z - Z_2)/Z_1]$. The constants A and r can be calculated from these data by assuming a linear representation, although a bilinear representation may also be possible in some cases [107].

In summary, the Bodner-Partom theory requires several constant strain rate tensile tests (constants E , n , Z_1 , m , and Z_0) and several creep tests (constants Z_2 , A , and r), where the actual number of tests is dependent on the amount of data deemed necessary for accurate evaluation of the constants. This concludes the determination of material constants for the Bodner-Partom theory.

MILLER'S MODEL

Chronological Development

Miller's model [90], introduced in 1976, is based on a combination of creep phenomenology and microstructural considerations. In stressing the need to model steady-state creep rates accurately, Miller proposes to use the Garofalo hyperbolic sine relation for steady-state creep as a basis for his constitutive equations. Representing isotropic and kinematic hardening, respectively, a drag stress variable and a back stress variable are introduced to describe non-steady-state inelastic responses. The growth laws for the back stress and the drag stress follow the standard Bailey-Orowan format of competing hardening and recovery rates. Miller's growth laws feature a constant kinematic work-hardening coefficient but a variable isotropic work-hardening coefficient. A procedure for evaluation of the material constants, based partly on trial-and-error curve-fitting, is also provided. Miller found reasonably good agreement of his theory with experimental results for type 304 stainless steel at room temperature.

This model contains both kinematic and isotropic hardening terms, an arrangement which leads, in Miller's view, to a rather complex set of equations. Miller and

Sherby [115] simplified this in 1978 by eliminating kinematic hardening and allowing only isotropic hardening to be modelled. While this representation gave fairly realistic simulations for pure aluminum, it became apparent that an additional strengthening term was needed for modelling of solute-strengthened materials. The solute strengthening term, which is not an internal state variable, was added to the drag stress in the inelastic strain rate equation.

In 1980, Miller noted that several existing unified constitutive theories, including his own, predict "over-square" hysteresis loops with respect to experimentally observed behavior [116]. To eliminate this discrepancy in Miller's model, the work-hardening coefficient in the back stress growth law, previously a constant, is made an exponential function of the back stress and the direction of the effective stress. The predicted hysteresis loops using the improved equations compare more favorably with experimental results.

Schmidt and Miller further improved the model by introducing an additional solute strengthening term [117,118]. This interactive term is multiplied by the drag stress to accompany the already present non-interactive solute strengthening term (see reference [115]) which is added to this product. The non-interactive term models the

influence of solutes on yield strength while the interactive term models the influence of solutes on strain hardening. These improvements allow the model to be used over a broader range of loadings where solute effects are significant.

Miller and his colleagues have devoted much effort to research in microstructural topics which have led to the particular formulation and features of the model: the mechanisms of solutes and their effects on the yield strength and strain hardening behavior of a wide variety of alloys [119], the physical factors governing power law creep as a basis for the form of the inelastic strain rate equation [120], and experimental cyclic torsion data for support of many assumptions and predictions of the model with respect to steady-state back stresses and cyclic strain hardening/softening [121].

Recent work includes extending the theory to multiaxial form by Miller [122], and in a different manner by Kagawa and Asada [123]. In addition, it has been reported [91] that the latest form of Miller's theory contains four internal state variables in order to model the long range and short range components of the drag stress and the back stress. This form of the model may be useful in modelling transient temperature response [91].

General Theory

In attempting to model a broad spectrum of deformation phenomena, Miller uses a combination of micromechanics and creep phenomenology to derive the constitutive equations of his model [90]. It is postulated that all inelastic deformation can be characterized adequately by

$$\dot{\epsilon}^I = f[(\sigma - R)/D], \quad (97)$$

where $\dot{\epsilon}^I$ is the inelastic strain rate, f is the inelastic strain rate function, R is the "rest stress" (or back stress), and D is the drag stress. To complete the model, it remains to determine the best possible specific function for equation (97) and the evolution equations for R and D .

In stressing the need to model steady-state creep rates accurately, Miller uses the Garofalo hyperbolic sine relation for steady-state creep as a basis for deriving the inelastic strain rate function:

$$\dot{\epsilon}_{ss}^I = B' [\sinh(A\sigma_{ss})]^n, \quad (98)$$

where the subscripts "ss" refer to the steady-state condition, B' is a temperature dependent parameter, and A and n are temperature-independent constants.

Since equation (97) must reduce to (98) for the special

case of steady-state creep, there must exist a function f_1 which causes the argument $(\sigma_{ss} - R_{ss})/D_{ss}$ to reduce to σ_{ss} , i.e.

$$f_1[(\sigma_{ss} - R_{ss})/D_{ss}] = \sigma_{ss}. \quad (99)$$

When this is true, equation (99) can be substituted for σ_{ss} in equation (98) to give $\dot{\epsilon}^I_{ss}$ as a function not only of σ_{ss} , but also of R_{ss} and D_{ss} . Since steady-state creep is only a special case, the subscripts "ss" can be dropped to give

$$\dot{\epsilon}^I = B' (\sinh\{Af_1[(\sigma - R)/D]\})^n. \quad (100)$$

By examination of warm-working data for several metals, the function f_1 is determined to be

$$f_1 = \frac{1}{A} [(\sigma - R)/D]^{1.5}. \quad (101)$$

Substituting this into equation (100) will result in the explicit equation governing the inelastic strain rate:

$$\dot{\epsilon}^I = B' (\sinh\{[(\sigma - R)/D]^{1.5}\})^n. \quad (102)$$

The entire temperature dependence of the model lies in

the constant B' , which is related to the activation energy for plastic flow. Below $0.6T_m$, where T_m is the absolute melting temperature, the activation energy decreases linearly with temperature and B' is given as

$$B' = B \exp\left\{\left[-Q/0.6kT_m\right] \left[\ln(0.6T_m/T) + 1\right]\right\}, \quad (103)$$

where B is a material constant, k is the gas constant, Q is the activation energy for plastic flow, and T is the absolute temperature. Above $0.6T_m$, the activation energy is approximately constant and B' is given as

$$B' = B \exp(-Q/kT). \quad (104)$$

In either case, the expression for B' can be abbreviated as

$$B' = B \theta', \quad (105)$$

where θ' is the desired temperature-dependent factor.

The evolution equations for R and D are given in the standard work-hardening/recovery format as

$$\dot{R} = H_1 \dot{\epsilon}^I - f_2(R, T) \quad (106)$$

and

$$\dot{D} = H_2' \dot{\epsilon}^I - f_3(D, T), \quad (107)$$

where H_1 and H_2' are constants, and f_2 and f_3 are recovery functions.

In order to determine the recovery functions f_2 and f_3 , Miller applies equations (106) and (107) to the special case of steady-state creep (where $\dot{R} = \dot{D} = 0$) and substitutes equation (98) for $\dot{\epsilon}_{ss}^I$ to obtain

$$f_2(R_{ss}, T) = H_1 \dot{\epsilon}_{ss}^I = H_1 B' [\sinh(A_0)_{ss}]^n \quad (108)$$

and

$$f_3(D_{ss}, T) = H_2' \dot{\epsilon}_{ss}^I = H_2' B' [\sinh(A_0)_{ss}]^n. \quad (109)$$

In a manner similar to the derivation of the inelastic strain rate expression, equations (97) to (100), the evolution equations become

$$\dot{R} = H_1 \dot{\epsilon}^I - H_1 B \theta' [\sinh(A_1 R)]^n \quad (110)$$

and

$$\dot{D} = H_2' \dot{\epsilon}^I - H_2' B \theta' [\sinh(A_2 D^3)]^n, \quad (111)$$

where A_1 and A_2 are material constants.

For the purposes of this research, a simplified version of this model will be used. Miller and Sherby [115] simplified the model by eliminating all kinematic hardening terms, allowing only isotropic hardening to be modelled, and incorporating a solute strengthening term:

$$\dot{\epsilon}^I = B \theta' (\sinh\{[(\sigma/E)/(D + F_{sol})^{1/2}]^{1.5}\})^n, \quad (112)$$

where the modulus-compensated stress σ/E has replaced the stress σ from the earlier equations for mathematical convenience, F_{sol} is the solute strengthening parameter, and D and F_{sol} are placed under the square-root sign to produce parabolic hardening, since parabolic hardening is a better approximation for many materials than the linear hardening of the earlier equations. The evolution equation for D becomes

$$\dot{D} = H|\dot{\epsilon}^I| - H B \theta' [\sinh(A^3 D^{1.5})]^n, \quad (113)$$

where H and A are material constants.

It should be noted that a slight modification has been introduced by this author to equation (113). In order to be able to simulate cyclic loading, the inelastic strain rate term in equation (113) has been placed in absolute

value signs. This follows the practice introduced by Miller, et al., in later works [90,116-118].

The variable F_{sol} is introduced into the equations in order to characterize the effects of solute strengthening on material behavior that are found in many solute strengthened alloys. These effects include plateaus in the yield strength versus temperature curve, local maxima and minima in the strain rate sensitivity versus temperature curve, and peaks in the apparent activation energy. By judicious selection of the functional dependence of F_{sol} upon the other variables, one can ensure that the resulting equations simulate these effects.

At low temperatures, solute atoms are so immobile that they cannot keep up with the moving dislocations and hence cannot exert any particularly strong drag force. At high temperatures, the solute atoms are so mobile that they can move easily with the dislocations and are again unable to exert a strong drag force. At intermediate temperatures, however, the average velocities of solute atoms and dislocations are approximately equal, and the two can interact strongly, producing a maximum strengthening effect. From these physical considerations, one can deduce that F_{sol} should have a low value at low temperatures, should increase with temperature and pass through a maximum, and should fall to a low value at high

temperatures.

Furthermore, experimental evidence indicates that strain rate sensitivity occurs in a fashion similar to temperature sensitivity.

The particular statistical function which satisfies the mathematical requirements is

$$F_{sol} = F_{sol,max} \exp(-\{[\log_{10}(Z) - \log_{10}(Z_{max})]/2\}^2) \\ + 1(10)^{-7} \exp(-\{[\log_{10}(Z) - 30]/10\}^2), \quad (114)$$

where Z is $|\dot{\epsilon}^I|/\theta'$, $F_{sol,max}$ and Z_{max} are constants, and the second term on the right hand side of the equation is included to ensure a non-zero value of F_{sol} for conditions when $Z \gg Z_{max}$.

Finally, the material constants to be determined are A , B , n , H , $F_{sol,max}$, and Z_{max} . In addition, T_m and Q must be determined for the temperature-dependent factor θ' .

Evaluation of Material Constants

Q and T_m

The values of the absolute melting temperature T_m and the activation energy for plastic flow for the material of interest may be determined from various sources in the

literature. With these values and by use of equation (103) or (104), the temperature-dependent factor θ' may be calculated for a given absolute temperature T .

A

In order to derive the relation between the constants A , B , and n and steady-state creep rates, one returns to the observation that, for the special case of steady-state creep, the inelastic strain rate equation (112) reduces to the Garofalo equation (see equation (98)):

$$\dot{\epsilon}_{ss}^I = B \theta' [\sinh(A\sigma_{ss}/E)]^n, \quad (115)$$

where $\dot{\epsilon}_{ss}^I$ is the steady-state creep rate and σ_{ss}/E has replaced σ_{ss} . Equation (115) may be rewritten as

$$\log_{10}(\dot{\epsilon}_{ss}^I/\theta') = \log_{10}(B) + n \log_{10}[\sinh(A\sigma_{ss}/E)]. \quad (116)$$

If this equation is an adequate representation of experimental data, then the constant A can be chosen such that $\log_{10}(\dot{\epsilon}_{ss}^I/\theta')$ is linear in $\log_{10}[\sinh(A\sigma_{ss}/E)]$, as shown in Figure 15.

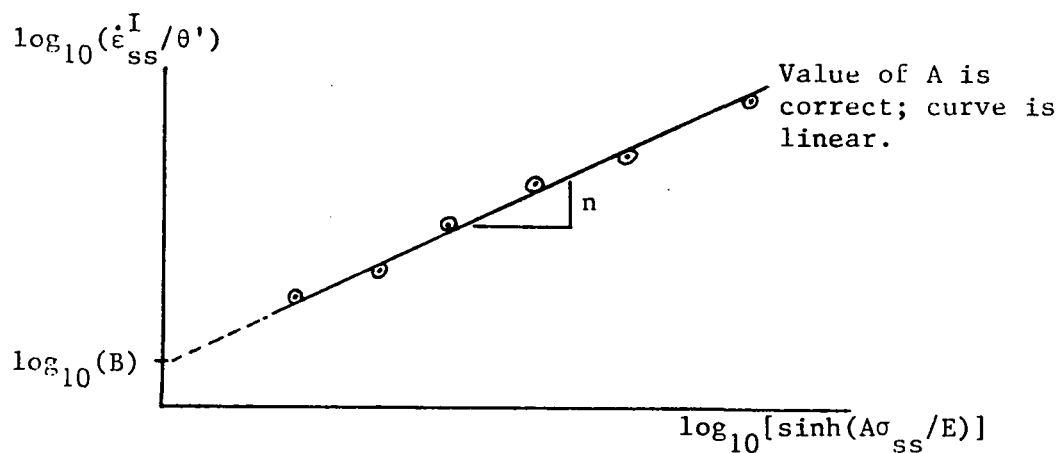
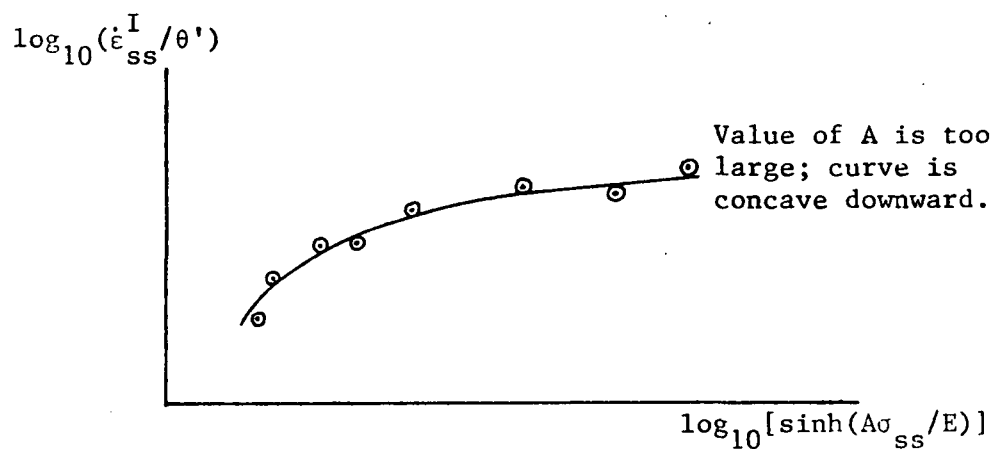
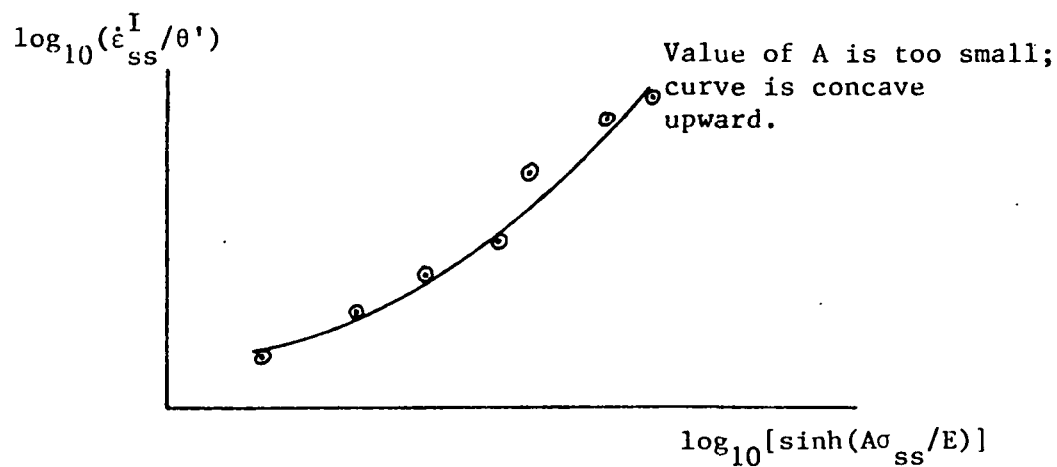


Fig. 15 The effect of A on $\log_{10}(\dot{\epsilon}_{ss}^I / \theta')$ v.
 $\log_{10}[\sinh(A\sigma_{ss}/E)]$ data

B and n

Since the value of A is now known, one can easily determine the constants B and n from equation (116), either by graphical means or by a least-squares analysis.

$F_{sol,max}$ and Z_{max}

The maximum value for F_{sol} is assigned arbitrarily and is based on an intuitive analysis of the problem of interest. Z_{max} is set by Miller as $Z_{max} = 1(10)^{10}$ for his choice of function for F_{sol} .

H

Finally, the value of the work-hardening coefficient H is determined on a trial-and-error basis by a best fit of the model through several experimental constant strain-rate stress-strain curves.

In summary, Miller's theory requires some information about the material of interest (for T_m and Q), several creep tests (constants A, B, and n), and several constant strain rate tensile tests (for e and H). This concludes the evaluation of material constants for Miller's model.

DETERMINATION OF MATERIAL CONSTANTS

Each theory is evaluated and compared to experiment by its authors for a particular material under particular temperature conditions. In general, the choice of material and conditions varies from theory to theory. One of the objectives of the current research is to create a common experimental data base for one material at one temperature in order to characterize the mathematical representations and to compare to experiment the numerical predictions of each theory.

Many of the phenomena associated with inelastic deformation such as rate sensitivity, the Bauschinger effect, and creep become significant in crystalline structures at elevated temperatures, that is, above three tenths of the absolute melting temperature. At the start of this research it was intended to perform testing on the nickel-based superalloy IN718 at 1350°F. Testing was restricted to room temperature conditions, however, since extensive difficulties were encountered with the available equipment with testing at high temperatures. This restriction led to the choice of the aluminum alloy 5086 as the candidate material. This alloy displays many of the phenomena of inelastic deformation and is already above

three tenths of its melting temperature at room temperature. Its composition and some properties are listed in Table 1.

A review of the material test requirements of each theory is shown in Table 2. It should be noted that the stress-drop tests are performed during steady-state creep and, as such, can be combined with the creep tests. The constant strain rate tensile tests were performed on an MTS 810 hydraulic material testing system; the creep tests and the stress-drop tests were performed on a constant-load creep frame which was designed and constructed at Texas A&M University. Data acquisition in both cases was by graphical means, although a digital system was also available for the creep frame. It was decided to use a constant-load creep frame rather than a constant-stress creep frame due to difficulties associated with accurately determining the applied stress when using the latter system. As can be seen by the creep response below, the effects of this choice on the results are negligible.

The results of the constant strain rate tensile tests can be seen in Figure 16 for four applied strain rates ranging from $4(10)^{-7} \text{ sec}^{-1}$ to $4(10)^{-4} \text{ sec}^{-1}$. It can be seen that the material exhibits some strain rate sensitivity and considerable work-hardening.

Table 1

Composition and Material Properties of Al 5086

Material: Al 5086 H111

Composition: 0.15%Cr, 0.40% Mn, 4.0% Mg, remainder Al

Melting temperature T_m : 858K

Elastic modulus E : $10.313(10)^3$ ksi

Ultimate stress σ_u : 40 ksi

Activation energy for plastic flow Q (at room temp.):

27,500 cal/mole

Form of specimens: uniaxial bar with $\frac{1}{2}$ -inch diameter

gauge section and threaded ends.

Table 2
Review of Material Test Requirements

Type of test	Krieg	Bodner	Miller	Total
<hr/>				
Constant strain rate				
tensile test	1	3-4	3-4	3-4
Creep	1	3-4	3-4	3-4
Stress-drop	3-4	-	-	3-4

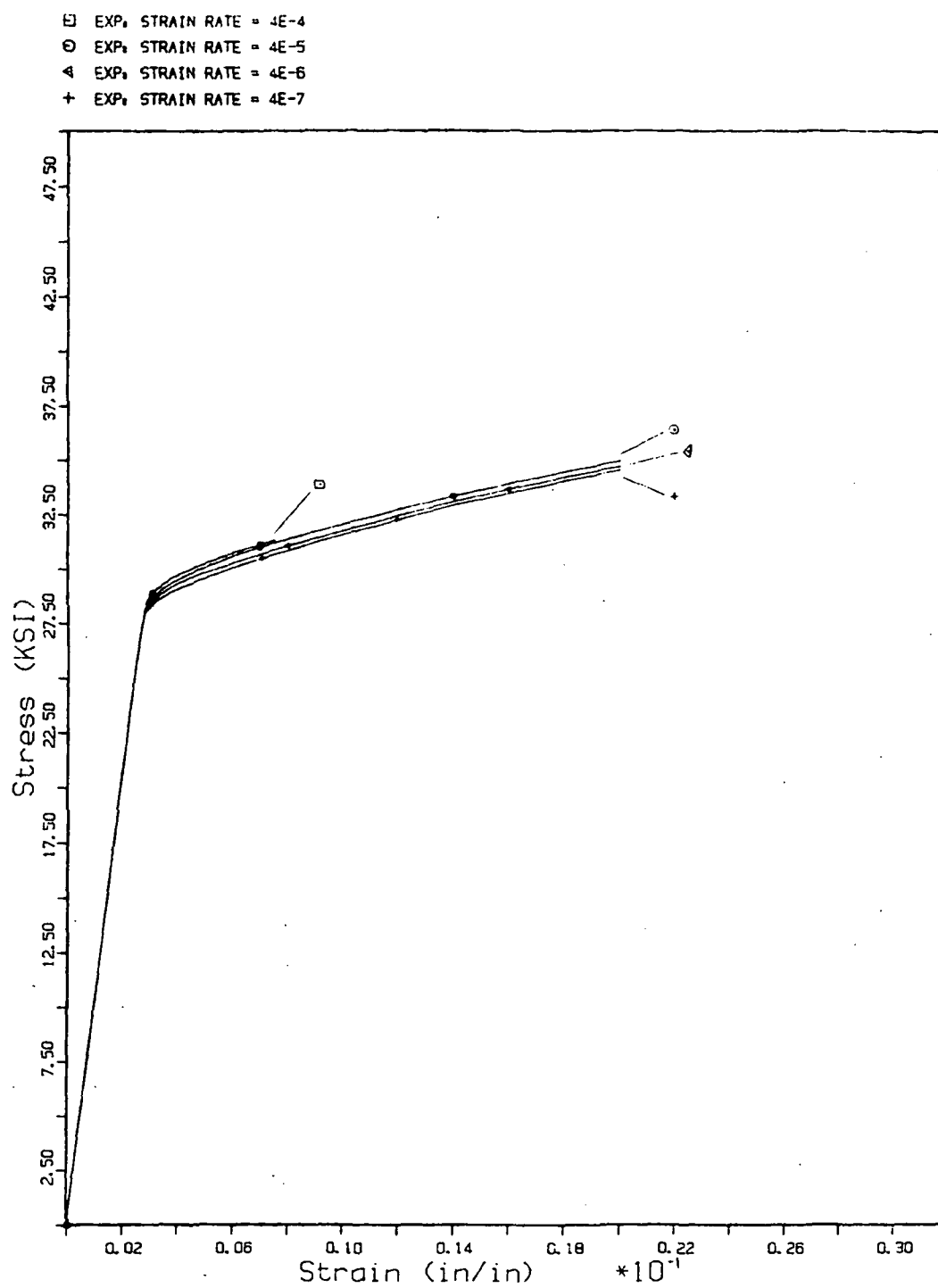


Fig. 16 Experimental constant strain rate tensile test response

The results of the constant-load creep tests can be seen in Figure 17 for five applied stresses ranging from 32.725 ksi to 38.850 ksi. Pertinent results of the constant strain rate tensile tests and the creep tests, as well as the stress-drop tests, are summarized in Table 3.

Material Constants for Krieg, et al.

In determining the material constants for this and the other theories under consideration, the procedures discussed in a previous section are followed. The reader may consult that section for greater detail.

The values of c_1 and c_2 are found by applying a linear curve-fit to a graph of $\ln(\dot{\epsilon}^I)$ v. $\ln|o - \alpha|$ data, where $\dot{\epsilon}^I$ is the strain rate immediately preceding the stress-drop, o is the applied stress, and α is the back stress. This is shown in Figure 18; the slope of the linear fit is c_2 and the vertical intercept is $\ln(c_1)$. In this manner, c_1 is calculated to be 7.177 and c_2 is $1.459(10)^{-9}$.

Under steady-state creep, the growth law for the back stress becomes (equation (71) repeated)

$$(c_3/c_4) = [\alpha^2/(c_1|\zeta|^{c_2})] [\exp(c_5\alpha^2) - 1]. \quad (71)$$

Applying this equation to two experimental cases results in

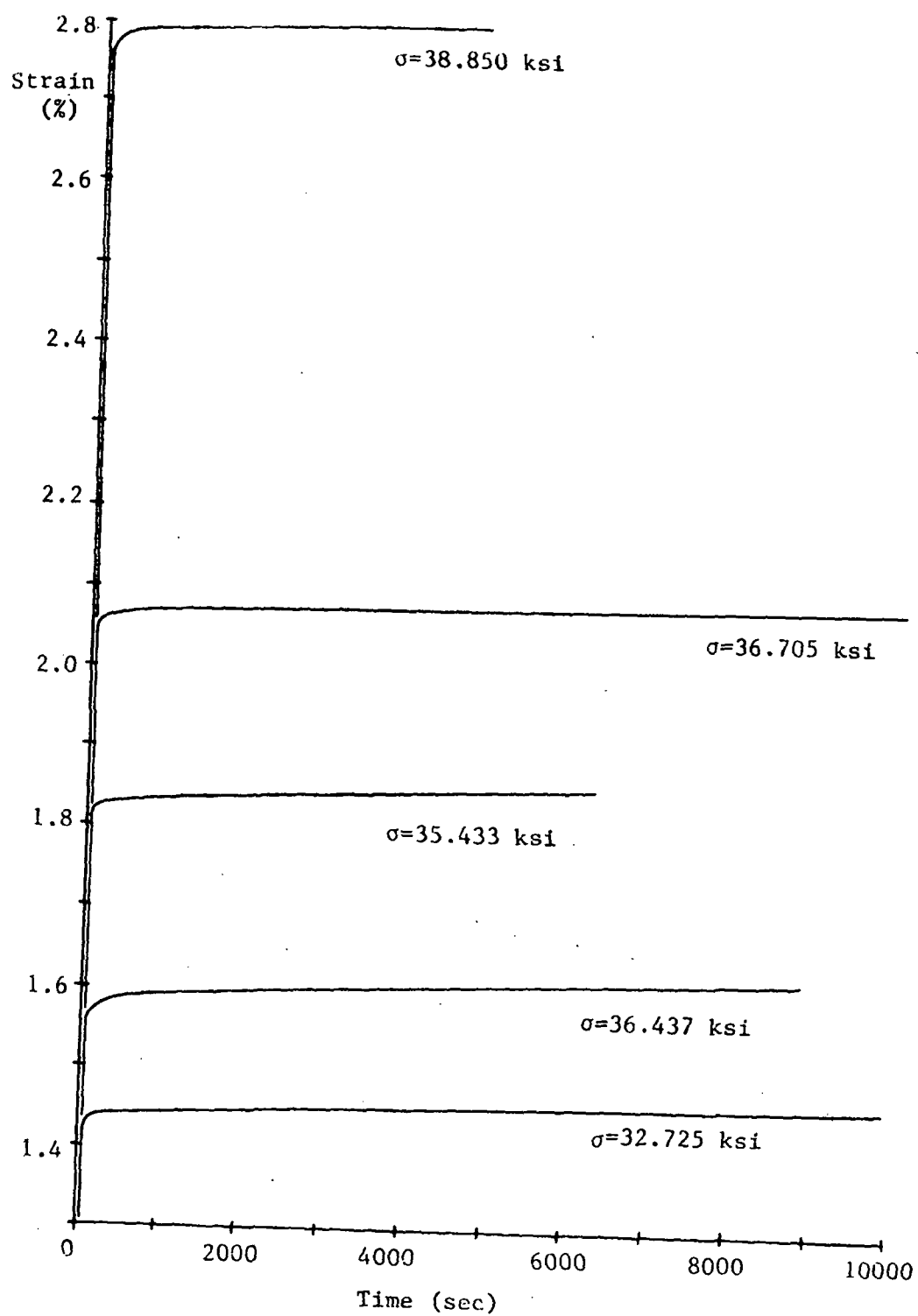


Fig. 17 Experimental Creep Test Response

Table 3
Pertinent Results of Experimental Tests

Constant strain rate tensile tests

Elastic modulus = $10.313(10)^3$ ksi

Elastic limit = 28.000 ksi

0.2% offset yield stress = 30.250 ksi for $4(10)^{-4}$ sec⁻¹

30.000 ksi $4(10)^{-5}$ sec⁻¹

29.750 ksi $4(10)^{-6}$ sec⁻¹

29.500 ksi $4(10)^{-7}$ sec⁻¹

Creep tests

Steady-state creep rate =

$1.205(10)^{-8}$ sec⁻¹ for 32.725 ksi

$4.167(10)^{-8}$ sec⁻¹ 35.433 ksi

$3.125(10)^{-8}$ sec⁻¹ 36.437 ksi

$4.435(10)^{-8}$ sec⁻¹ 36.705 ksi

$4.546(10)^{-8}$ sec⁻¹ 38.850 ksi

Stress-drop tests

Strain rate before stress drop	applied stress	back stress
$0.1000(10)^{-7}$ sec ⁻¹	34.402 ksi	33.107 ksi
$0.4243(10)^{-7}$ sec ⁻¹	35.433 ksi	33.804 ksi
$2.658(10)^{-7}$ sec ⁻¹	36.705 ksi	34.659 ksi

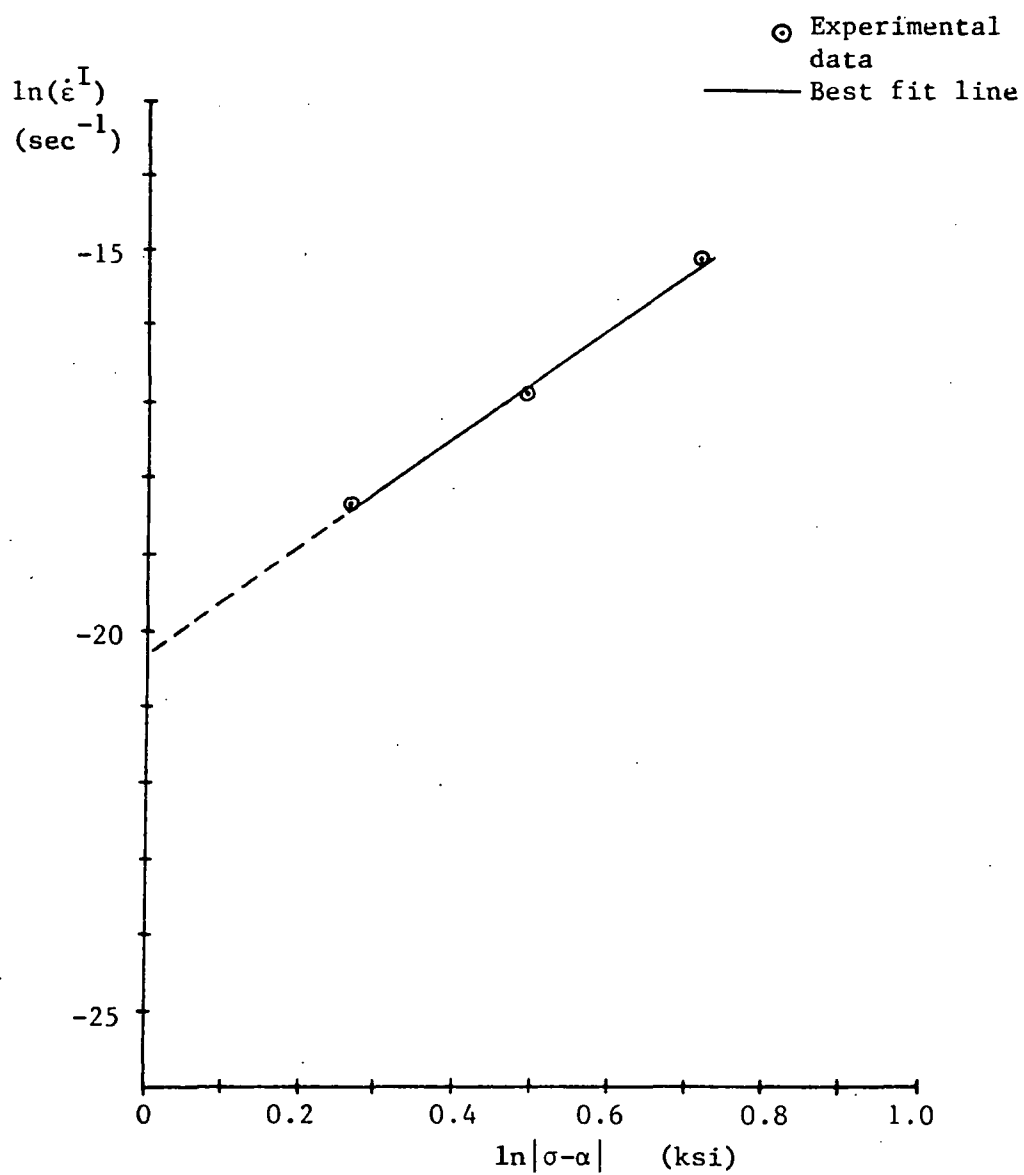


Fig. 18 Graph of $\ln(\dot{\epsilon}^I)$ v. $\ln|\sigma - \alpha|$ for Krieg's Model

two nonlinear equations in two unknowns which can be solved for (c_3/c_4) and c_5 by iteration. Solving for the cases with the highest and lowest values of α (see Table 3) yields $(c_3/c_4) = 3.255(10)^{25} \text{ ksi}^2 \text{ sec}$ and $c_5 = 0.03030 \text{ ksi}^{-2}$.

To determine c_3 , a point is chosen on the primary creep curve where the creep rate is still twice the eventual steady-state rate. The effective stress ζ at this point is calculated by inverting the inelastic strain rate equation (68) (equation (73) repeated here):

$$\zeta = (\dot{\epsilon}^I / c_1)^{1/c_2}. \quad (73)$$

The value of the back stress is then given by $\alpha = \sigma - \zeta$. Using the creep test with $\sigma = 35.433 \text{ ksi}$ gives the following information:

$$\begin{aligned} \sigma_1 &= 35.433 \text{ ksi}, \\ \dot{\epsilon}_1^I &= 8.333(10)^{-8} \text{ sec}^{-1}, \\ t_1 &= 450 \text{ sec.} \end{aligned}$$

This gives $\zeta_1 = 1.717 \text{ ksi}$ and $\alpha_1 = 33.716 \text{ ksi}$, where the subscript 1 refers to the point on the primary creep curve. The growth law for α , equation (69), can be integrated numerically by separating variables (equation (72) repeated):

$$c_3 t_1 = \int_0^{\alpha_1} \{c_1 | \sigma_1 - \alpha |^{c_2} -$$

$$(c_4/c_3) \alpha^2 [\exp(c_5 \alpha^2) - 1]]^{-1} d\alpha. \quad (72)$$

With α_1 and σ_1 known, $c_3 t$ is calculated as $2.126(10)^8$ ksi sec. From this, $c_3 = 5.185(10)^4$ ksi and $c_4 = 1.593(10)^{-21}$ ksi⁻¹ sec⁻¹.

This concludes the material parameter determination for the theory of Krieg, et al.

Material Constants for Bodner, et al.

For the present strain rate range of interest, D_0 is set as $1(10)^4$ sec⁻¹.

To determine n and Z_1 , a saturation stress must be determined analytically since the experimental stress-strain curves are not saturated (see Figure 16). This is accomplished by extrapolating to the point of zero γ on the γ v. σ graph, where $\gamma = d\sigma/dW^P$ and is given by differentiating a curve-fit of $W^P = W^P(\sigma)$. It is found that quadratics provide the best curve-fit for $W^P = W^P(\sigma)$:

$$W^P = 4.679 - 0.3679\sigma + 0.7462(10)^{-2}\sigma^2 \quad (117)$$

for $\dot{\epsilon} = 4(10)^{-7}$ sec⁻¹, and

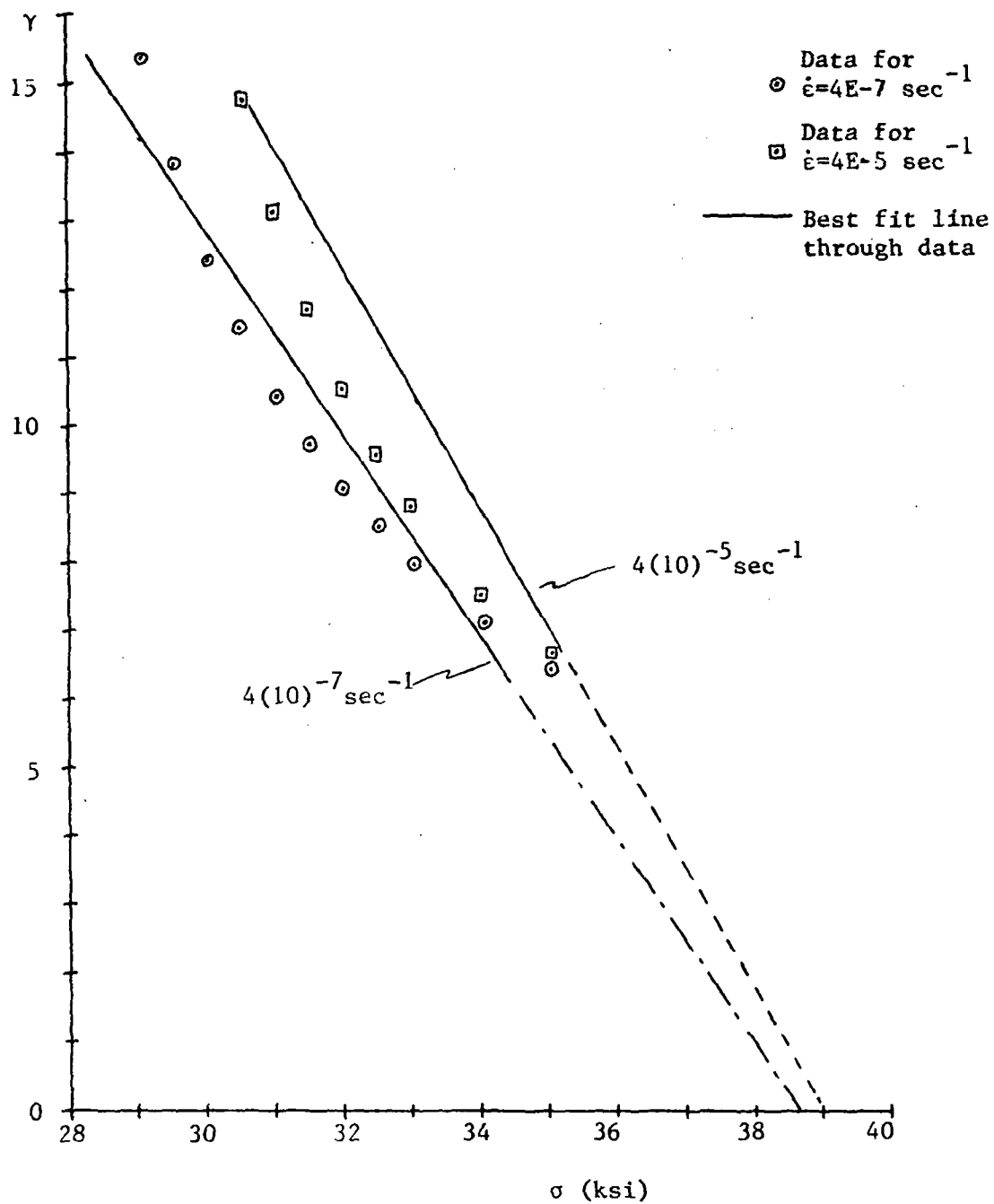


Fig. 19 Graph of Y v. σ for Bodner's Model

PRECEDING PAGE BLANK NOT FILLED

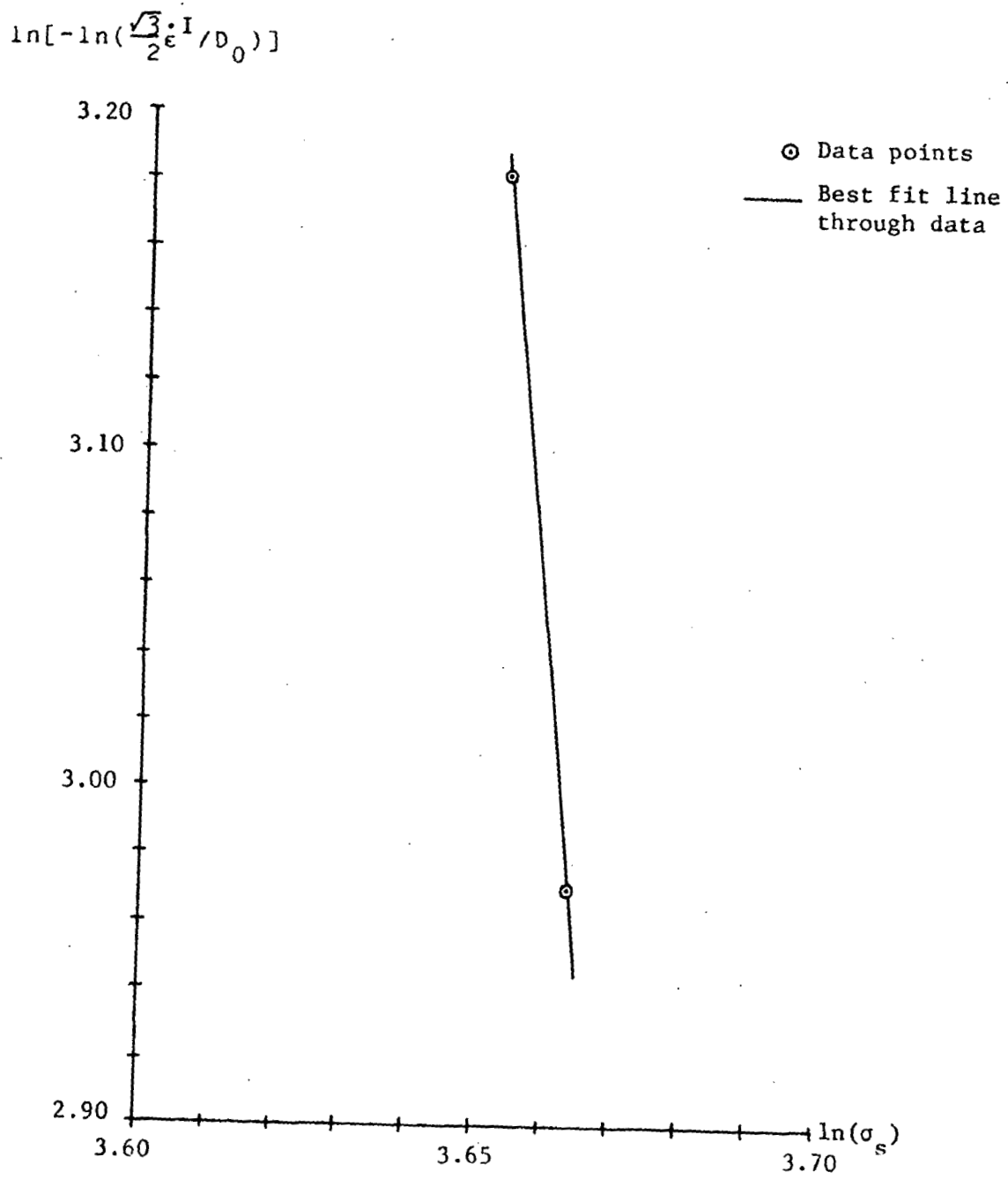


Fig. 20 Graph of $\ln[-\ln(\frac{\sqrt{3} \cdot I}{2\epsilon^1/D_0})]$ v. $\ln(\sigma_s)$ for Bodner's Model

Values of $\dot{\epsilon}^I$ are calculated from $\dot{\epsilon}^I = \dot{\epsilon} \left(1 - \frac{1}{E} \frac{\Delta \sigma}{\Delta \epsilon}\right)$

and the resulting values of Z are shown in Table 4 below.

Table 4. Calculated Values of Z used
in the Determination of Z_0

$\dot{\epsilon}$ (sec ⁻¹)	σ (ksi)	$\dot{\epsilon}^I$ (sec ⁻¹)	Z (ksi)
$4(10)^{-7}$	28.250	$3.6474(10)^{-7}$	34.102
$4(10)^{-6}$	28.375	$3.5152(10)^{-6}$	34.090
$4(10)^{-5}$	28.500	$3.3536(10)^{-5}$	34.060
$4(10)^{-4}$	28.688	$3.2243(10)^{-4}$	34.081

An average value of 34.00 ksi is taken for Z_0 .

The value of Z_2 , the minimum value of Z , is taken to be the lowest value of Z for steady-state creep, although one may simply set $Z_2 = Z_0$. The latter is chosen, giving $Z_2 = 33.50$ ksi.

The values of the recovery coefficient A and the recovery exponent r are determined by calculating a value of Z for the steady-state region of each creep test by using equation (94) (see above). Calculated values of Z are shown in Table 5 below.

Table 5. Calculated Values of Z used
in the Determination of A and r

σ_{ss} (ksi)	$\dot{\epsilon}_{ss}^I$ (sec^{-1})	Z (ksi)	$\ln[m (Z_1 - Z) \dot{W}^P]$	$\ln[(Z - Z_2)/Z_1]$
32.725	$1.205(10)^{-8}$	39.758	-2.091	-12.38
36.437	$3.125(10)^{-8}$	44.192	-1.520	-12.37
36.705	$4.435(10)^{-8}$	44.489	-1.491	-12.14

These values of Z are then used to construct a $\ln[m (Z_1 - Z) \dot{W}^P]$ v. $\ln[(Z - Z_2)/Z_1]$ graph, as shown in Figure 21. The slope of a linear curve-fit for this graph is r; the vertical intercept is $\ln(AZ_1)$. In this manner, A is calculated to be $1.447(10)^{-7} \text{sec}^{-1}$ and r is 0.2290.

This concludes the material constant determination for the theory of Bodner, et al.

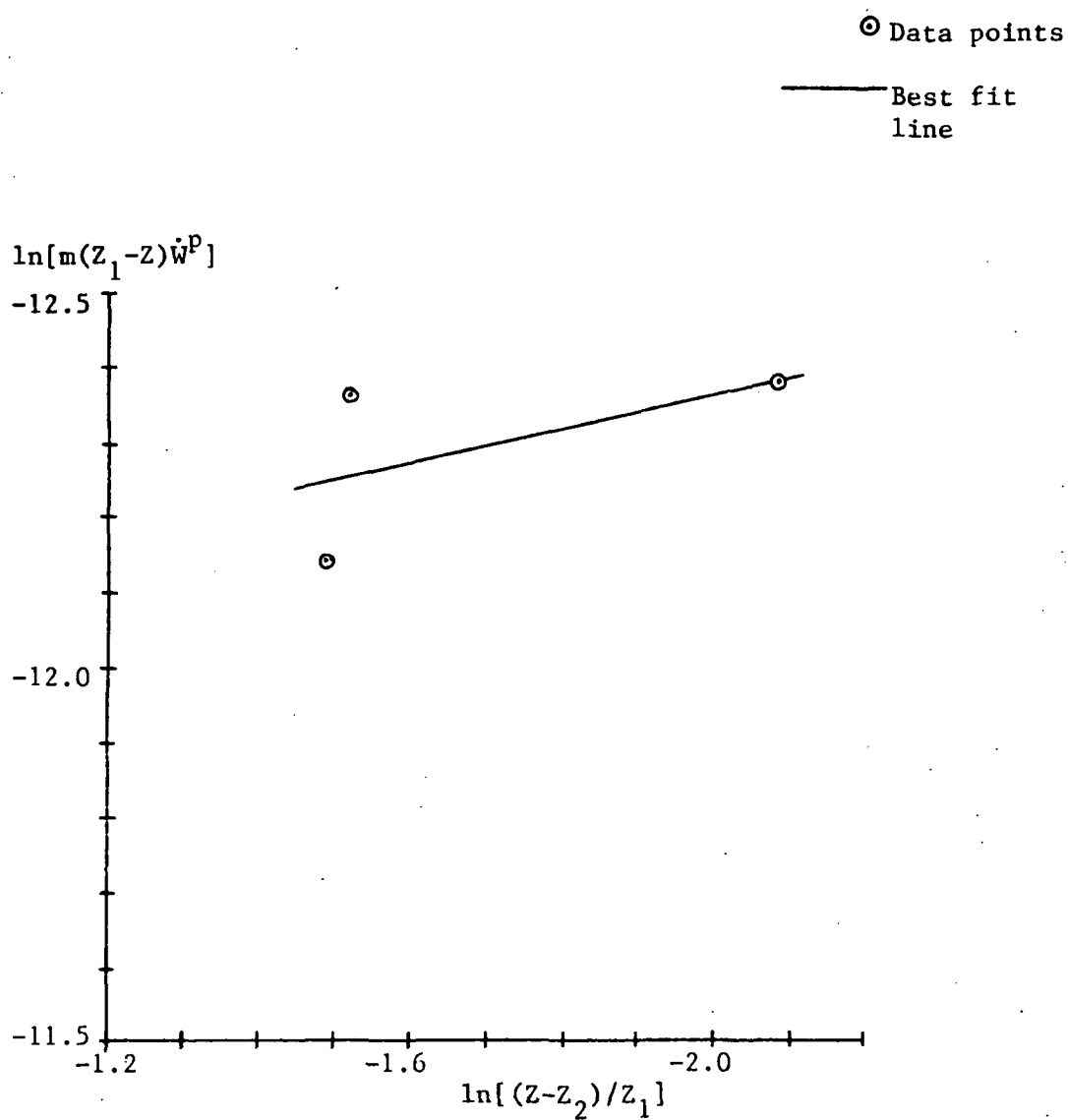


Fig. 21 Graph of $\ln[m(Z_1 - Z)\dot{W}^P]$ v. $\ln[(Z - Z_2)/Z_1]$
for Bodner's Model

Material Constants for Miller, et al.

The values of the activation energy for plastic flow Q and the melting temperature T_m can be found in a materials handbook. For Al 5086 at room temperature, Q is 27500 cal/mole and T_m is 858K.

Since room temperature is less than $0.6T_m$ for Al 5086, equation (103), repeated below, is used to calculate the temperature-dependent factor θ' :

$$\theta' = \exp\{[-Q/0.6kT_m] [\ln(0.6T_m/T) + 1]\}, \quad (103)$$

where T and T_m are absolute temperatures. This gives θ' as $8.74(10)^{-19}$.

The value of A is chosen such that a graph of $\log_{10}(\dot{\epsilon}_{ss}^I/\theta')$ v. $\log_{10}[\sinh(A\sigma_{ss}/E)]$ for steady-state creep data is linear. This is shown below in Table 6 and in graphical form Figure 22 for several values of A .

Table 6. Calculations for Various Values of A

$\dot{\epsilon}_{ss}^I$ (sec^{-1})	$\log_{10}(\dot{\epsilon}_{ss}^I/\theta')$	σ_{ss} (ksi)	$\log_{10}[\sinh(A\sigma_{ss}/E)]$		
			A=50	A=200	A=1000
$1.205(10)^{-8}$	10.14	32.725	-0.7977	-0.1687	1.076
$4.167(10)^{-8}$	10.68	35.443	-0.7628	-0.1292	1.191
$3.125(10)^{-8}$	10.55	36.437	-0.7506	-0.1153	1.233
$4.435(10)^{-8}$	10.71	36.705	-0.7474	-0.1116	1.244
$4.546(10)^{-8}$	10.72	38.850	-0.7225	-0.0826	1.335

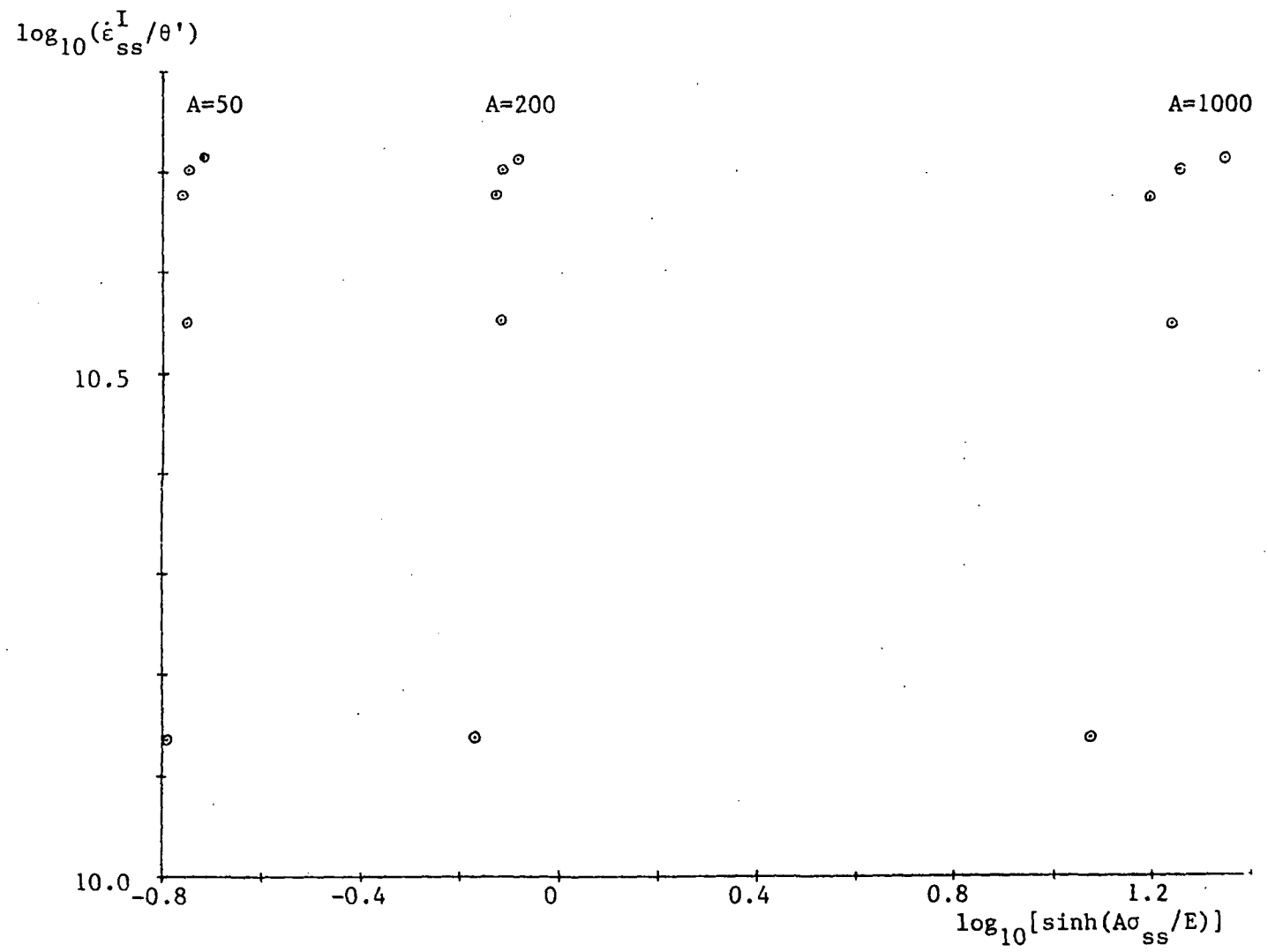
As can be seen in Figure 22, the curve is nearly linear for $A = 50$, with no significant improvement for $A < 50$.

With this value of A, the values of B and n can be determined by constructing a linear curve-fit for the data in Figure 22. The slope of the curve-fit is n; the vertical intercept is $\log_{10}(B)$. In this manner, n is calculated to be 7.701 and B is $2.410(10)^{16} \text{ sec}^{-1}$.

The maximum value of F_{sol} is set arbitrarily as $F_{sol,max} = 1(10)^{-7}$. Simulations of experimental tests have shown that the choice of this value does not influence the results significantly.

The work-hardening coefficient H is set arbitrarily to give the best fit of simulations of constant strain rate tensile tests to experimental data. This value is set as $7.5(10)^{-4} \text{ ksi}$.

Fig. 22 Graph of $\log_{10}(\dot{\epsilon}_{ss}^I/\theta')$ v. $\log_{10}[\sinh(A\sigma_{ss}/E)]$
for Miller's Model



Finally, the initial value of the drag stress, D_{init} , is calculated by inverting the inelastic strain rate equation (112) and using values of $\dot{\epsilon}^I$ and σ at yield. In this manner, D_{init} is calculated to be $3.386(10)^{-5}$.

This concludes the material constant determination for the theory of Miller, et al.

A summary of the material constants for each theory is given in Table 7.

Table 7. Summary of Material Constants for all Models

Krieg, <u>et al.</u>	$E = 10.313(10)^3 \text{ ksi}$
	$c_1 = 7.177$
	$c_2 = 1.459(10)^{-9}$
	$c_3 = 5.185(10)^4 \text{ ksi}$
	$c_4 = 1.593(10)^{-21} \text{ ksi}^{-1} \text{ sec}^{-1}$
	$c_5 = 0.03030 \text{ ksi}^{-2}$
Bodner, <u>et al.</u>	$E = 10.313(10)^3 \text{ ksi}$
	$n = 10.30$
	$Z_1 = 46.59 \text{ ksi}$
	$m = 1.558 \text{ ksi}^{-1}$
	$Z_0 = 34.00 \text{ ksi}$
	$Z_2 = 33.50 \text{ ksi}$
	$A = 1.447(10)^{-7} \text{ sec}^{-1}$
	$r = 0.2290$
Miller, <u>et al.</u>	$E = 10.313(10)^3 \text{ ksi}$
	$\theta' = 8.74(10)^{-19}$
	$A = 50$
	$n = 7.701$
	$B = 2.410(10)^{16} \text{ sec}^{-1}$
	$F_{\text{sol,max}} = 1(10)^{-7}$
	$H = 7.5(10)^{-4} \text{ ksi}$
	$D_{\text{init}} = 3.386(10)^{-5}$

COMPARISON OF THEORY TO EXPERIMENT

The third and final objective of this research is to compare the numerical predictions of each theory to experiment by integrating the constitutive equations subject to specific load histories. Before proceeding to the quantitative comparisons, however, there follows a brief qualitative review of the predictive capabilities of each theory.

Qualitative Review of Predictive Capabilities

All the theories under consideration are similar in that they are unified theories; that is, the rate-dependent creep and the rate-independent plasticity components have been combined into one inelastic strain term. Each theory, in the form under consideration, is isothermal in that it is not able to model transient temperature response. Furthermore, each model is able to exhibit strain rate sensitivity through the exponent in the inelastic strain rate equation.

The theory of Krieg, et al., contains two internal state variables: the inelastic strain and the back stress. The back stress represents kinematic hardening, which allows the Bauschinger effect to be modelled. Krieg,

et al., have assumed the hardening function in the back stress growth law to be constant, which may cause "over-square" hysteresis loops. This may be alleviated by introducing a dependence of the hardening function on the current value of the stress or back stress. Due to the lack of a representation for isotropic hardening (the drag stress), this theory may not be able to model cyclic strain hardening. Finally, it can be seen that anelasticity (strain recovery at zero load) can be predicted by this theory by setting $\sigma = 0$ in the inelastic strain rate equation (68); relaxation is predicted by setting $\dot{\epsilon} = 0$; and creep is predicted by setting $\dot{\sigma} = 0$.

The theory of Bodner, et al., also contains two internal state variables: the inelastic strain and a term representing isotropic hardening. The isotropic hardening growth law contains dynamic as well as thermal recovery. The presence of isotropic hardening allows cyclic strain hardening to be modelled, although the absence of kinematic hardening may preclude the ability to model the Bauschinger effect. Finally, it can be seen that anelasticity cannot be modelled since $\dot{\epsilon}^I$ is zero when setting $\sigma = 0$ in the inelastic strain rate equation (86); creep and relaxation can be predicted, however, by setting $\dot{\sigma} = 0$ and $\dot{\epsilon} = 0$, respectively.

The theory of Miller, et al., contains two internal

state variables: the inelastic strain and the drag stress. The drag stress represents isotropic hardening, which allows cyclic strain hardening to be modelled. This model is similar to that of Krieg, et al., in that the hardening function in the drag stress growth law is assumed to be constant, which produces "over-square" hysteresis loops. The model is similar to that of Bodner, et al., in that the lack of a back stress may preclude the ability to model the Bauschinger effect as well as anelasticity. Finally, creep and relaxation are modelled in a manner similar to that of the other two theories.

Review of Integration Technique

Each theory is represented mathematically by a set of differential equations. Since these differential equations are numerically "stiff", causing higher-order integration schemes to become unstable [124], a first-order forward integration scheme with small, variable time steps was used. For example, Krieg's inelastic strain rate equation ((68) repeated here)

$$\dot{\epsilon} = c_1 |\sigma - \alpha|^{c_2} \text{sgn}(\sigma - \alpha) \quad (68)$$

becomes

$$\epsilon^I(t + \Delta t) = c_1 |\sigma(t) - \alpha(t)|^{c_2} \Delta t + \epsilon^I(t) \quad (119)$$

where t represents an initial state and $t + \Delta t$ represents the incremented state. Similarly, the growth law for the back stress (equation (69)) becomes

$$\alpha(t + \Delta t) = \{c_3 [(\epsilon^I(t + \Delta t) - \epsilon^I(t))/\Delta t] -$$

$$c_4 \alpha^2(t) [\exp(c_5 \alpha^2(t)) - 1] \operatorname{sgn}(\alpha(t))\} \Delta t + \alpha(t). \quad (120)$$

Finally, the stress is updated by

$$\sigma(t + \Delta t) = E \{ \dot{\epsilon} - [(\epsilon^I(t + \Delta t) - \epsilon^I(t))/\Delta t] \} \Delta t + \sigma(t). \quad (121)$$

This concludes the review of the integration technique used in this research.

Comparison of Numerical Predictions to Experiment

In this section, the ability of each model to predict the response to a specific load history is analyzed. The first experimental test to be modelled is a constant strain rate tensile test with $\dot{\epsilon} = 4(10)^{-5} \text{ sec}^{-1}$, shown in Figure 23.

EXP. STRAIN RATE = $4E-5$

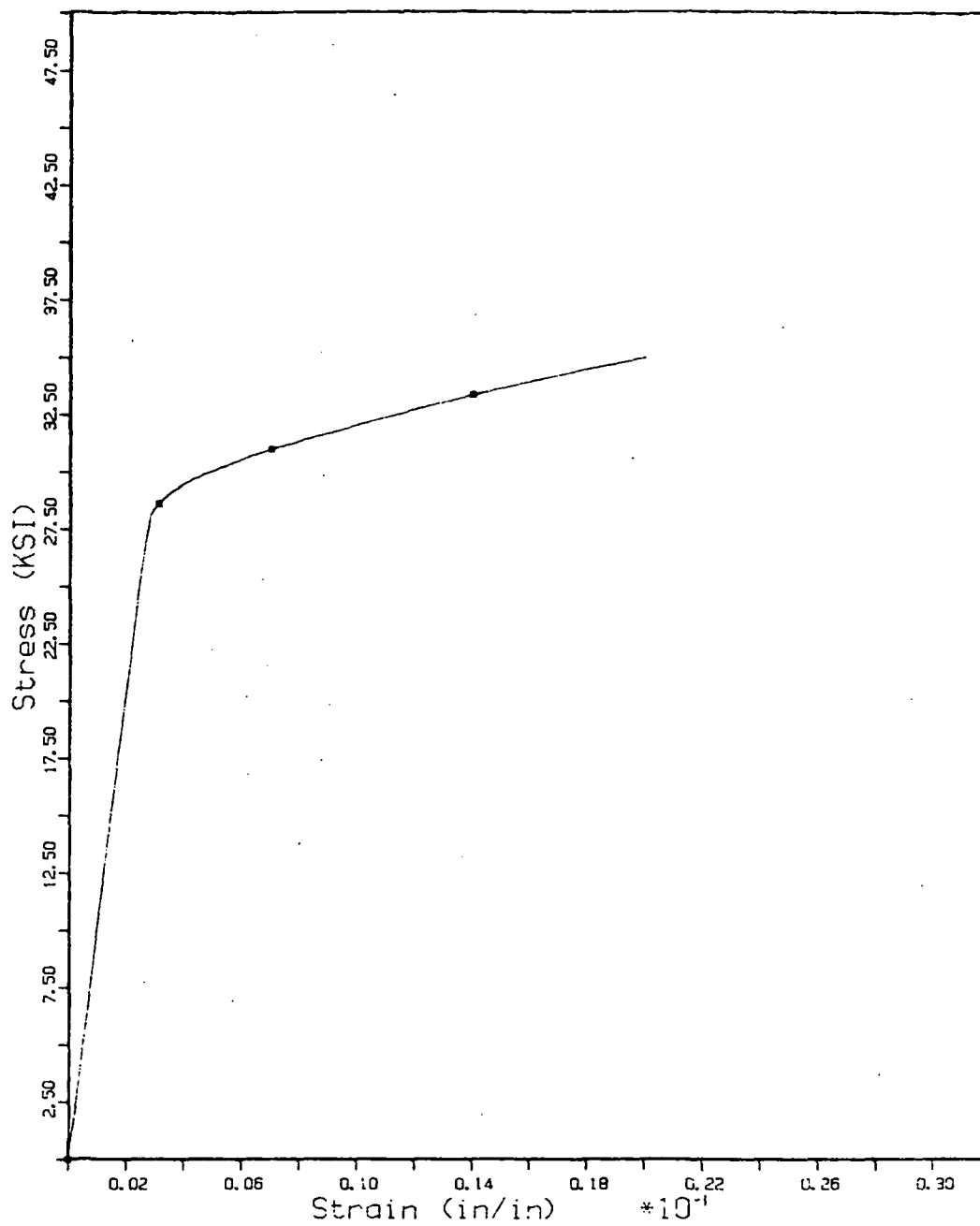


Fig. 23 Experimental constant strain rate tensile test:

$$\dot{\epsilon} = 4(10)^{-5} \text{ sec}^{-1}$$

Krieg, et al.: Constant Strain Rate Tensile Test

It can be seen from Figure 24 that this theory does not compare favorably with experiment for this constant strain rate tensile test. It is believed by this author that this is due largely to the method of determining the material constants. As discussed in an earlier section, the ability to determine a zero creep rate or merely the absence of a resolvable creep rate in a stress-drop test depends greatly on the resolution of the data acquisition equipment and is extremely difficult and time consuming at best. A parameter variation study showed slight improvements in the stress-strain curve in Figure 24 but led to computational difficulties in simulating cyclic load histories and complex load histories. It can be concluded from this that improvements in the measurement of back stresses are required. For example, the methods of Blum and Finkel [98], in which the instantaneous strain change and the maximum strain change after unloading are compared, and of Walker [58], in which one applies hold times on the unloading side of a saturated hysteresis loop and extrapolates to the point of zero relaxation, merit further study.

Bodner, et al.: Constant Strain Rate Tensile Test

The theory of Bodner, et al., compares favorably to

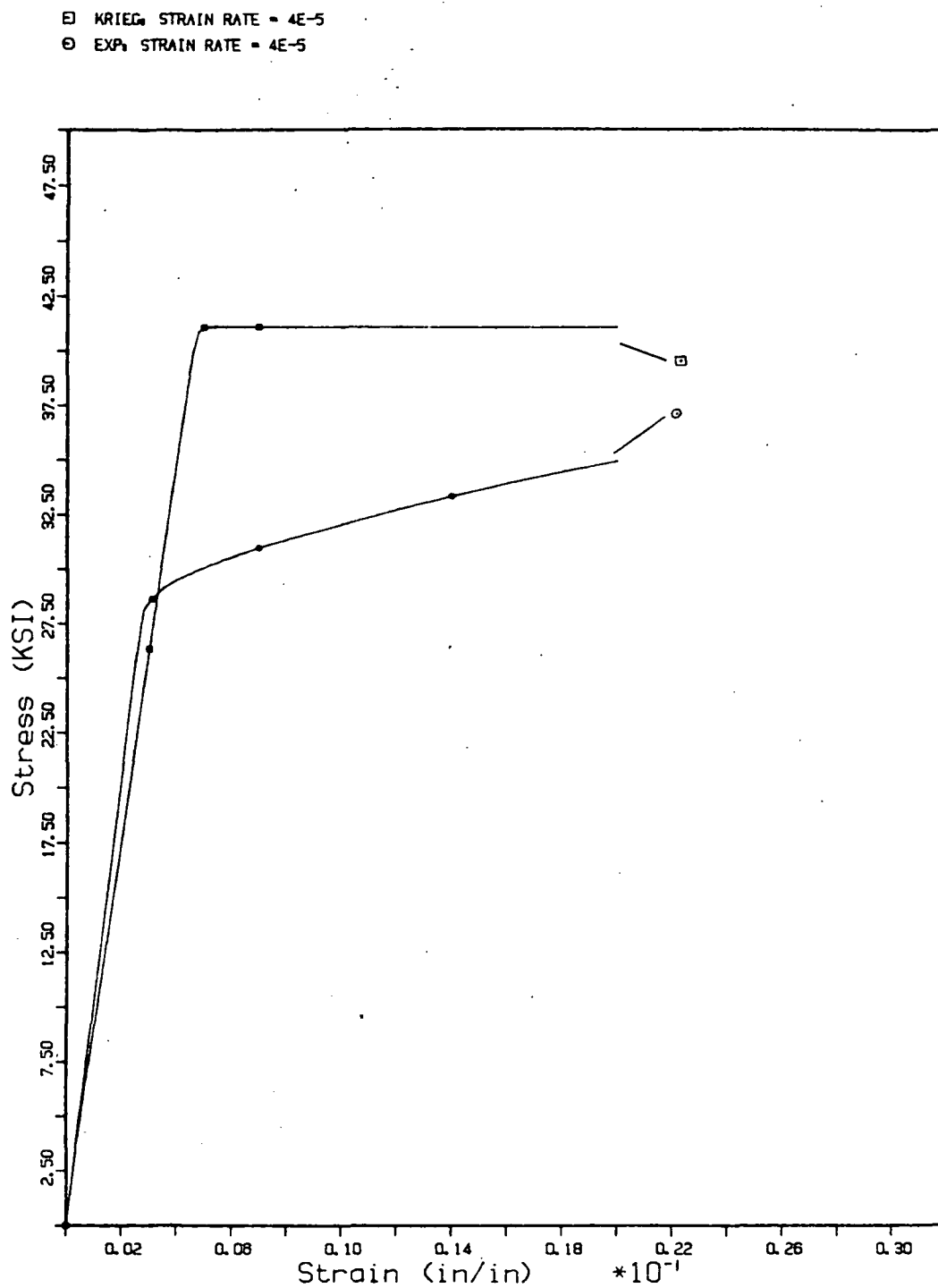


Fig. 24 Constant strain rate tensile test. Comparison of theory of Krieg, et al., to experiment.

C-4

experiment, as can be seen in Figure 25. Work-hardening is predicted well although the elastic-inelastic behavior transition is too sharp. It is found that this is due to the theory predicting values of Z that are too high at low stresses, possibly requiring a modification of the hardening term in the growth law for Z .

Miller, et al.: Constant Strain Rate Tensile Test

In determining the material constants for this theory, the strain rate exponent n was calculated to be 7.7, resulting in the response shown in Figure 26. A parameter variation study indicated that a value of $n = 6$ appeared to fit the experimental data much better. This indicates a problem inherent in many constitutive theories: the determination of material constants is not rigorous and the difficulties are compounded by the fact that many constants are interdependent and, in fact, may be assigned arbitrary values. In the interests of further numerical comparisons, a value of $n = 6$ is chosen for this model. With this choice, this theory predicts the yield point and work-hardening fairly well.

Finally, a comparison of all the models for a constant strain rate tensile test can be seen in Figure 27.

- EXP, STRAIN RATE = $4E-5$
○ BOONER, STRAIN RATE = $4E-5$

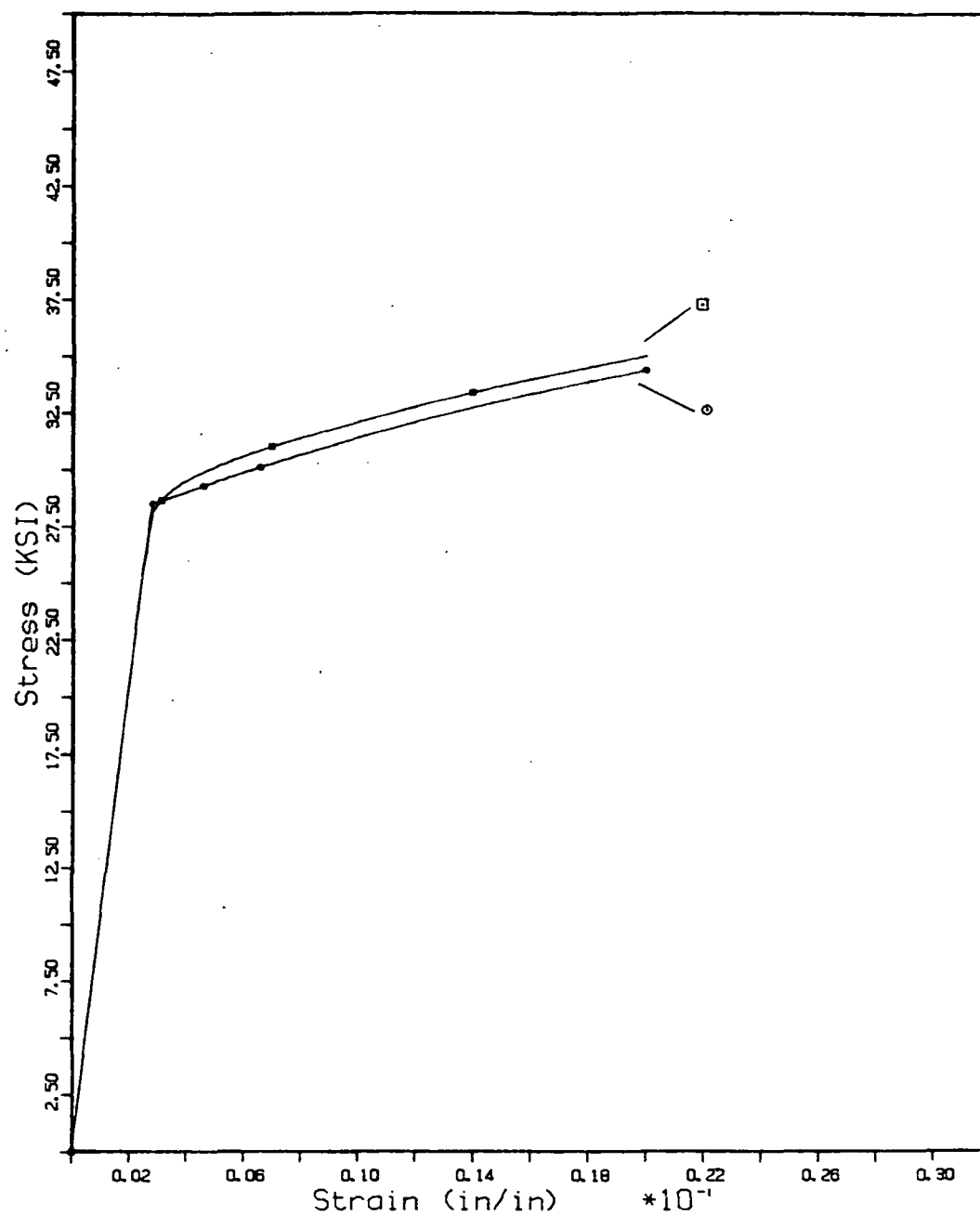


Fig. 25 Constant strain rate tensile test. Comparison of theory of Bodner, et al., to experiment.

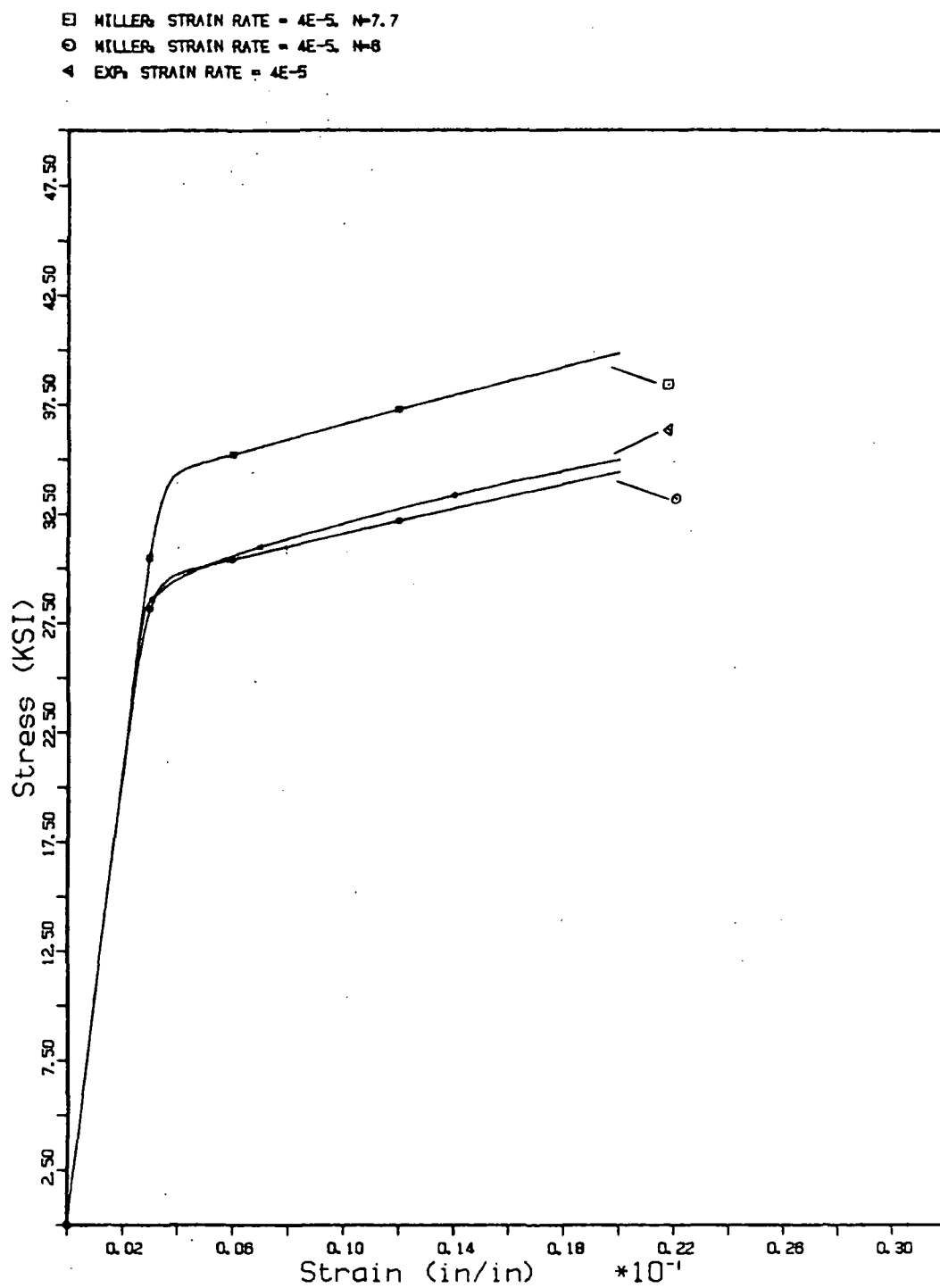


Fig. 26 Constant strain rate tensile test. Comparison of theory of Miller, et al., to experiment.

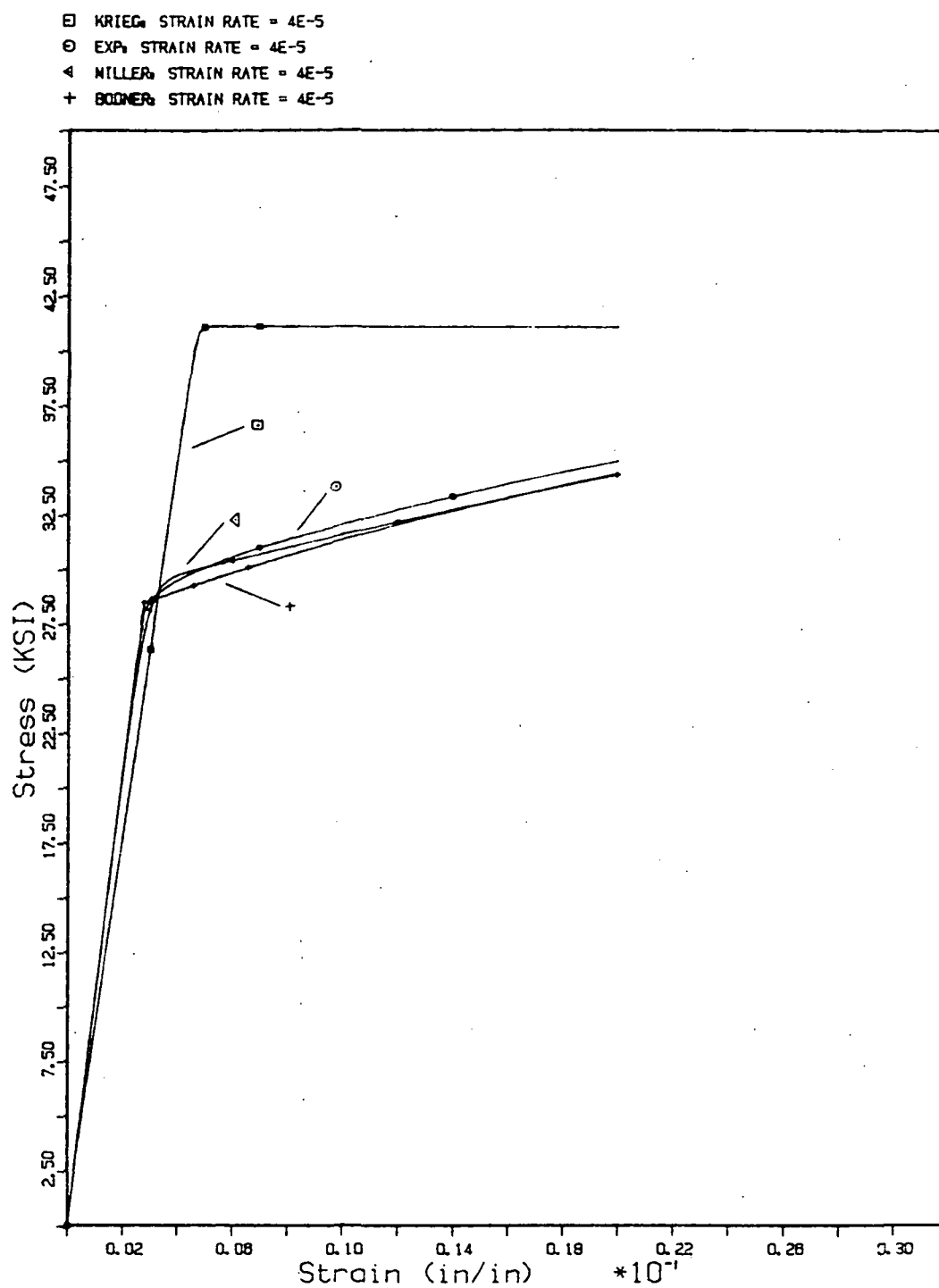


Fig. 27 Constant strain rate tensile test. Comparison of all theories to experiment.

Many theories use creep tests or constant strain rate tensile tests as information for the material parameter determination; consequently, one would expect fairly accurate simulations of these types of load histories. A more rigorous comparison, however is a cyclic load history, as shown in Figure 28 with $\dot{\epsilon} = \pm 1(10)^{-4} \text{ sec}^{-1}$ for cycles 1-10. The experimental data exhibit a pronounced Bauschinger effect and considerable cyclic strain hardening, although it appears that the hysteresis loop saturates fairly quickly.

Krieg, et al.: Cyclic Loading Test

The cyclic response of the theory of Krieg, et al., is shown in Figure 29 for cycle 1. It can be seen that the theory does indeed predict a Bauschinger effect, although it is not as pronounced as the experimental data. The model predicts a harder material than is the actual case, resulting in the very thin and, as expected, "over-square" hysteresis loop. This may be due to the ratio c_3/c_4 (calculated from stress-drop data) being too large.

A comparison of the prediction for cycles 1 and 10 can be seen in Figure 30, where, as expected, the model does not display significant cyclic strain hardening. However, since the material exhibits cyclic strain hardening, the difference between the saturated experimental and

EXP. STRAIN RATE = $\pm 1 \times 10^{-4}$, CYCLES 1-10

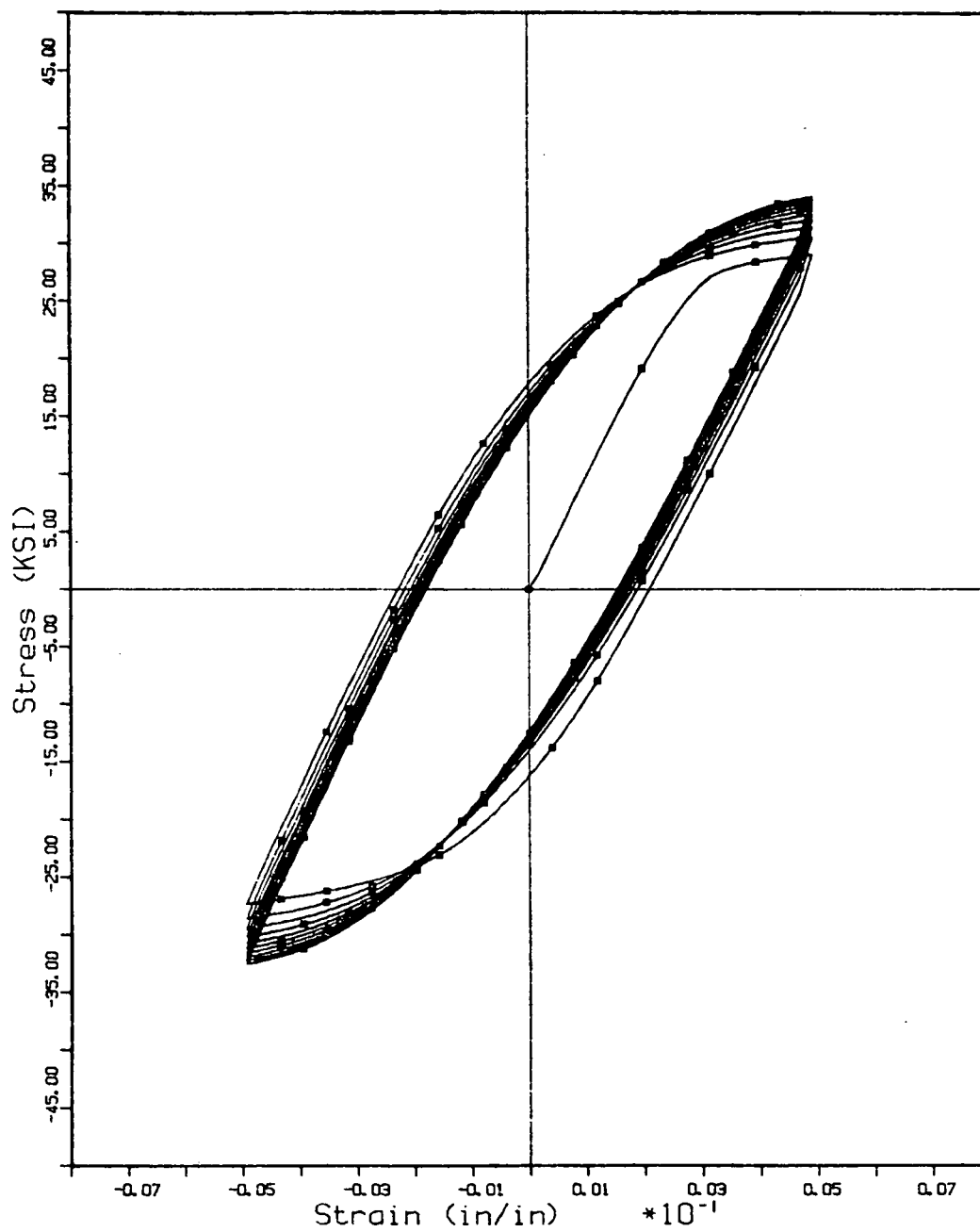


Fig. 28 Experimental cyclic loading test: cycles 1-10

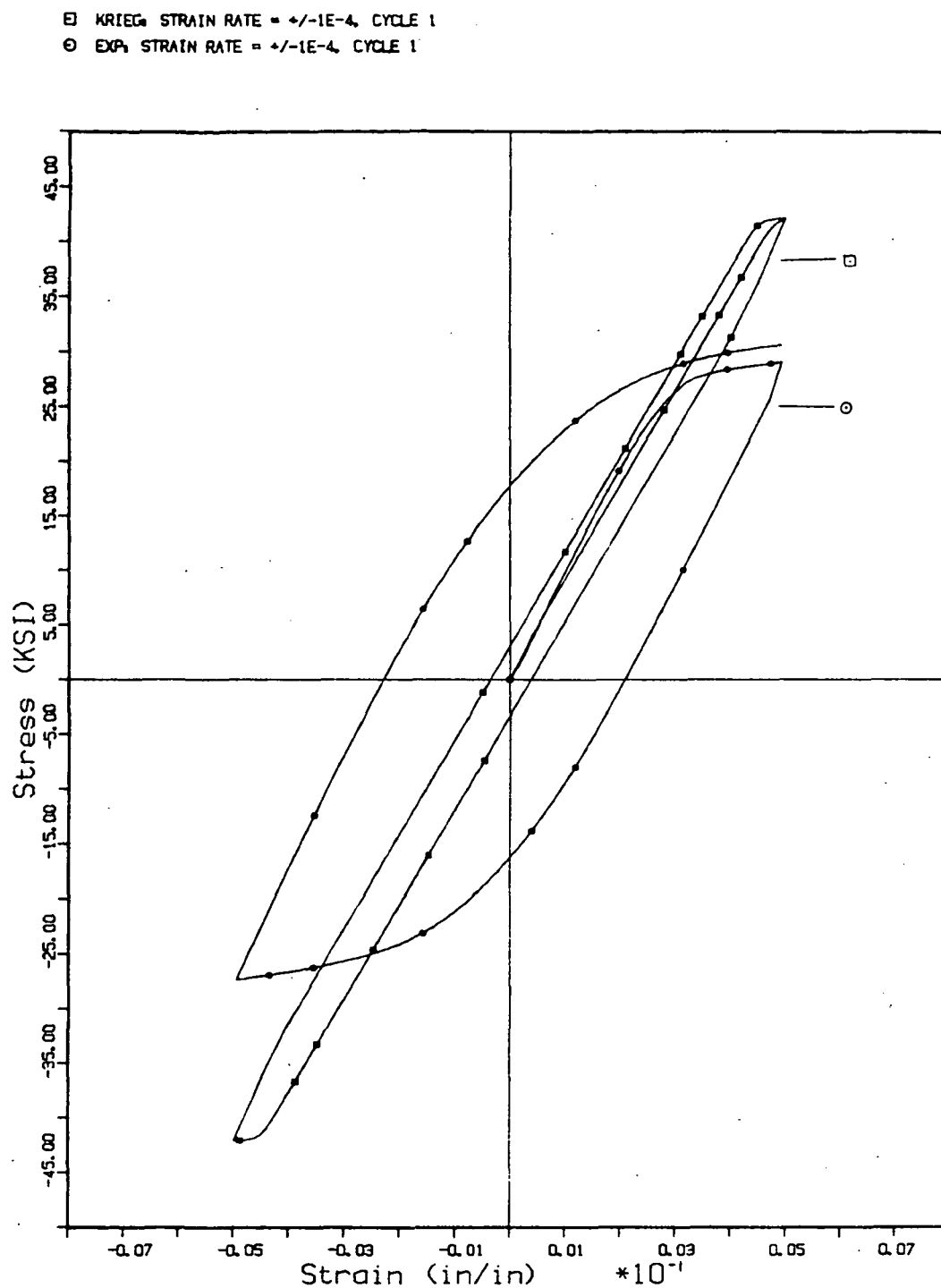


Fig. 29 Cyclic loading test: Cycle 1. Comparison of theory of Krieg, et al., to experiment.

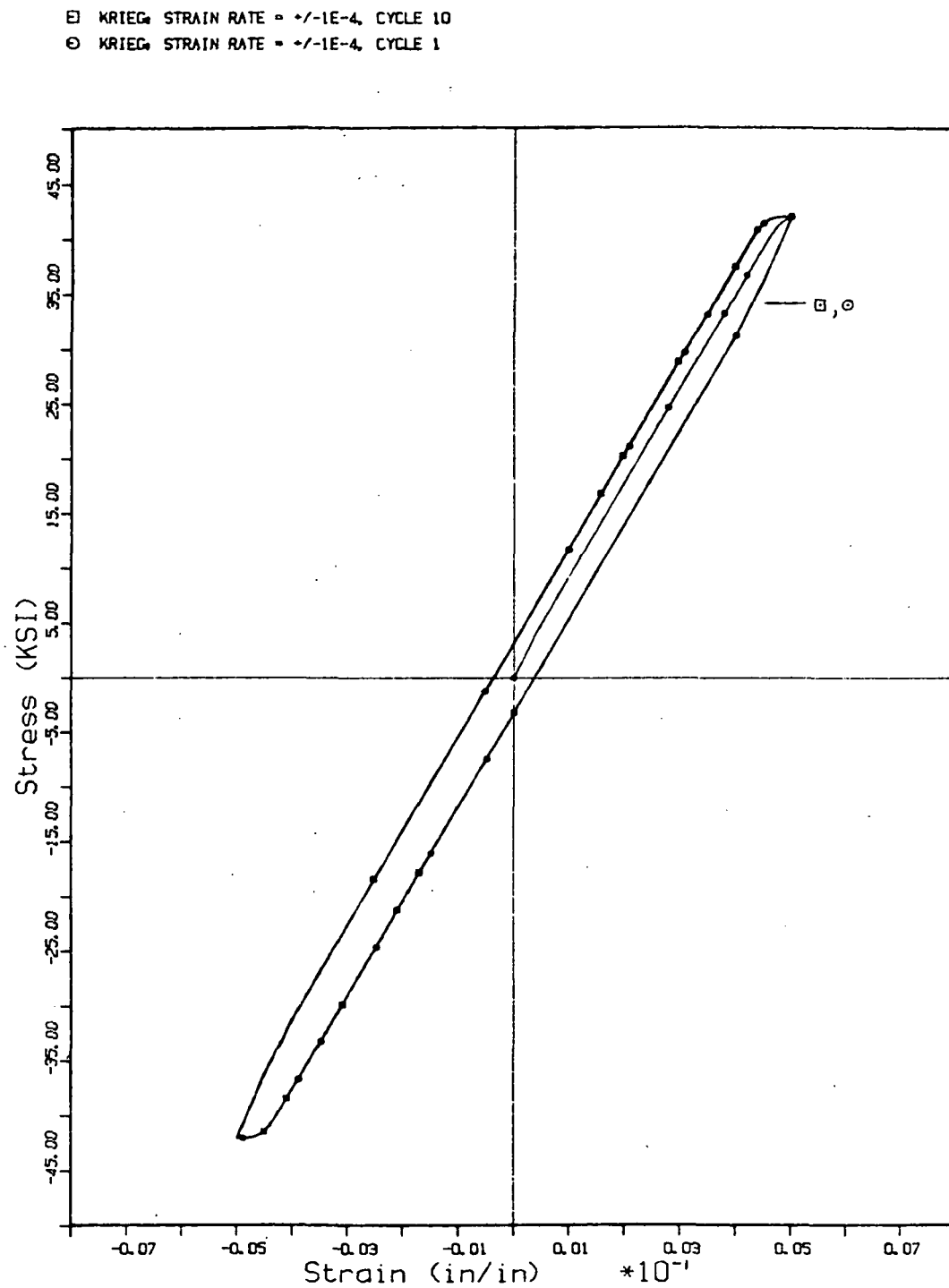


Fig. 30 Cyclic loading test: cycles 1 and 10. Prediction of theory of Krieg, et al.

predicted loops diminishes somewhat, as shown in Figure 31.

Bodner, et al.: Cyclic Loading Test

Figure 32 shows that this theory models cycle 1 fairly well, although the elastic-inelastic behavior transition is too sharp (as noted in earlier tensile data also). The absence of the Bauschinger effect suggests that a directional hardening term is necessary. This can also be seen when examining the γ v. σ graph used earlier in calculating some of the material constants. Although the theory assumes a linear relationship between γ and σ , the experimental data suggest a bilinear relationship. This is examined in greater detail by Bodner, et al., in recent work [109-111]. The upper slope in this bilinear relationship governs directional hardening and the lower slope governs isotropic hardening. It can be seen easily that including such a directional hardening term could provide the Bauschinger effect and also decrease the height of the hysteresis loop.

The aforementioned observations can also be seen in Figures 33 and 34, which compare prediction for cycle 1 to prediction for cycle 10 and prediction to experiment for cycle 10, respectively.

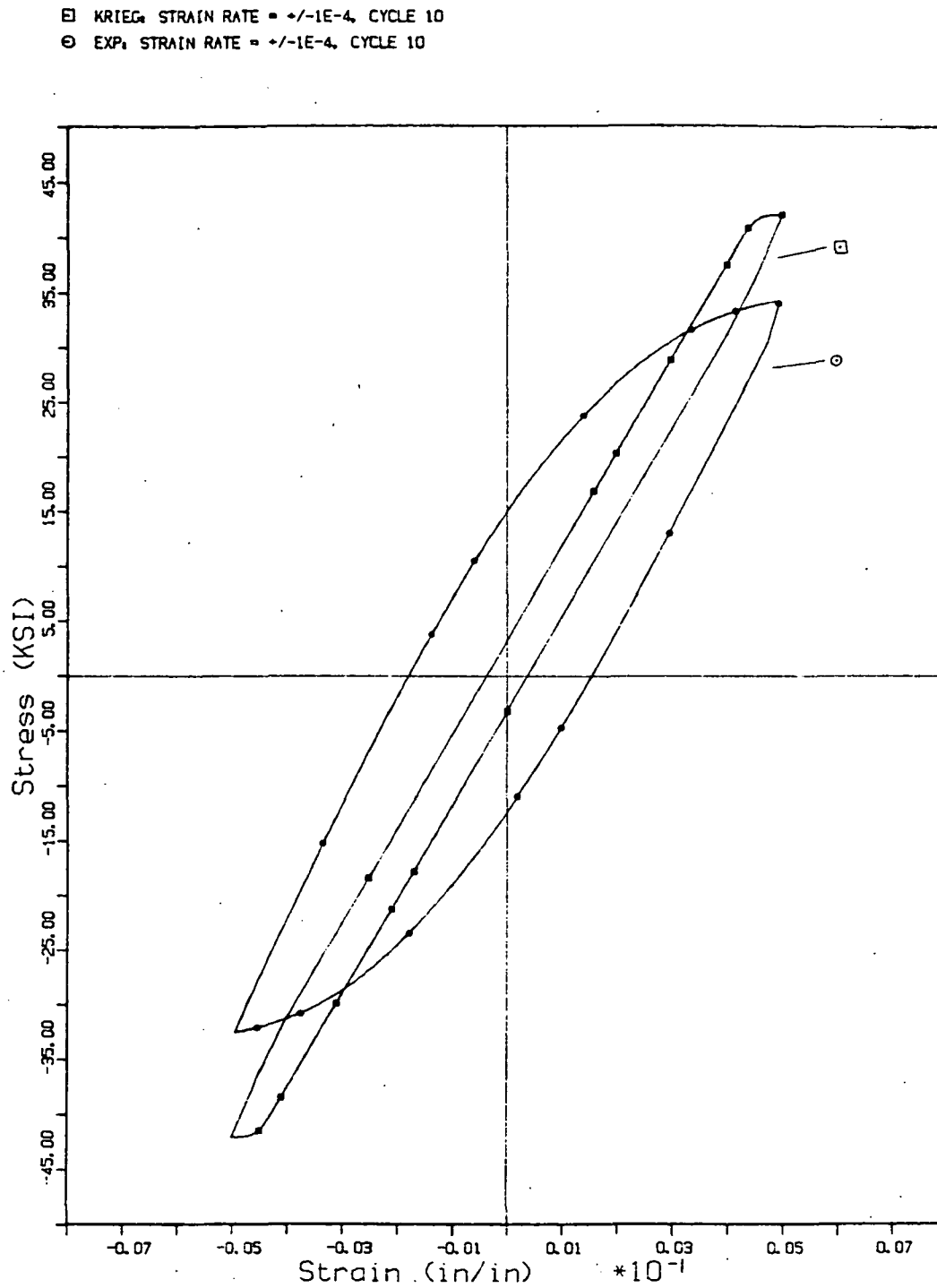


Fig. 31 Cyclic loading test: cycle 10. Comparison of theory of Krieg, et al., to experiment.

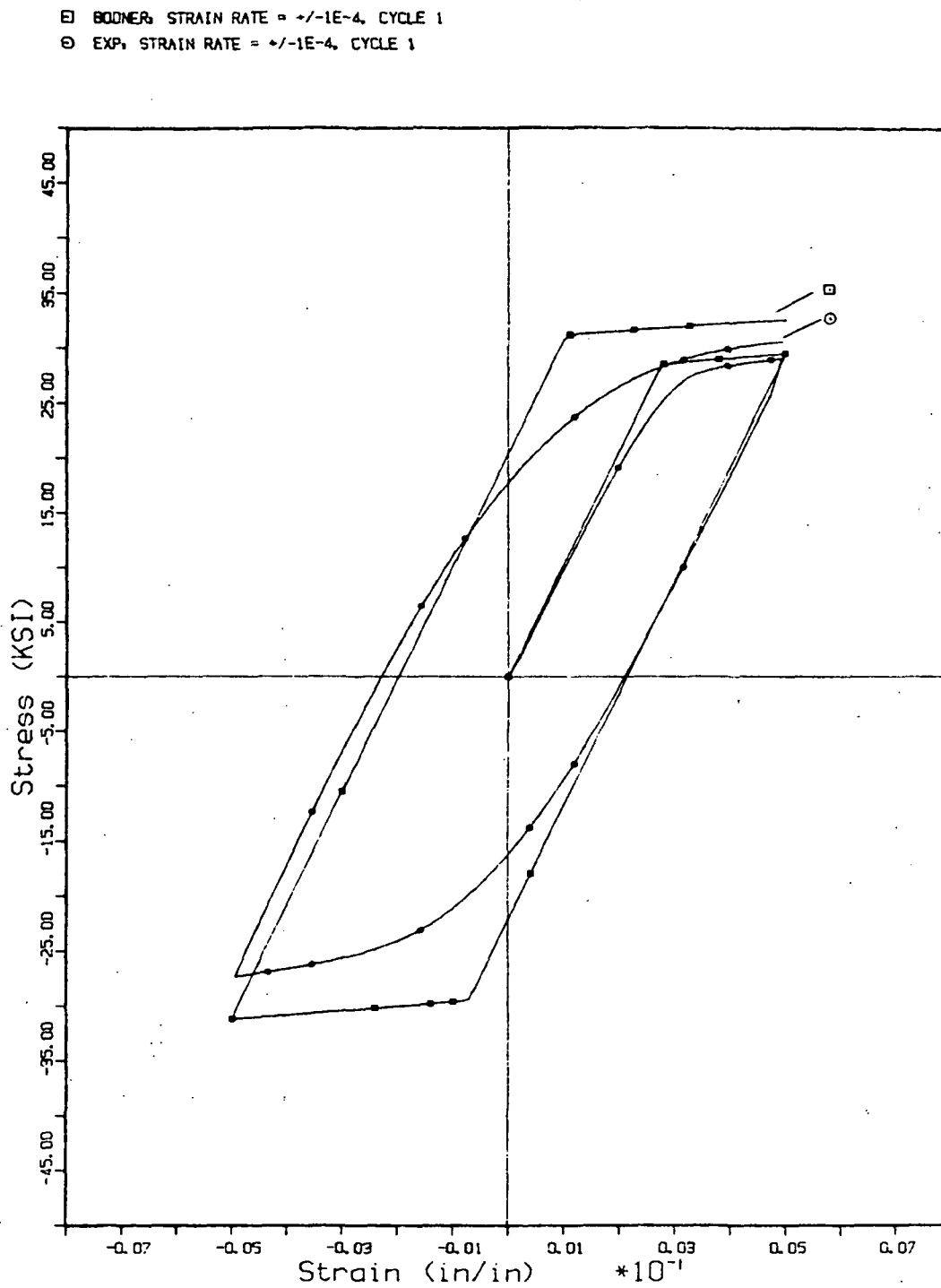


Fig. 32 Cyclic loading test: cycle 1. Comparison of theory of Bodner, et al., to experiment.

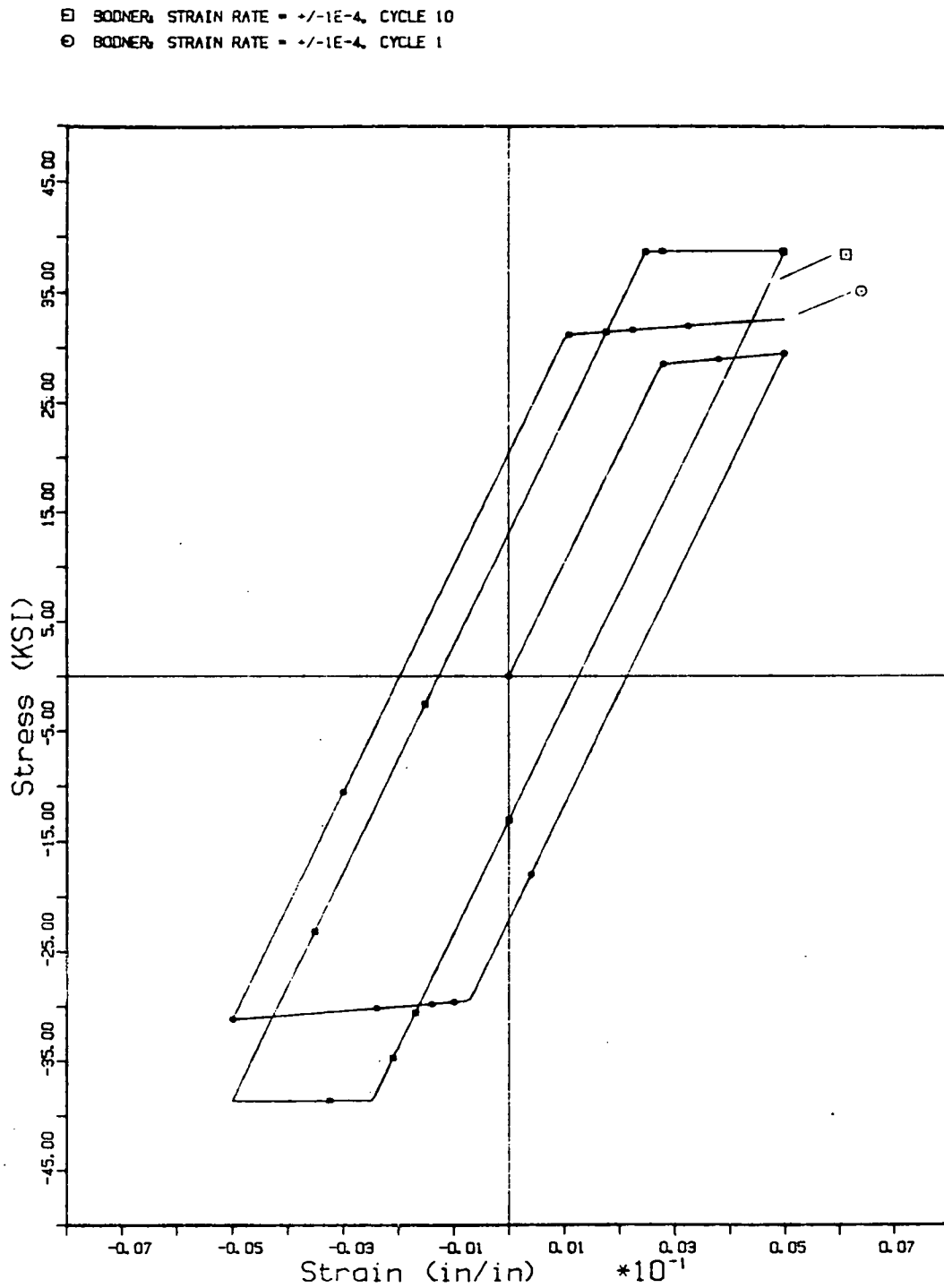


Fig. 33 Cyclic loading test: cycles 1 and 10. Prediction of theory of Bodner, et al.

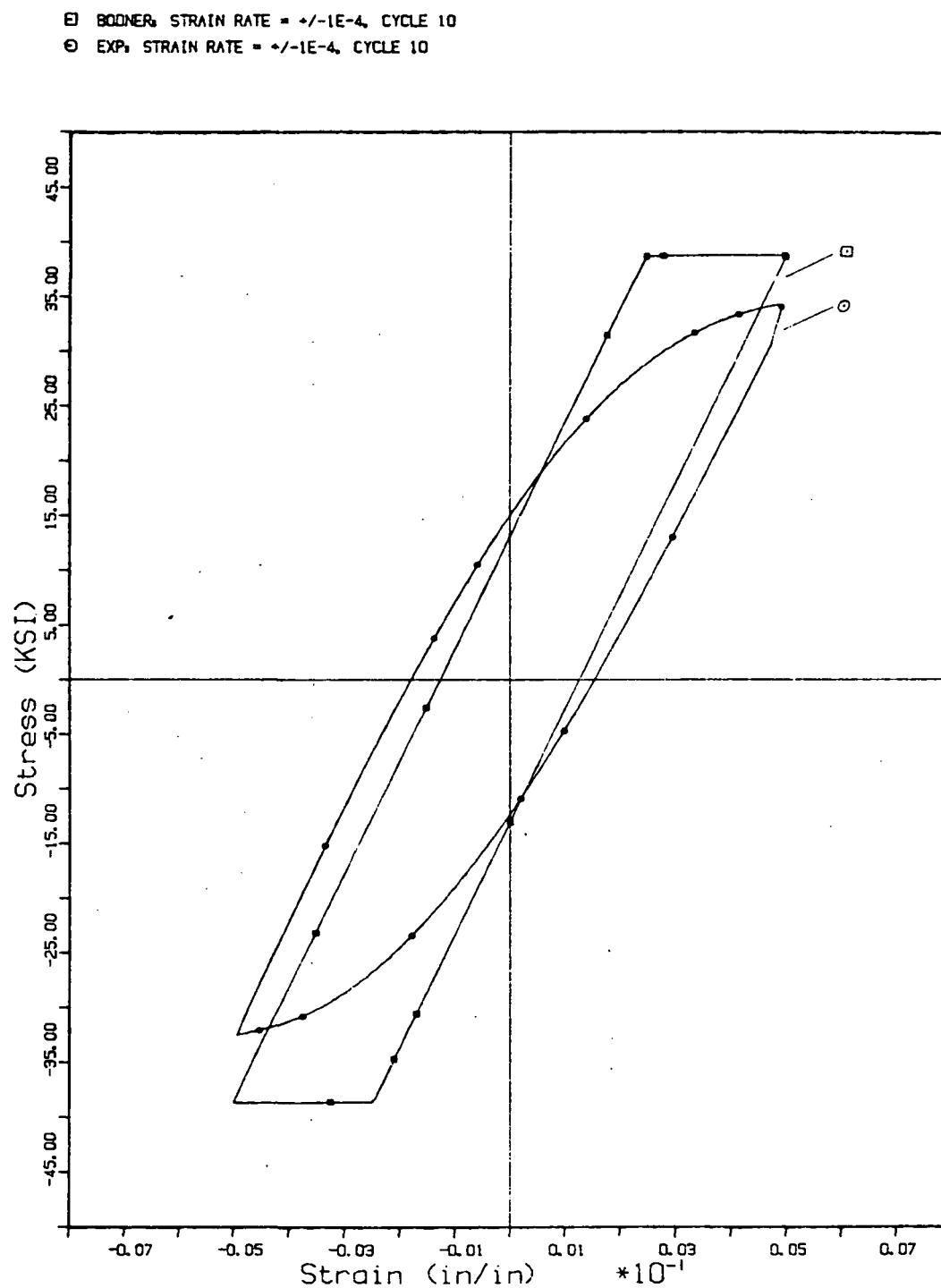


Fig. 34 Cyclic loading test: cycle 10. Comparison of theory of Bodner, et al., to experiment.

Miller, et al.: Cyclic Loading Test

The similarities between this model and that of Bodner, et al., can be seen in Figure 35 in that the theory does not model the Bauschinger effect due to the absence of a directional hardening term. It can also be seen that the assumption of a constant hardening function for the drag stress causes an "over-square" loop, although this is not as pronounced here as with the other two models.

Comparing the predictions of cycle 10 and cycle 1 shows extensive cyclic strain hardening (see Figure 36). This is much more apparent in the theory-to-experiment comparison for cycle 10, as shown in Figure 37, and suggests a need for a revision of the hardening function.

Finally, a comparison of all models for cycles 1 and 10 is shown for completion in Figures 38 and 39, respectively.

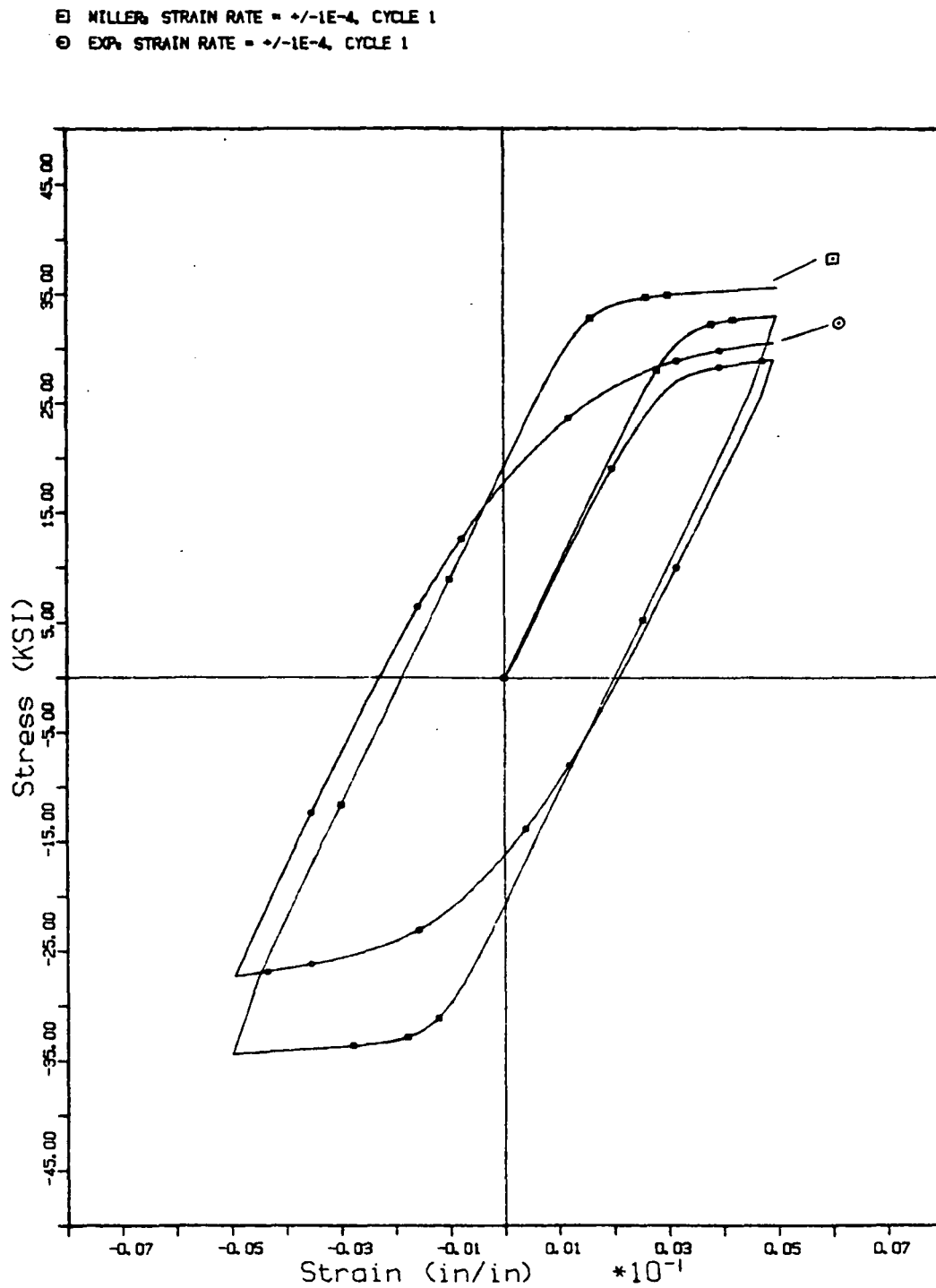


Fig. 35 Cyclic loading test: cycle 1. Comparison of theory of Miller, et al., to experiment.

- MILLER, STRAIN RATE = $\pm 1E-4$, CYCLE 10
 ○ MILLER, STRAIN RATE = $\pm 1E-4$, CYCLE 1

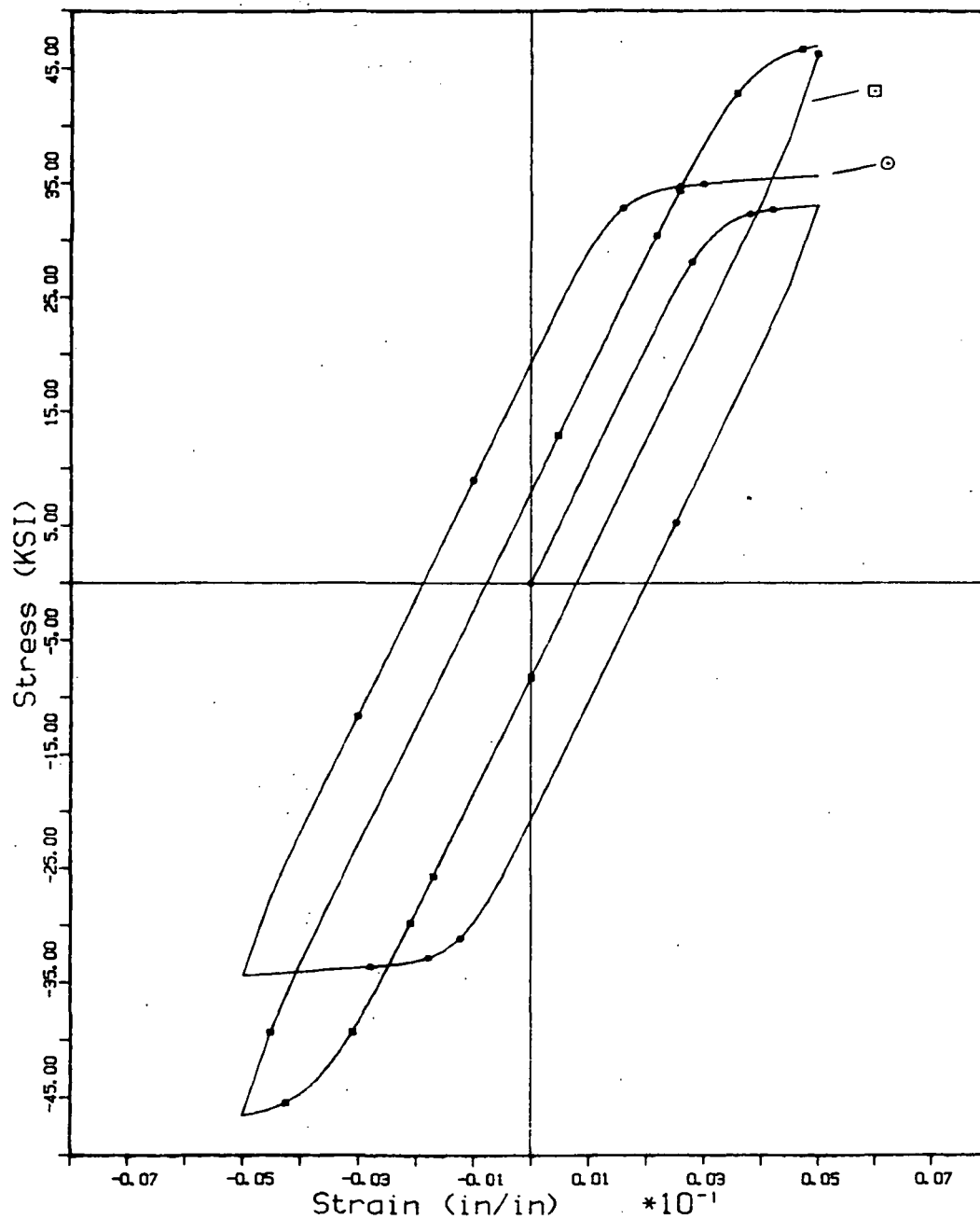


Fig. 36 Cyclic loading test: cycles 1 and 10. Prediction of theory of Miller, et al.

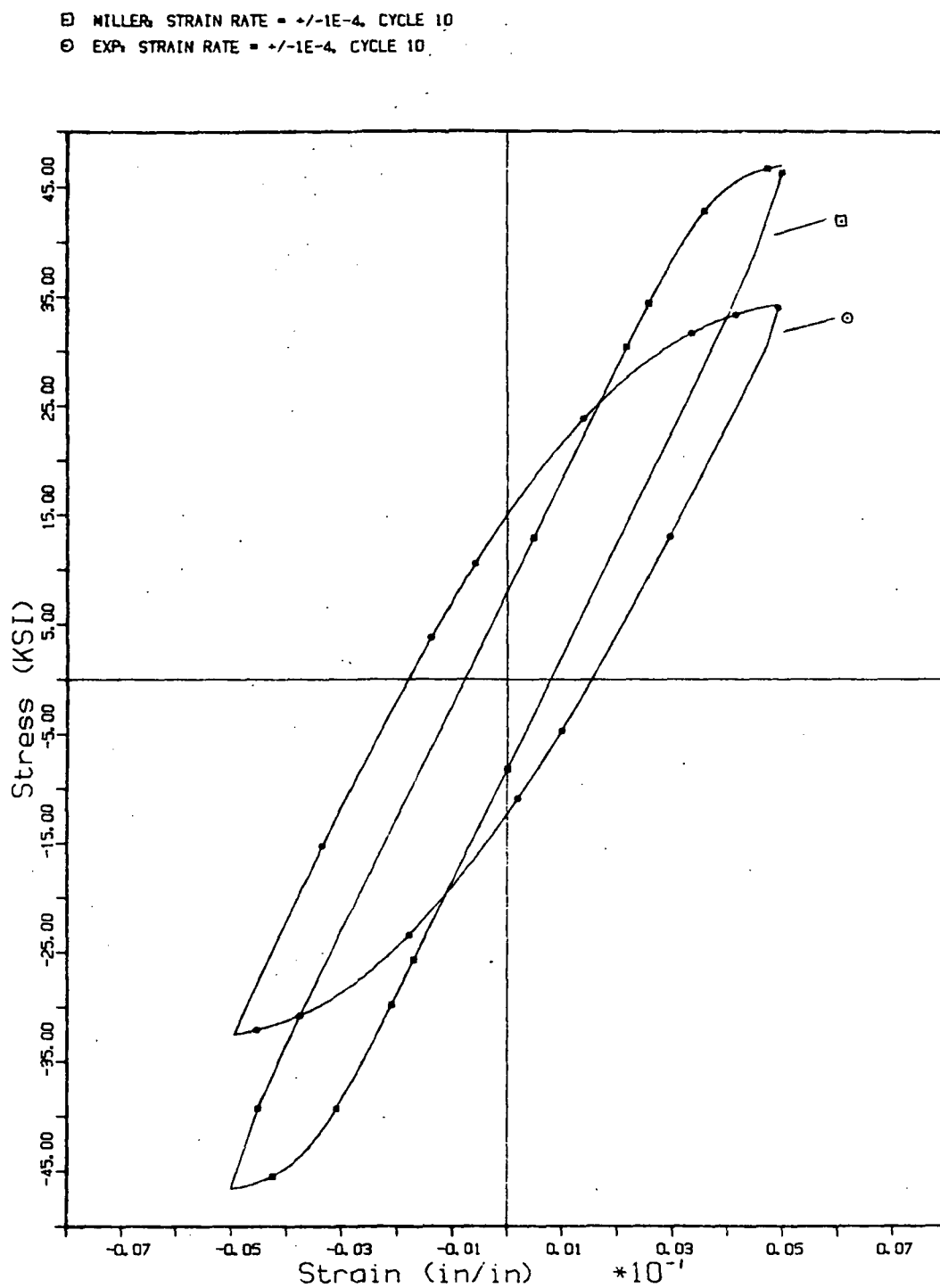


Fig. 37 Cyclic loading test: cycle 10. Comparison of theory of Miller, et al., to experiment.

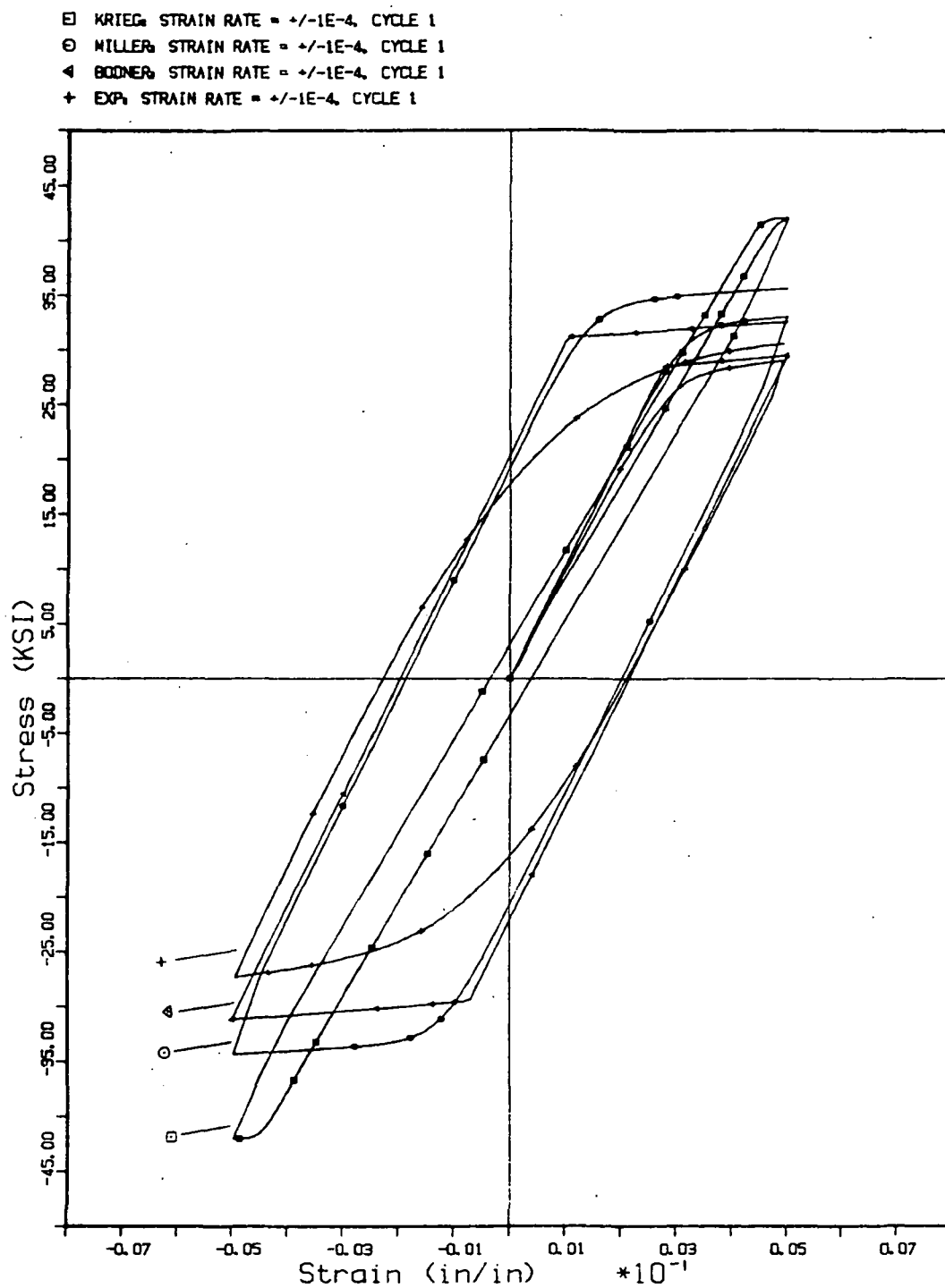


Fig. 38 Cyclic loading test: cycle 1. Comparison of all theories to experiment.

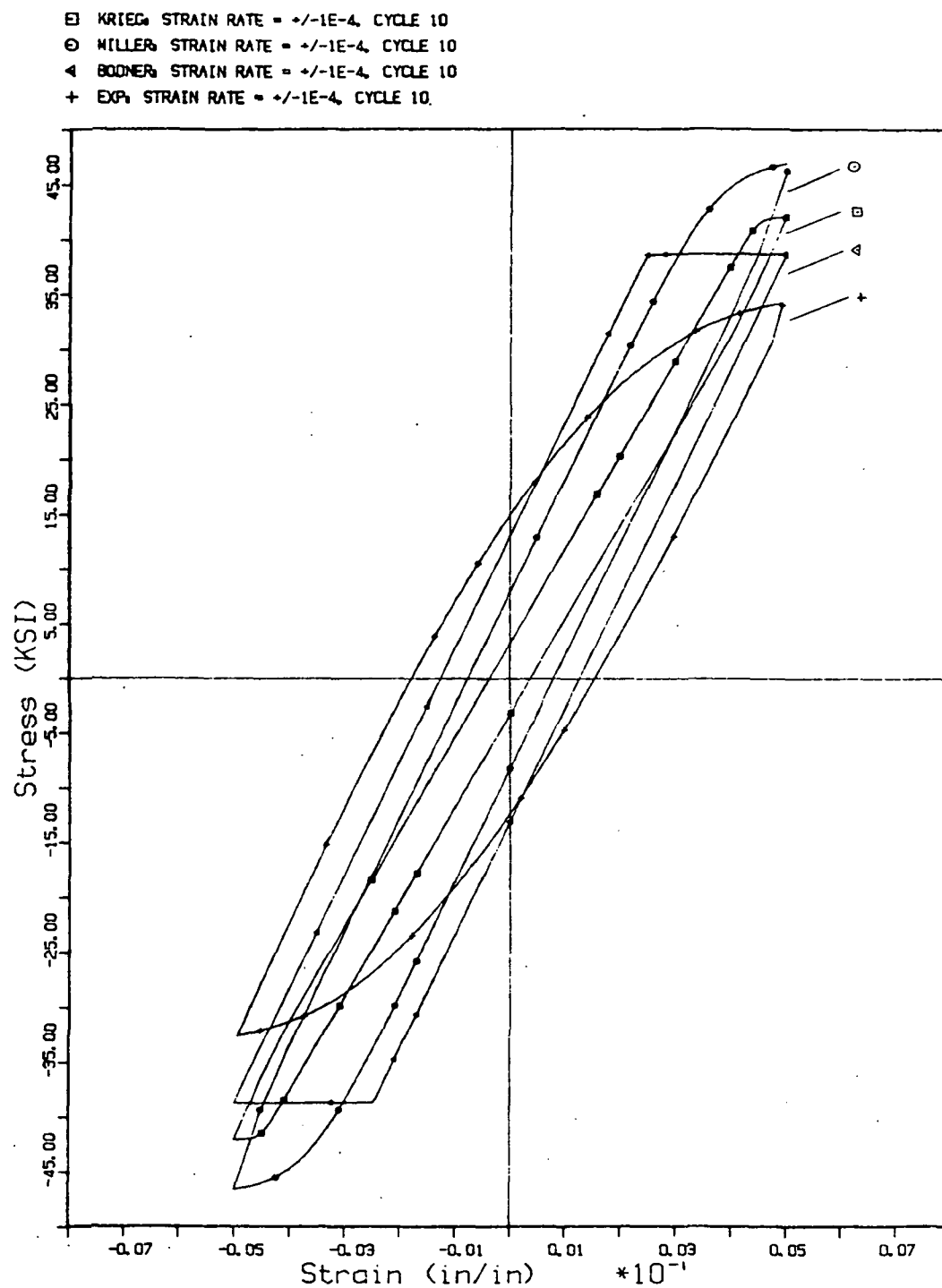


Fig. 39 Cyclic loading test: cycle 10. Comparison of all theories to experiment.

The final set of comparisons involves the prediction of the response to a complex loading history. Many models are designed specifically for creep response or cyclic response with somewhat limited capability for a general, complex response. The loading history is shown in Figure 40; the experimental response is shown in Figure 41.

Krieg, et al.: Complex Loading History

Figure 42 shows that this model over-predicts the stress, indicating that the inelastic strain is growing too slowly. This implies that the back stress is growing too quickly and that the hardening/recovery ratio is too large. Further evidence of this is demonstrated by the considerable amount of relaxation in compression. As before, this discrepancy may be due to the method of material constant determination.

Bodner, et al.: Complex Loading History

Figure 43 shows that this theory predicts the complex loading response very well. The model appears to predict a harder material with less relaxation than the experiment, again suggesting that the hardness Z is too large. A large Z causes a large $\dot{\epsilon}$, leading to an over-prediction of stress. Similarly, during relaxation (when $\dot{\epsilon} = 0$), a large Z causes a small $\dot{\sigma}$, leading to little relaxation.

Fig. 40 Experimental complex loading history

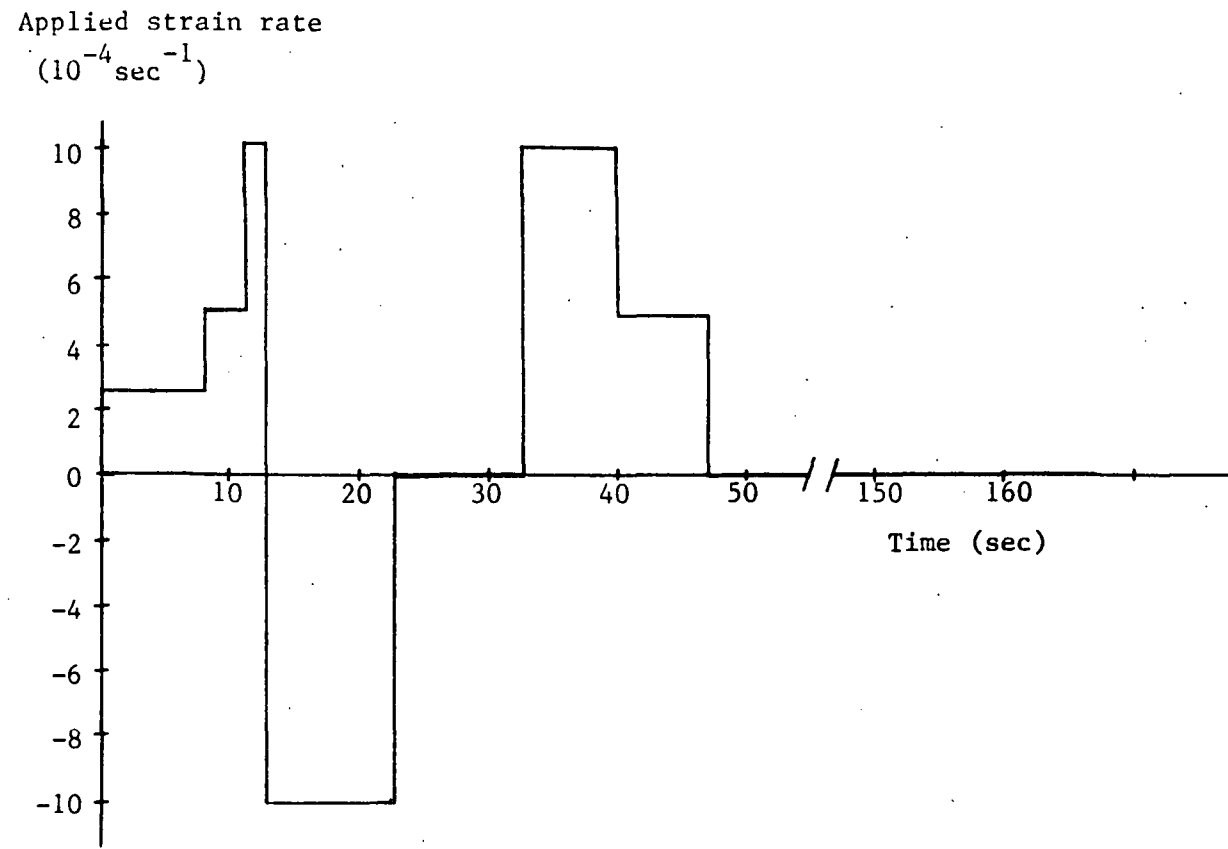
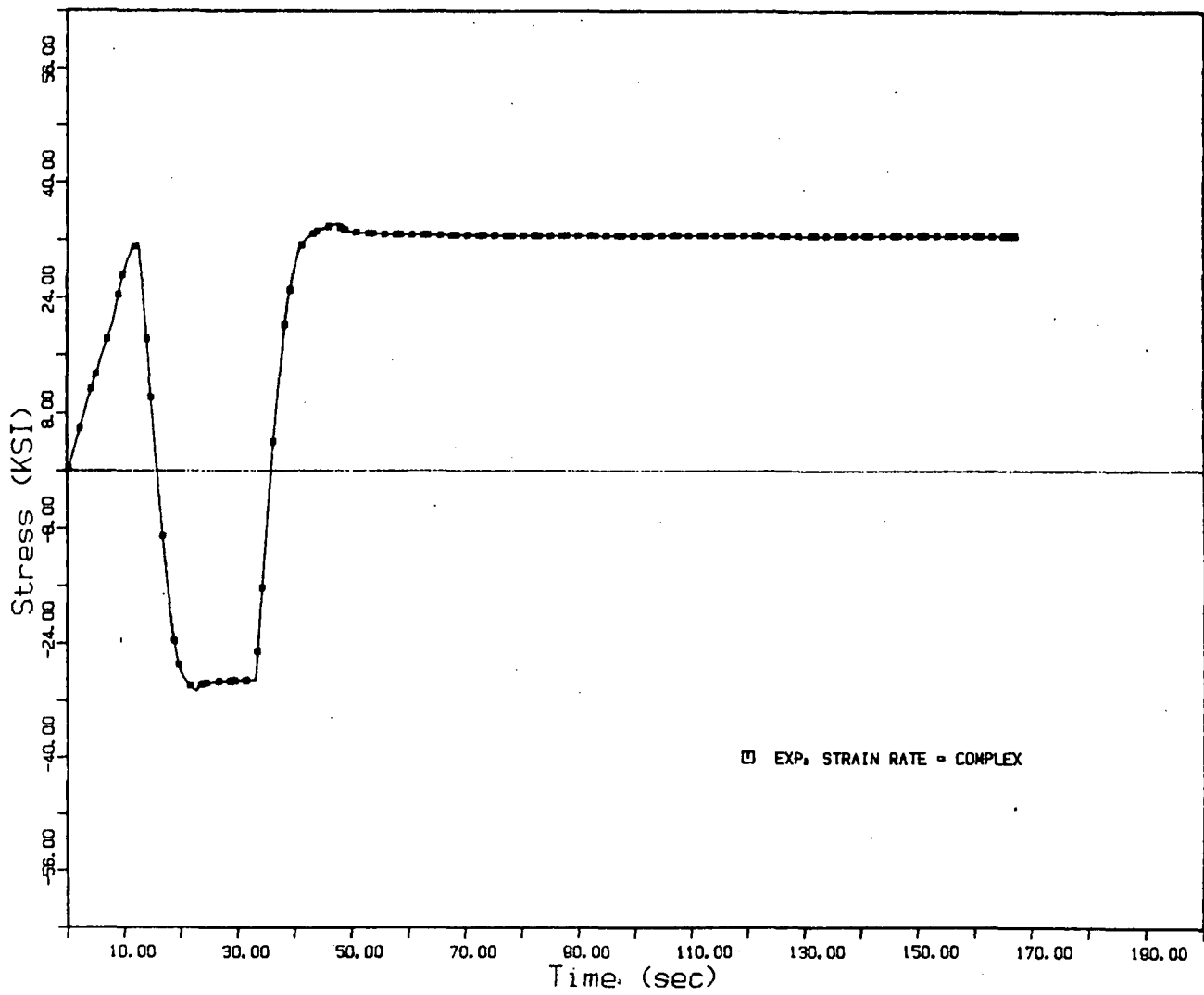


Fig. 41 Experimental complex loading response



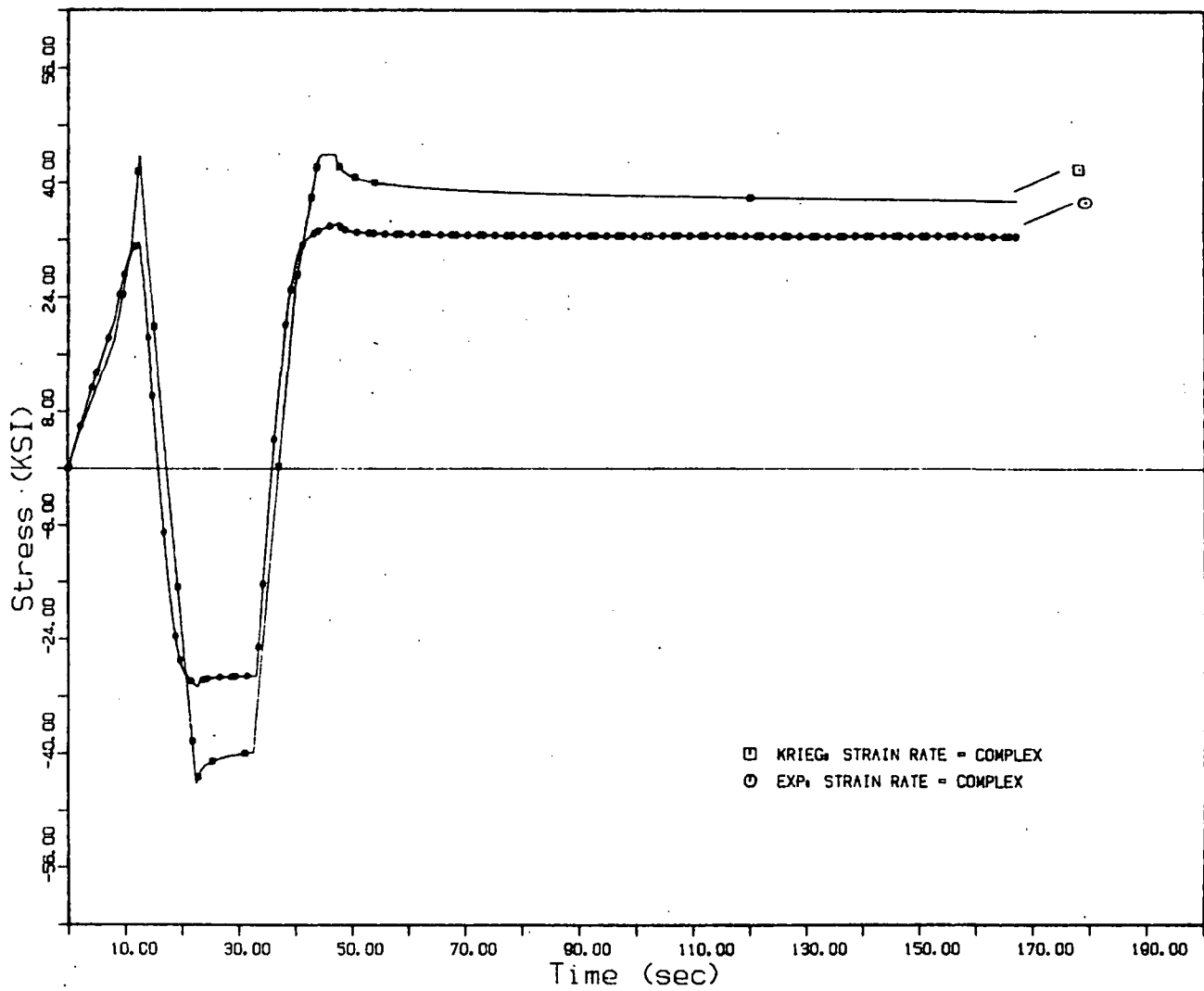
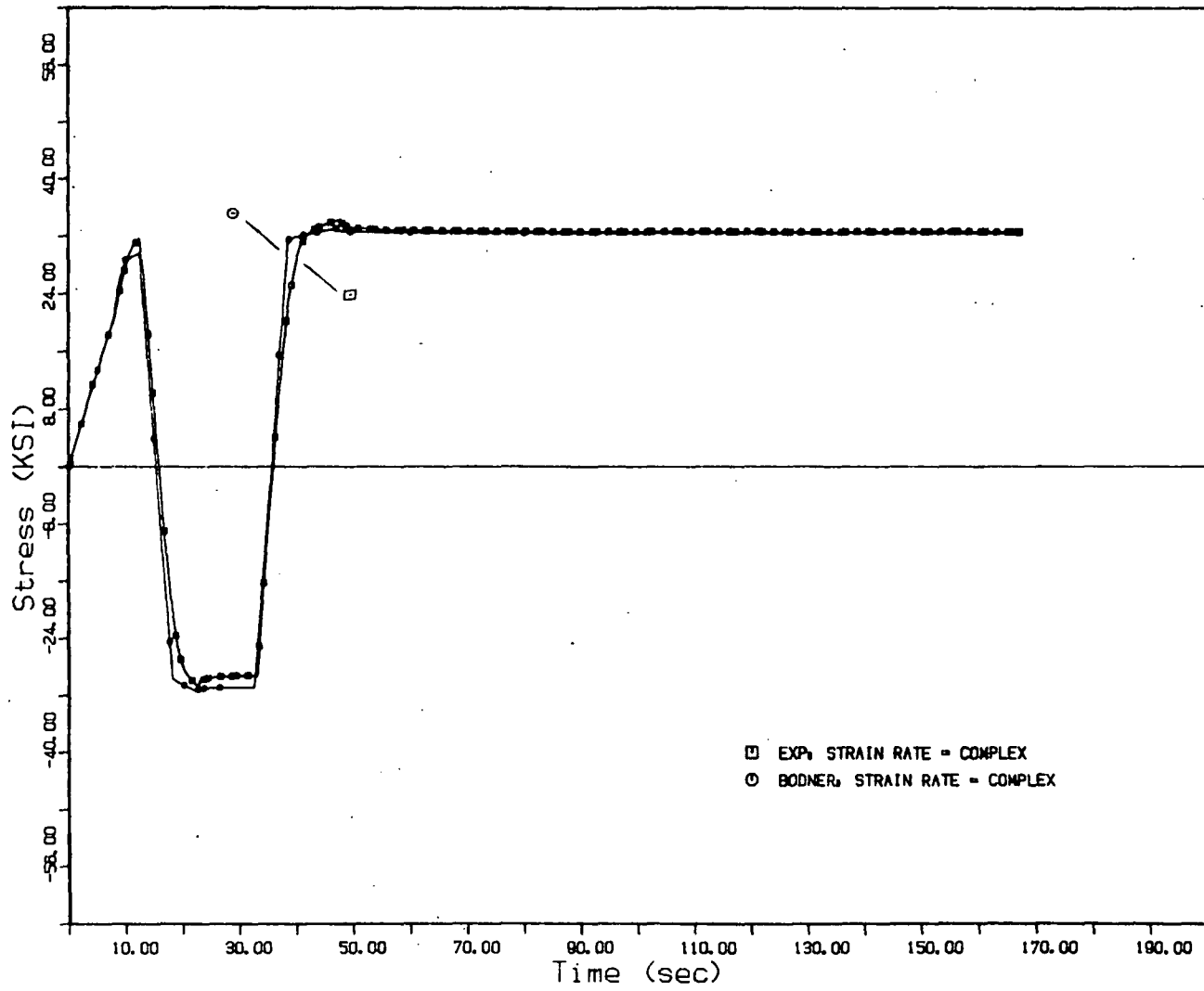


Fig. 42 Complex loading test. Comparison of theory of Krieg, et al., to experiment.

Fig. 43 Complex loading test. Comparison of theory of Bodner, et al., to experiment.



Miller, et al.: Complex Loading History

Figure 44 shows that this model over-predicts the stress during loading and unloading. This may be due to the fact that the hardening constant was set arbitrarily by fitting theory to experiment for a given strain rate, whereas the complex loading test involves strain rates upto two orders of magnitude higher. The large amount of relaxation is then brought on by the large value of stress.

Furthermore, it should be noted that, at approximately 40 seconds, the model experiences a negative stress rate immediately after the applied total strain rate is reduced. Again, this is due to the large value of stress causing the inelastic strain rate momentarily to be larger than the total strain rate. This decreases σ until $\dot{\epsilon}^I$ is less than $\dot{\epsilon}$, at which point the response returns to normal.

A solution to this could be an improved method for determining H , as well as a more complex hardening law for the drag stress.

Finally, a comparison of all theories to experiment for the complex loading history is shown in Figure 45 for completion.

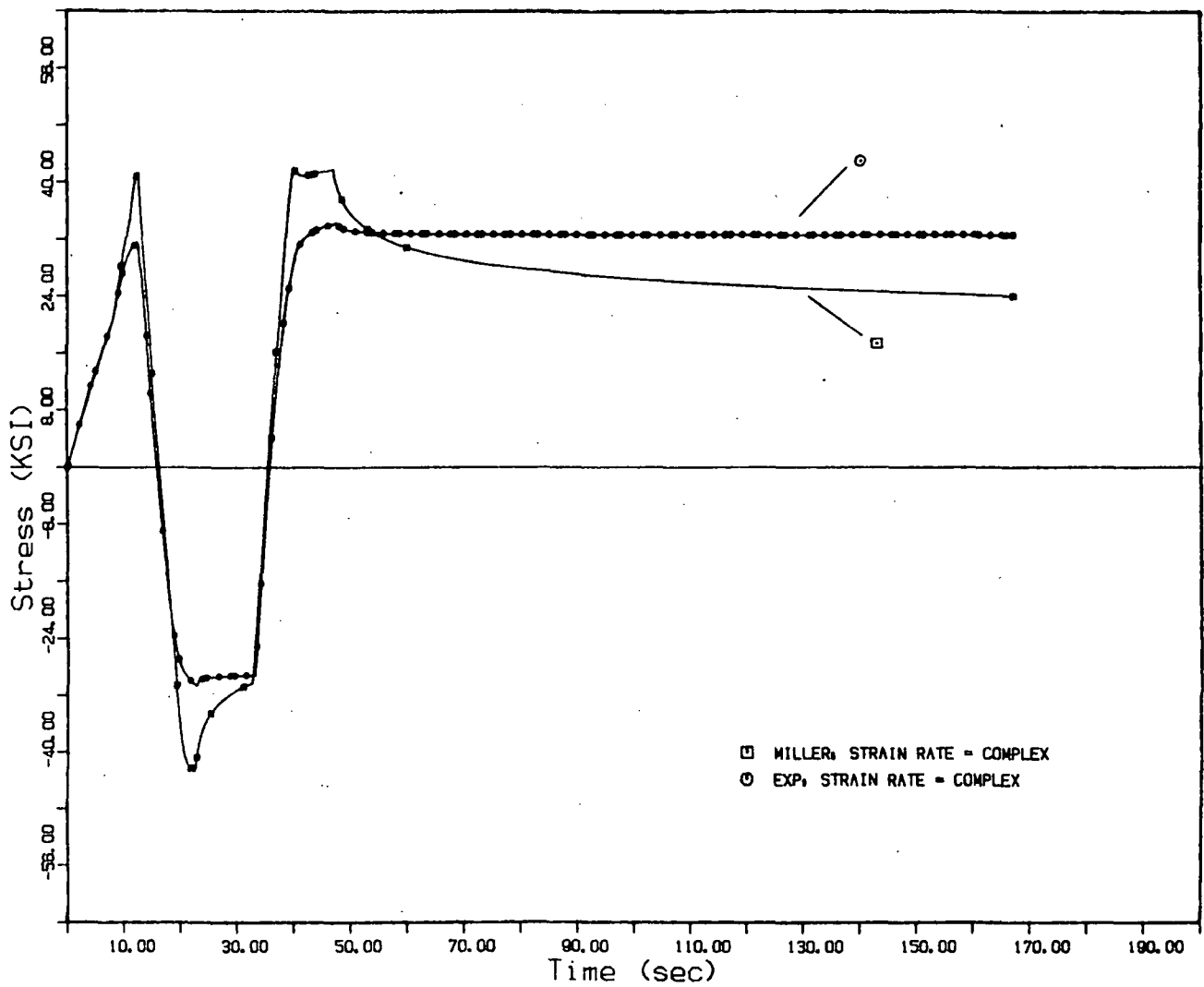


Fig. 44 Complex loading test. Comparison of theory of Miller, et al., to experiment.

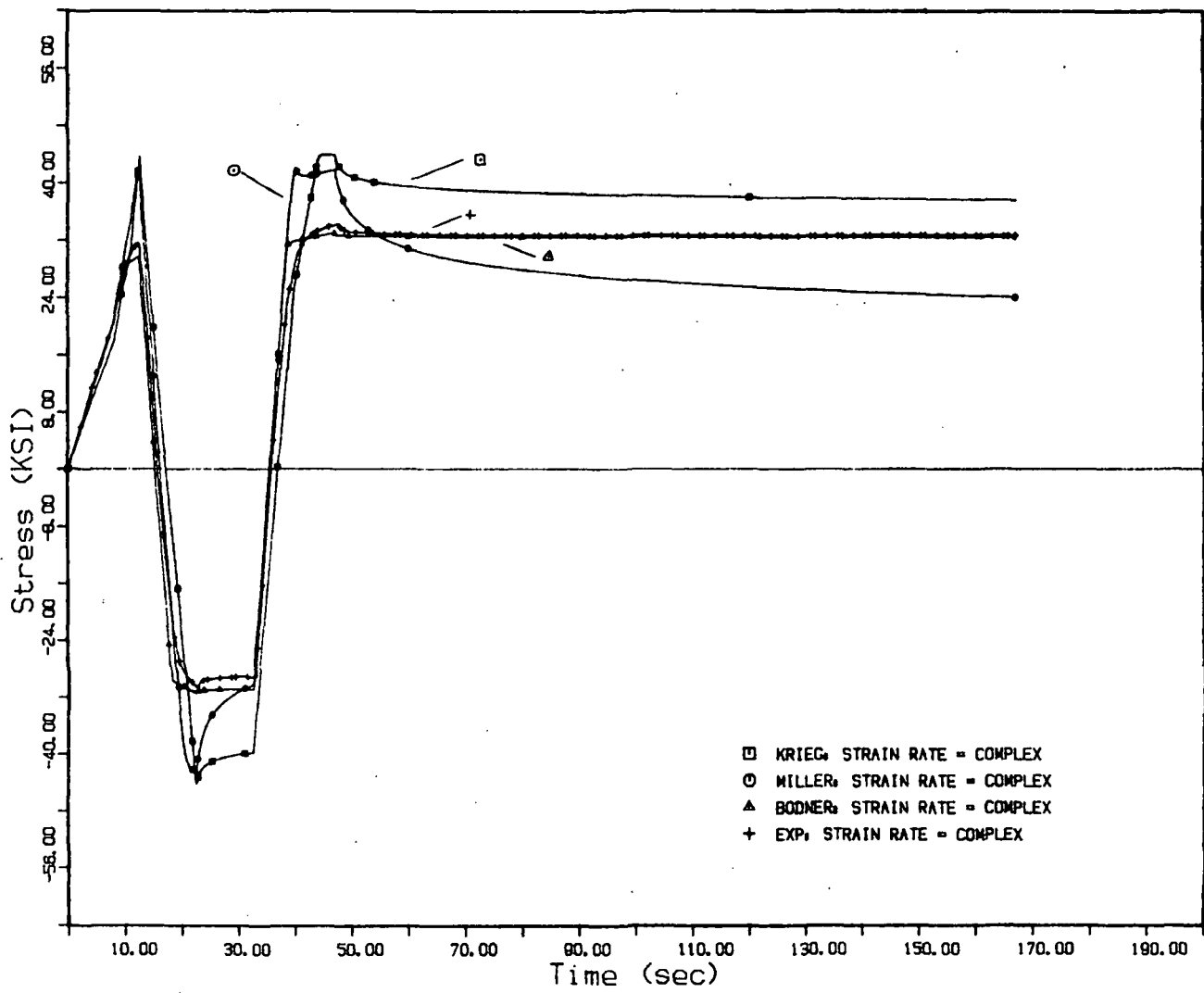


Fig. 45 Complex loading test. Comparison of all theories to experiment.